DEVELOPMENT OF METHODOLOGY TO ESTIMATE FRACTIONAL FLOW RESERVE USING MAGNETIC RESONANCE IMAGING AND COMPUTATIONAL FLUID DYNAMICS

A Dissertation
Presented to
The Academic Faculty

By

Jackson Brooks Hair

In Partial Fulfillment
Of the Requirements for the Degree
Doctor of Philosophy in Biomedical Engineering

Georgia Institute of Technology
Emory University

May 2020

DEVELOPMENT OF METHODOLOGY TO ESTIMATE FRACTIONAL FLOW RESERVE USING MAGNETIC RESONANCE IMAGING AND COMPUTATIONAL FLUID DYNAMICS

Approved by:

John N. Oshinski, Advisor
Department of Radiology and Imaging Sciences
Emory University School of Medicine

Wei Sun
Department of Biomedical Engineering
Georgia Institute of Technology and Emory University

Shella Keilholz
Department of Biomedical Engineering
Georgia Institute of Technology and Emory University

Lucas Timmins
Department of Biomedical Engineering
University of Utah

Habib Samady
Division of Cardiology
Emory University School of Medicine

Date Approved: March 20, 2020

ACKNOWLEDGEMENTS

In the fall of 2015, I started working towards my PhD in Biomedical Engineering less than four months after receiving my undergraduate degree from the same department. In many ways, my graduate education has felt like an extension of my undergraduate—nine years with many of the same familiar faces. It is therefore hard for me to fully separate these two periods of my life and to acknowledge who contributed to one and not the other, so I will make no such attempt.

My love of engineering has been constant in my life, but it was not until I enrolled at Georgia Tech in 2011 that I was truly able to experience it. Though I initially chose to pursue biomedical engineering on a whim, I very quickly found that I had made the correct choice. Several instructors during this time had particular impact on me. I credit Essy Behravesh for my appreciation of the scientific method and statistical analysis, Ross Ethier for introducing me to Navier–Stokes, and Wei Sun for my first exposure to academic research and cardiovascular modeling. These three individuals drove me to pursue graduate education and had the greatest influence in my choice of research topic.

Though I chose to remain with the same department, I was fortunate in that it was affiliated with two universities. This gave me the freedom to find an advisor at Emory, and I could not have been more fortunate in having chosen John Oshinski. John has the greatest respect for his students and does all that he can to foster their independence. He allowed me to make my own decisions about my research but provided constant guidance so that those decisions would be well-informed. He somehow manages to perfectly balance always

being available without being overbearing, and he gave me a true understanding of reconciling my professional and personal lives for which I will forever be grateful.

Though my project has been my own, I have been lucky to work with many collaborators and mentors during this time. Adrian and Lizz were very helpful to me when I was first starting out in juggling coursework at Georgia Tech and lab work at Emory. Luke and David introduced me to many of the software programs I still use today—including Fluent and Segment—and were always willing to help me work out whatever problems I encountered. Shella and Xiaoping taught me so much about imaging and signal processing, two areas in which I had no background prior to starting graduate school. Habib, despite his unbelievably busy schedule, would always eventually find time to meet with me when I requested it to provide direct clinical feedback on my research. For my many other technical challenges, I was always able to find someone willing to help me at either Emory or Georgia Tech, including Mohammed, Zahra, Puneet, Marty, and Steven. All of these individuals consistently took time out of their schedules for me, and they never asked for anything in return.

At some point, my technical requirements necessitated that I seek additional help from overseas. The Biomedical Engineering department selected me as a recipient for a travel award named in honor of Bob Nerem so that I could go to Switzerland. I was welcomed there by Matthias Stuber's group. Though my time there was short, I learned so much from Jerome and Davide, who continued to provide support once I had returned home. Lorenzo and Stephanie also proved invaluable with their assistance, and I owe them greatly.

My research is translational in nature, and much of my data came directly from patients. The Emory Healthcare clinical staff devoted hours of their lives to helping me with this. Anurag would allow me to run my more experimental sequences in place of his routine protocols, even though I could never assure him of their success. He was consistently willing to help, saying that clinicians owe so much to researchers and that it was his responsibility to help me whenever he could. This perspective is often difficult to find, even in a university-affiliated hospital, and it was always refreshing to me. I worked with many clinical fellows during this time, including Peter, Zaid, Varuna, Tony, and Stephanie, and they frequently helped me set up my protocols or answer my many questions about anatomy and pathophysiology. Lastly, Deborah helped me immensely over these years in acquiring the data I desperately needed for my research. She would work me into her already extremely overbooked schedule whenever she could, and I cannot thank her enough.

In 2018, I was able to intern with the Exponent biomechanics practice here in Atlanta. Ian helped me to secure this internship, and he and Stacy provided me with a first-hand look at life after academia for which I am very grateful. This experience gave me a better perspective on what I want out of my professional career, and I will always value this.

Lastly, I want to thank my family. I thank my parents for pushing me to excel both in and out of school. I thank my sister for providing a high standard for me to reach for. Most of all, I thank my wife, Katie, for her unconditional support, for listening to me talk about my research, and for agreeing to volunteer in so many MRI scans for me.

TABLE OF CONTENTS

LIST OF FIGURES

NOMENCLATURE

2D PCMR	Time-resolved one-dimensional phase-contrast MRI
4D-GRASP	4-dimensional golden-angle radial sparse parallel
4D PCMR	Time-resolved three-dimensional phase-contrast MRI
5D-GRASP	5-dimensional golden-angle radial sparse parallel
AUC	Area under the receiver-operator curve
BMR	Basal microvascular resistance
bSSFP	Balanced steady-state free precession
CAD	Coronary artery disease
CFD	Computational fluid dynamics
CFR	Coronary flow reserve
CHD	Congenital heart disease
COURAGE	Clinical Outcomes Utilizing Revascularization and Aggressive Drug Evaluation
CT	Computed tomography
CTA	Computed tomography angiography
DISCOVER-FLOW	Diagnosis of Ischemia-Causing Coronary Stenoses Obtained Via Noninvasive Fractional Flow Reserve

ECG	Electrocardiogram
EDV	End-diastolic volume
ESV	End-systolic volume
EF	Ejection fraction
FAME	Fractional Flow Reserve versus Angiography for Multivessel Evaluation
FDA	Food and Drug Administration
FFR	Fractional flow reserve
FFR_{CT}	Computed tomography–derived fractional flow reserve
FOV	Field-of-view
FRF	Free-Running Framework
GRASP	Golden-angle radial sparse parallel
GRE	Gradient echo
HMR	Hyperemic microvascular resistance
HSR	Hyperemic stenotic resistance
ICA	Independent component analysis
IRB	Institutional Review Board
LAD	Left anterior descending

LCX	Left circumflex
LM	Left main
LV	Left ventricle
MPR	Multiplanar reformation
MR	Magnetic resonance
MRA	Magnetic resonance angiography
MRI	Magnetic resonance imaging
PCI	Percutaneous coronary intervention
PCMR	Phase-contrast magnetic resonance
PET	Positron emission tomography
PSD	Power spectral density
RCA	Right coronary artery
RF	Radiofrequency
ROI	Region-of-interest
SENSE	Sensitivity-encoding
SI	Superior-inferior
SNR	Signal-to-noise ratio

SPECT	Single-proton emission computed tomography
SSFP	Steady-state free precession
SSIM	Structural similarity
VENC	Velocity encoding
vFFR	Virtual fractional flow reserve
XD-GRASP	Extradimensional golden-angle radial sparse parallel

SUMMARY

Fractional flow reserve is the current gold standard for evaluating severity of coronary artery disease, but it is underutilized clinically due to its invasiveness. Recent efforts have worked toward developing non-invasive alternatives, wherein medical imaging data are used to construct patient-specific computational fluid dynamics models to simulate blood flow through the coronary arteries and calculate virtual fractional flow reserve. Magnetic resonance imaging is particularly well-suited for this application due to its ability to directly quantify both angiographic geometry and flow velocity. Therefore, the purpose of this thesis was the investigation and development of magnetic resonance techniques toward defining the patient-specific boundary conditions needed in computationally estimating fractional flow reserve.

In **Aim 1**, we performed a series of computational simulations to determine what patient-specific flow information is needed to calculate virtual fractional flow reserve. Then, we tested phase-contrast magnetic resonance in a cohort of healthy volunteers to validate its ability to quantify coronary arterial flow. In **Aim 2**, several novel implementations of self-gated magnetic resonance angiography were investigated for their ability to characterize coronary arterial geometry. Tests were carried out in several cohorts of adult patients with congenital heart disease and a cohort of pigs to study the use of self-navigation and both four and five–dimensional golden-angle radial sparse parallel magnetic resonance. Optimizations of both the acquisition and reconstruction frameworks were explored. Altogether, these studies advanced the use of magnetic resonance angiography in interventional cardiology.

CHAPTER 1. CLINICAL BACKGROUND

1.1 Coronary Artery Disease

Coronary artery disease (**CAD**) is responsible for half of all deaths attributed to cardiovascular disease, making it a leading cause of death globally [1, 2]. In the United States, approximately 6.7% of adults age 20 and older have CAD [3]. The underlying cause of CAD is atherosclerotic lesions creating flow-limiting stenoses in the coronary arteries, which can result in downstream myocardial ischemia and potentially myocardial infarction. A primary catheter-based revascularization treatment for CAD is percutaneous coronary intervention (**PCI**), which includes angioplasty and deployment of a vascular stent (Figure 1). However, not all patients with CAD are at risk for myocardial infarction,

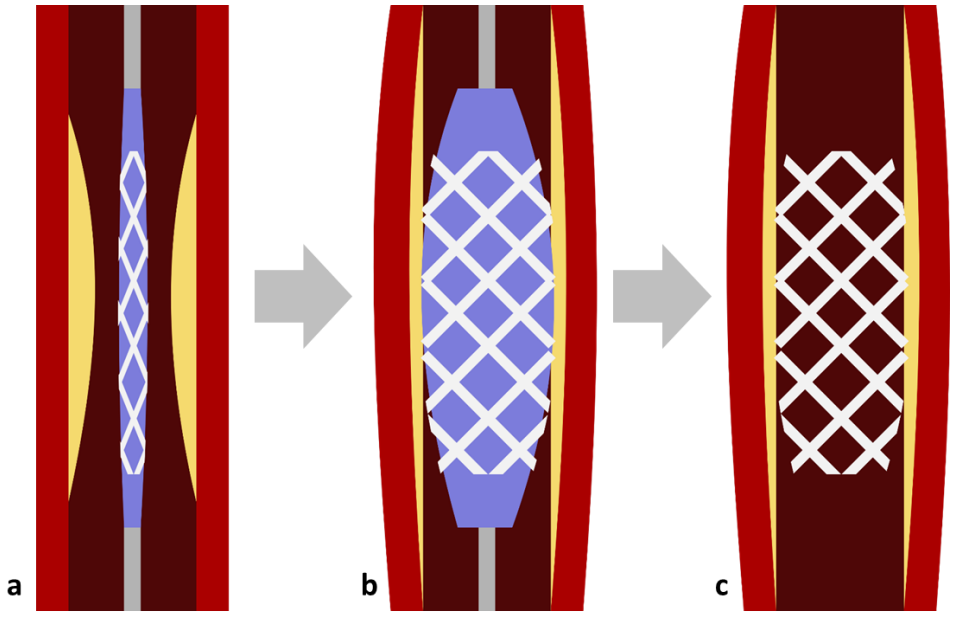

Figure 1: Percutaneous coronary intervention. (a) A catheter is used to position the ballon and stent at the site of narrowing. (b) The balloon in inflated, and the stent is deployed. (c) The catheter and balloon are removed, leaving the stent which keeps the pathway open.

and it is therefore important to be able to correctly identify which patients would benefit from intervention.

Historically, CAD has been assessed through percent anatomic narrowing of the vessel lumen. Gould et al. first demonstrated the relationship between luminal narrowing and ischemia induction in 1974, but more recent studies have shown that anatomic severity of a coronary stenosis is not strongly predictive of its physiologic severity [4]. In 2007, the Clinical Outcomes Utilizing Revascularization and Aggressive Drug Evaluation (**COURAGE**) trial investigated patient outcomes following angiography-guided revascularization. It reported that of patients with ≥70% diameter stenoses, only 32% exhibited severe ischemia and as many as 40% displayed minor or no ischemia. Furthermore, it concluded that using angiography-guided PCI did not reduce the risk of death, myocardial infarction, or other major cardiovascular events when added to optimal medical therapy consisting of pharmacologic therapy and lifestyle intervention [5].

1.2 Fractional Flow Reserve

In 1995, Pijls et al. introduced fractional flow reserve (**FFR**) as an index to evaluate the functional significance of epicardial coronary stenoses [6]. Theoretically, it is defined as the ratio of maximum flow through the stenotic vessel to maximum flow through the hypothetical healthy vessel. In clinical practice, it is determined by taking the ratio of pressure distal to the lesion to pressure proximal to the lesion during maximal hyperemia (Figure 2). Therefore, an FFR of 1.0 would indicate no reduction in flow while an FFR of 0.5 would indicate a 50% reduction in flow. We expect the pressure to scale linearly with the flow rate if the resistance is constant and minimized, which is achieved through

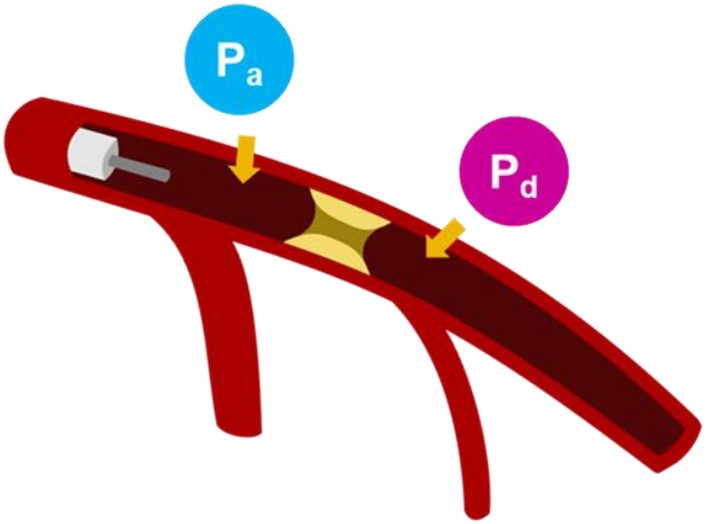

Figure 2: FFR measurement *in vivo*. Measurements must be acquired during maximal hyperemia to minimize downstream resistance. P_a, aortic pressure. P_d, distal pressure.

induction of hyperemia using an injected vasodilator—such as adenosine—and averaging measurements across multiple cardiac cycles [6].

Several studies have shown the benefits and efficacy of FFR in deciding who benefits from PCI. In 2007, the DEFER study investigated the effect of PCI in patients with functionally non-significant coronary stenosis, and found that there was no benefit to intervention in patients with FFR ≥0.75 [7]. The Fractional Flow Reserve versus Angiography for Multivessel Evaluation (**FAME**) study, published in 2009, found that revascularization only of ischemic lesions (i.e., those with FFR ≤0.80) was associated with 28% fewer major adverse cardiac events compared with an angiography-guided strategy [8]. Furthermore, the FAME II study, published in 2012, showed FFR-guided PCI to also improve patient outcomes when compared with optimal medical therapy alone [9]. In fact, *FFR is the only diagnostic method for guiding coronary intervention that has shown any benefit to patient outcomes to date.*

To measure FFR clinically, a pressure wire is inserted percutaneously from the femoral or brachial artery, through the aorta, and into the coronaries where proximal and distal pressures are measured directly across multiple cardiac cycles. These values are then time-averaged and divided to acquire FFR, and a threshold of 0.8 is used to determine which patients should receive revascularization. Despite its proven efficacy, clinical data of attempted coronary interventions of intermediate stenoses have shown that FFR is used in only 6.1% of patients while 73.6% of patients were evaluated with angiography alone [10]. This underutilization can be attributed largely to the extra time and cost of the pressure wire, as well as the small but non-negotiable risk to the patient. Therefore, there have been considerable efforts in recent years to develop non-invasive alternative methods of determining FFR.

1.3 Virtual Fractional Flow Reserve

Virtual fractional flow reserve (**vFFR**) is a generic term for non-invasive alternatives to FFR wherein medical images are used to create patient-specific models of the coronary vasculature and computational fluid dynamics (**CFD**) is used to numerically solve the governing equations of fluid mechanics and estimate FFR. To compute vFFR, certain boundary conditions must be defined in the patient-specific model, including: the lateral wall geometry which describes the coronary luminal boundary; the inlet flow rate to simulate hyperemic coronary blood flow; and flow-splitting ratios at vessel branch points.

1.3.1 Computed Tomography–Derived Fractional Flow Reserve

The first example of vFFR was computed tomography (**CT**)–derived FFR (**$\mathbf{FFR_{CT}}$**), described by Taylor et al. in 2013 [11]. FFR_{CT} uses CT angiography (**CTA**) to construct

an anatomical model of the coronary arteries and a mathematical model of the coronary physiology to derive boundary conditions based solely on morphometric laws and volumetric CT data [11]. Because CT is unable to measure flow directly, total coronary flow is defined as a function of myocardial mass [12], flow-splitting between vessels is determined through Murray's law [13], and lumped-parameter models are coupled to the aortic inlet, non-coronary vasculature, and coronary microcirculation [11].

In the Diagnosis of Ischemia-Causing Coronary Stenoses Obtained Via Noninvasive Fractional Flow Reserve (**DISCOVER-FLOW**) study, FFR_{CT} was computed in 159 vessels from 103 patients undergoing CTA, invasive coronary angiography, and FFR measurement, and diagnostic performance of FFR_{CT} was assessed in reference to invasive FFR. FFR_{CT} and FFR were found to be well correlated ($r = 0.717$, $p < 0.001$) with a slight underestimation by FFR_{CT} (0.022 ± 0.116, $p = 0.016$), and the area under the receiver-operator characteristics curve (**AUC**) was 0.90 ($p = 0.001$) [14].

Though FFR_{CT} allows for a non-invasive assessment of the functional significance of coronary stenosis, it does have several limitations inherent in CT. First, as mentioned previously, CT is unable to directly measure flow rate, requiring several assumptions to be made involving physio-morphic relationships and mean anthropometric data in order to estimate flow boundary conditions. Second, acquisition of CT volumetric data requires contrast injection and repeatedly exposing the patient to ionizing radiation. Third, CT is susceptible to blooming artifacts from calcium which can obstruct or artificially enlarge the vessel geometry.

1.4 Coronary Flow Reserve

A complimentary coronary physiologic measure to FFR is coronary flow reserve (**CFR**), which is defined as the ratio of hyperemic flow to basal flow [4]. In healthy individuals, CFR has been shown to be approximately 4.8, which indicates hyperemic flow is almost five times greater than basal flow [4, 15]. Unlike FFR, CFR is affected by both distal tissue bed vascular function and epicardial resistance, each of which can be assessed invasively by determining hyperemic microvascular resistance (**HMR**) and the hyperemic stenosis resistance (**HSR**), respectively [16]. For example, if the downstream small vessel vasodilation response is impaired, the HMR will increase and thereby reduce CFR. Similarly, to compensate for an increase in the HSR caused by CAD, the basal microvascular resistance (**BMR**) will decrease and reduce CFR, as the available coronary

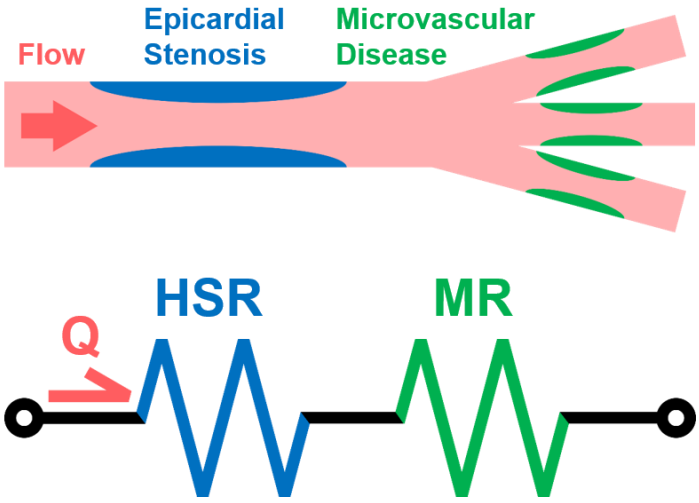

$$Q_B = \frac{\Delta P^B}{HSR}, \qquad Q_H = \frac{\Delta P^B}{HSR}$$

$$FFR = \frac{P_d^H}{P_p} = 1 - \frac{\Delta P^H}{P_p}$$

$$CFR = \frac{Q^H}{Q^B}$$

$$FFR = 1 - \frac{P_p}{\Delta P^B} CFR$$

Figure 3: Illustration of Coronary Flow Reserve (CFR). (a) Coronary arterial blood flow travels through both epicardial vessels and microvasculature. Each can contribute to the total resistance. The resistance due to the epicardial vessels (blue) is the stenotic resistance (HSR), and the resistance due to the microvasculature (green) is the myocardial resistance (MR). (b) The flow (Q) can be modeled using a circuit analogy in which the total resistance is the sum of the HSR and MR. (c) Flow through the vessel varies between basal ($Q_{\square}^{B}$) and hyperemic ($Q_{\square}^{H}$) conditions due to changes in the MR, but it can be expressed as the ratio of the pressure change (ΔP) across the stenotic epicardial vessel to the HSR. FFR is the ratio of the pressure distal to the lesion during hyperemic flow (P_d^H) to the proximal pressure ($P_{\square}^{\square}$), while CFR is the ratio of the hyperemic flow to the basal flow. Through these equations, the theoretical interdependence of CFR and FFR can be seen.

reserve is diminished [4]. Therefore, CFR and FFR are intrinsically connected, and an illustration of this interdependence can be seen in Figure 3. Because so many factors contribute toward patient-specific CFR, its value can vary substantially between patients. CFR can be measured clinically through magnetic resonance imaging (**MRI**) and positron emission tomography (**PET**) and can be estimated through single-proton emission computed tomography (**SPECT**). CTA, however, cannot measure CFR.

CHAPTER 2. TECHNICAL BACKGROUND

2.1 Phase-Contrast Magnetic Resonance

The phase φ of the magnetic resonance (**MR**) signal emitted from a spinning particle is determined as a function of the gyromagnetic ratio γ, the gradient strength over time $\boldsymbol{G}(t)$, the position of the particle over time $\boldsymbol{r}(t)$, and the duration of the gradient T as

$$\varphi = -\int_0^T \gamma \boldsymbol{G}(t) \cdot \boldsymbol{r}(t) dt.$$

From this equation, it can be shown that a stationary spin exposed to a pair of bipolar gradients will experience no net phase shift, but a moving spin will experience a net phase shift proportional to the component of the velocity coincident with the direction of the gradient. By imaging a slice once with a pair of bipolar gradients and once without, the difference of the two images will be the phase shift created by the moving spins, thereby allowing *in vivo* quantification of flow velocities [17, 18]. This is referred to as phase-contrast magnetic resonance (**PCMR**). Typically, only the through-plane velocity is measured so flow rate can be determined over cross-sectional area. It is possible to repeat or interleave PCMR measurements in three orthogonal directions to obtain the complete 3D, time-resolved velocity field.

2.2 Prospective Navigator Echo

Navigator echoes are additional RF-pulses used to dynamically track anatomic motion during image acquisition. For example, to mitigate the effects of respiratory motion, a navigator is often used to track the motion of the diaphragm, and image data are only acquired if the diaphragm is recorded as being within a small respiratory acceptance

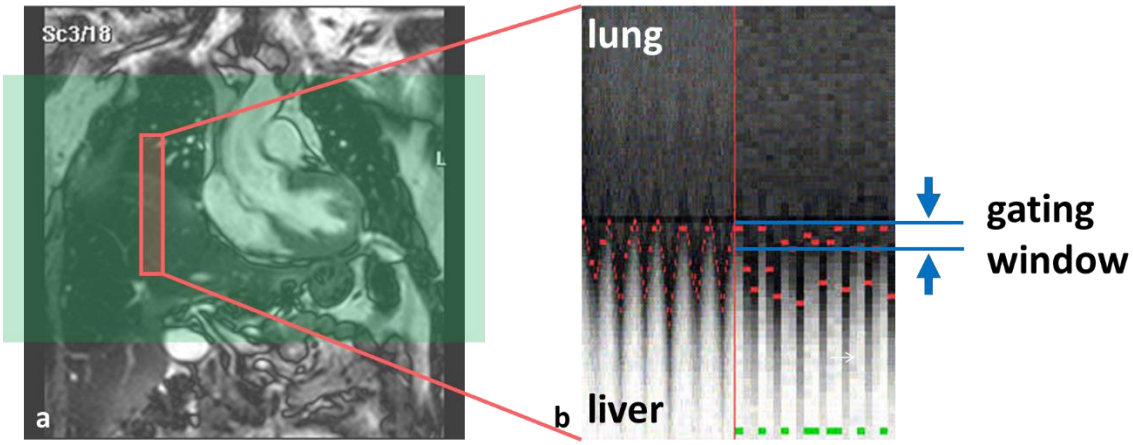

Figure 4: Prospective navigator-gating. (a) A one-dimensional beam is positioned over the right hemidiaphragm and is acquired prior to each potential image acquisition. (b) Edge detection determines if the respiratory position is within the gating window, and image acquisition occurs if it is.

window (Figure 4). Though this does effectively compensate for respiratory motion, it greatly lowers scan efficiency as only a fraction of cardiac cycles fall within this acceptance window, and scans can be unpredictably long and require extensive planning to correctly implement.

2.3 Self-Gating

Self-gating is a novel concept for motion-compensation during MRI in which motion information is derived directly from the image data themselves [19]. In the implementation used in this project, data acquisition is performed using a three-dimensional golden-angle radial *k*-space trajectory, beginning with a readout extending in a superior-inferior (**SI**) direction from the center of *k*-space [20]. Each SI line is then extracted and arranged temporally, and a one-dimensional Fourier transform is applied to create an SI projection of the image volume through which physiologic motion can be visualized (Figure 5).

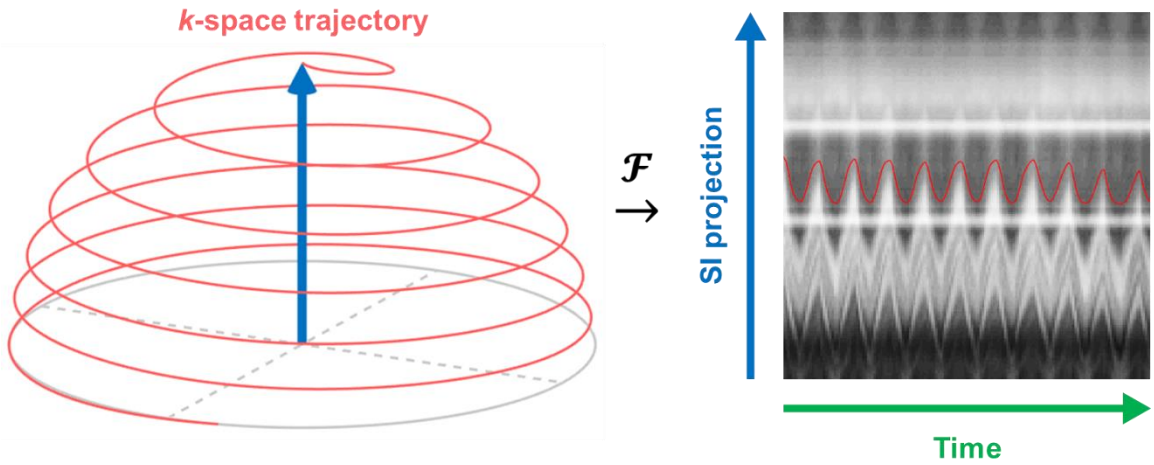

Figure 5: Representative image of self-navigated data acquisition and motion extraction. Data is acquired using a 3D spiral phyllotaxis trajectory (left) starting with a line oriented in the superior-inferior (**SI**) direction. The SI lines from each acquisition are then concatenated temporally, and a 1D Fourier transform is performed, allowing for the physiologic signal to be identified using principal component analysis (right).

Self-gating relies on the same basic principle used in conventional prospective navigation: physiologic motion is tracked in a single dimension, and imaging is gated such that overall motion within the image data is minimized. Self-gating, however, has advantages over the conventional prospective approach due to it being a retrospective method. With prospective gating, imaging only occurs when the motion is within the acceptance window, and this window must be manually set prior to the start of the scan. If the subject's breathing changes during the scan, several minutes can be wasted during which no data are collected. With retrospective gating, image data are acquired throughout the scan, and the motion-states are determined afterwards with consideration of the entire motion signal. This allows the total scan time to be much more predictable and requires less planning from the operator. There are several techniques which make use of the self-gating principle to compensate for motion in cardiac imaging. Some of these are described in the sections below. A visualization of how these techniques relate to one another can be seen in Figure 6.

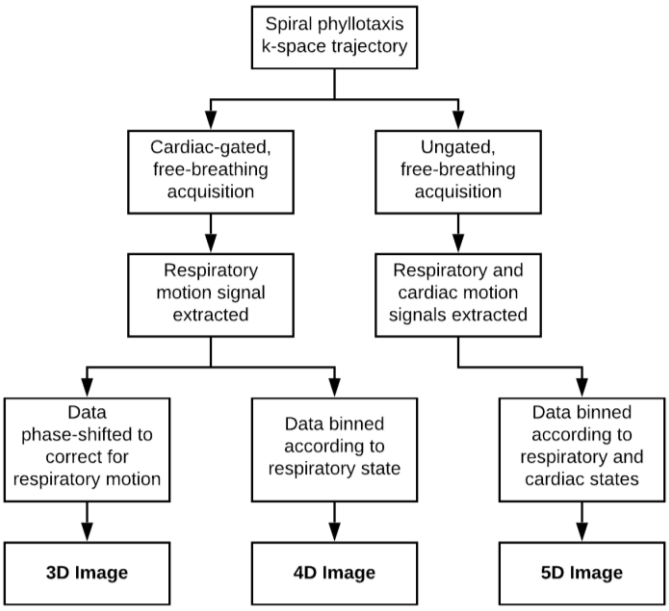

Figure 6: A graphical visualization of different implementations of self-gating.

2.3.1 Self-Navigated, Motion-Corrected Coronary MRA

Self-gating principles have been applied to cardiac and coronary imaging [21-24]. In its first iteration, prospective electrocardiogram (**ECG**)–gating was employed such that image data were only acquired during a single cardiac phase, typically end-systole or mid to late–diastole [21]. The bright-blood acquisition allows for the left ventricular (**LV**) blood pool to be tracked through self-navigation, and principal component analysis can then be used to extract the respiratory motion signal from the acquired data. Through the Fourier shift theorem, a translation in the image domain equates to a phase-shift in the frequency domain. Therefore, the acquired data are phase-shifted corresponding to their respective amount of respiratory displacement, followed by regridding and reconstruction of the final image volume. This allows for a free-breathing, whole-heart image acquisition which is prospectively cardiac-gated and retrospectively corrected for respiratory motion, thereby creating a fully motion-compensated image set.

2.3.2 XD-GRASP

A novel reconstruction framework called extradimensional golden-angle radial sparse parallel (**XD-GRASP**) MRI was recently proposed in 2016 [25]. Through it, image data are artificially undersampled by binning them into additional dimensions corresponding to different motion states, and compressed sensing techniques are then used to reconstruct the undersampled data.

2.3.3 4D-GRASP Coronary MRA

The principles of self-navigation MRA can be combined with XD-GRASP to create motion-resolved images of the coronary arteries [24]. If prospectively cardiac-gated raw image data and the respiratory motion signal are acquired through the methodology described in section 2.3.1, the acquired data can then be binned according to the respective respiratory position, thereby creating a fourth dimension (**4D-GRASP**). This will group data sets such that all sets acquired at end-inspiration are together, all sets acquired at end-

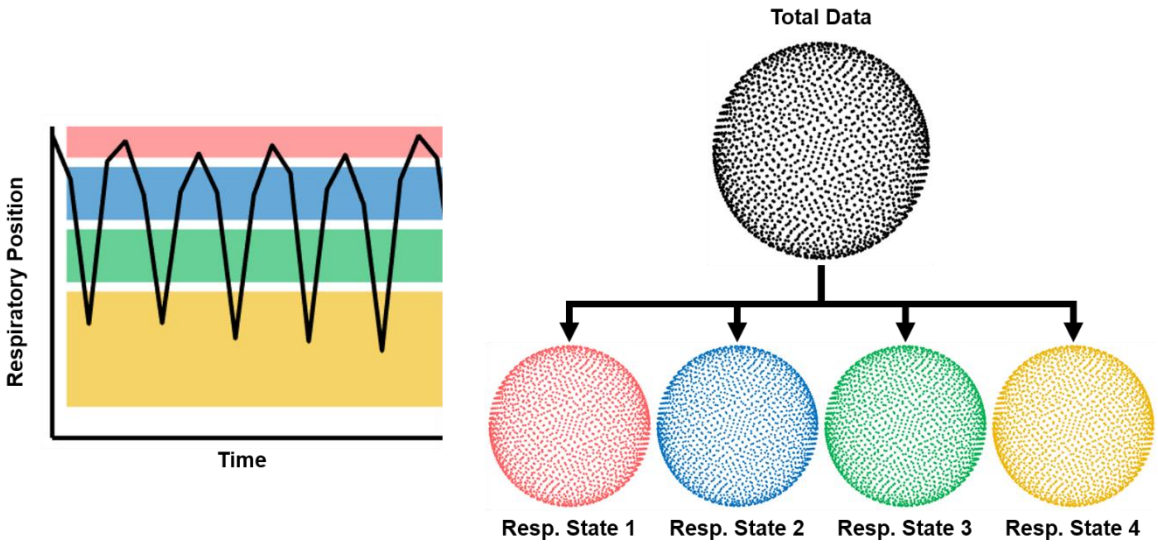

Figure 7: Representative image of 4D-GRASP binning. Respiratory motion is extracted from the image data, and data sets are binned according to relative respiratory position.

expiration are together, etc. (Figure 7). Once compressed-sensing reconstruction is completed, the resulting image set will be across four dimensions: three spatial and one respiratory. Within each bin, respiratory motion will be minimized, so no motion-correction is necessary prior to reconstruction. This method uses prospective cardiac gating so all respiratory motion states will be at a single cardiac phase.

2.3.4 5D-GRASP Coronary MRA

Another implementation of XD-GRASP is to bin datasets into both respiratory and cardiac dimensions, thereby allowing for five total dimensions (**5D-GRASP**) [26]. In the free-running framework (**FRF**) presented by Di Sopra et al. in 2019, image data are acquired continuously without any prospective gating or ECG-triggering [27]. This allows for collection of data throughout the subject's respiratory and cardiac cycles. The cardiac and respiratory cycles oscillate at different frequencies, allowing for the two physiologic

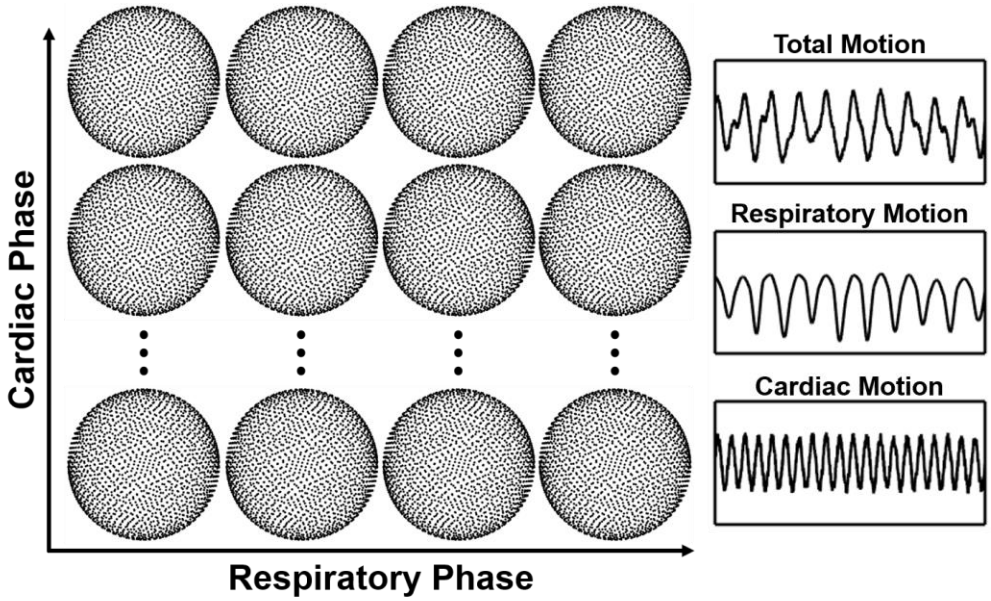

Figure 8: Representative image of 5D-GRASP binning. Data are acquired rapidly without gating, and the total motion is extracted from image data. Relative frequencies are used to separate respiratory and cardiac motion, and data are then binned.

signals to be separated, and data are then binned into a two-dimensional array of three-dimensional data sets (Figure 8). 5D-GRASP allows 3-dimensional reconstructed images of the heart at different temporal locations, providing new or potentially more accurate diagnoses to be performed. Furthermore, because the data are no longer prospectively binned, then the acquisition should be less sensitive to variations in the heart-rate during the scan.

CHAPTER 3. HYPOTHESIS AND SPECIFIC AIMS

3.1 Summary of Background

Revascularization for CAD using PCI has been shown to only benefit patients for whom the atherosclerotic plaques create a functionally significant stenosis, and FFR is the current gold-standard for making this determination. Despite its proven efficacy, FFR is underutilized due to its invasive and expensive nature. vFFR is a group of techniques that seek to develop non-invasive alternatives to FFR through patient-specific CFD modeling. The most notable example of vFFR is FFR_{CT}, which uses CT image data to directly characterize vessel morphology and indirectly estimate hyperemic flow. Hyperemic flow is necessary to accurately measure FFR as it enforces the condition of minimized downstream resistance. However, CT cannot quantify patient-specific CFR which defines this hyperemic behavior. MRI can directly measure flow velocities and determine *in vivo* through PCMR. Self-gating principles allow for physiologic motion to be measured from MR image data, which can then allow for either motion-correction or XD-GRASP and binning techniques to reconstruct a fully motion-resolved image set. Therefore, MRI appears specifically well-suited for vFFR calculation due to its ability to quantify both the patient-specific anatomy and flow.

3.2 Central Hypothesis

We hypothesized that MRI could acquire both the geometric and flow boundary conditions necessary to non-invasively calculate patient-specific vFFR using CFD.

3.3 Approach

Flow information can be quantified directly *in vivo* using PCMR, but its use in quantifying inlet flow boundary conditions for coronary arterial CFD simulations has not been sufficiently validated. Different implementations of vFFR—specifically FFR_{CT}—have made assumptions concerning what patient-specific flow information is necessary for the simulations, and these assumptions have also not been well validated. Therefore, we first determined what patient-specific flow information was necessary for accurate vFFR calculation, which was done through error assessment of vFFR calculated using different assumptions of hyperemic coronary flow. Then, flow through the coronary arteries was measured with PCMR in a set of volunteers and evaluated for consistency and repeatability with regards to the patient-specific flow information necessary for inflow boundary conditions.

Characterizing the coronary arterial luminal geometry through MRI had been shown to be possible [28], but it is often unreliable with prospective ECG and respiratory gating. Self-gating offers a novel technique for motion-compensation through retrospective gating and motion-correction, which could more consistently provide images suitable for coronary geometric characterization. Self-gating lends itself to multiple implementations for MRA. However, due to the complexity of implementation and recent appearance of the techniques, they have not been fully assessed for coronary imaging. Therefore, multiple techniques were applied to a cohort of patients undergoing clinically indicated cardiac MRI, followed by evaluation of image quality.

3.4 Aim 1: Determine If PCMR Can Provide the Inlet Flow Boundary Conditions Necessary for Calculation of vFFR Through CFD

3.4.1 Aim 1a: Determine What Inlet Flow Boundary Conditions Are Necessary for Calculation of vFFR through CFD

Clinical FFR is measured during maximal hyperemia, meaning that CFD should use the patient-specific hyperemic waveform as the inlet flow boundary condition to most accurately simulate flow through the coronary artery. However, because most imaging modalities cannot directly quantify flow, assumptions have been made in different implementations of vFFR. For example, FFR_{CT} uses the myocardial mass to estimate the time-average basal flow, then uses population-averages to predict the waveform and microvascular response to hyperemia. *We hypothesized that vFFR calculation is insensitive to the time-dependence of the flow waveform but requires patient-specific CFR*. We tested this through a series of CFD simulations comparing hyperemic, basal, and steady waveforms.

3.4.2 Aim 1b: Investigate if PCMR Can Be Used to Acquire the Inlet Flow Boundary Conditions for Calculation of vFFR

Aim 1a determined what patient-specific flow information was needed to calculate vFFR, and subsequently PCMR was investigated for its ability to quantify this information *in vivo*. PCMR was applied to measure flow through the left main artery, right coronary artery, and coronary sinus in a series of volunteers. Since we cannot know the true flow in human coronaries, measurements were analyzed for repeatability. *Two hypotheses were tested for this aim: 1) repeated measurements of coronary arterial flow will show internal-*

consistency, and 2) the combined measurements of coronary arterial flows within a specific patient will show agreement with coronary sinus flow measurements.

3.5 Aim 2: Determine if Self-Gated MRI Can Provide Image Quality Sufficient for Coronary Geometry Characterization

3.5.1 Aim 2a: Determine If Self-Navigation MRA Can Provide Image Quality Sufficient for Coronary Geometric Characterization

The self-navigation MRA protocol described in section 2.3.1—whereby images are acquired during prospective cardiac-gating, followed by retrospective correction to compensate for respiratory motion—was applied to a cohort of *patients* undergoing clinically indicated cardiac MRI. Images were acquired and image quality was assessed. *It was hypothesized that the retrospective respiratory motion–compensation technique used by self-navigation MRA could consistently provide full coronary geometric characterization.*

3.5.2 Aim 2b: Determine If 4D-GRASP MRA Can Provide Image Quality Sufficient for Coronary Geometric Characterization

The 4D-GRASP protocol described in section 2.3.3—whereby images are acquired during prospective cardiac gating, followed by binning according to respiratory state and reconstruction using compressed sensing techniques—was applied to a cohort of patients undergoing clinically indicated cardiac MRI. The raw data were also reconstructed using motion-corrected, self-navigation MRI. *It was hypothesized that the 4D-GRASP images would show improvement over self-navigation MRI through paired comparison.*

3.5.3 Aim 2c: Determine If 5D-GRASP MRA Can Provide Image Quality Sufficient for Coronary Geometric Characterization

The 5D-GRASP protocol described in section 2.3.4—whereby images are acquired during a free-running, continuous acquisition, followed by binning according to both respiratory and cardiac state and reconstruction using compressed sensing techniques—was applied to a cohort of patients undergoing clinically indicated cardiac MRI as well as a cohort of pigs. Three separate acquisitions were investigated, including a non-contrast acquisition, a gadolinium-enhanced acquisition, and a ferumoxytol-enhanced acquisition. Images were acquired and assessed for their ability to characterize the coronary geometry. *It was hypothesized that the ferumoxytol-enhanced images would perform better than the other two 5D-GRASP techniques, the 4D-GRASP technique, or self-navigation MRI.*

3.6 Outcomes

The first outcome of Aim 1 was a quantitative determination of what flow information is needed to calculate vFFR through CFD. Through this, the limitations on which imaging modalities may or may not be used for vFFR could be more objectively ascertained. This information was then used in the second half of Aim 1 to validate whether or not PCMR could acquire the requisite flow data. The primary outcome of Aim 2 was to investigate implementations of self-gated acquisition and reconstruction frameworks and quantify their capacity for three-dimensional coronary MRA. Each sub-aim was designed to test a specific implementation and determine if it could be used in calculating vFFR. When an approach did not succeed in this objective, we investigated what was the likely cause of failure and proposed the next implementation to test which should improve upon the last.

3.7 Significance and Innovation

CAD is the leading cause of death globally, and trends indicate that in the United States half of all healthy 40-year-old men and one in three healthy 40-year-old women will develop it in their lifetimes [29]. Currently, the only method proven to improve patient outcomes and survivability following revascularization for stable CAD is invasive FFR measurement. Despite its proven efficacy, it remains underutilized due to its associated costs and risks. A non-invasive alternative to FFR could allow clinicians to accurately assess the functional severity of coronary stenoses without requiring catheterization of the patient.

Early efforts to develop vFFR have focused on using CT due to its proficiency in imaging coronary arterial geometry. Despite excitement within the diagnostic and invasive cardiology community for FFR_{CT}, there are significant drawbacks for CT-based FFR. CT is not able to directly measure flow, which is a primary determinant of the pressure differential across the stenosis. Basal flow can be approximated from morphologic data and allometric scaling, but CT also cannot characterize the downstream myocardial tissue which determines distal resistance and contributes towards the patient-specific CFR. CT also suffers from beam-hardening artifacts which can cause an overestimation in the degree of stenosis or make the vessel geometry difficult or impossible to determine. Lastly, CT delivers a non-trivial dose of radiation for a diagnostic test, which poses a concern for its clinical use. The issues presented by the presence of calcium as well as the lack of patient-specific flow and CFR measurements have led to serious questions about the accuracy of FFR_{CT}. The overall per-vessel diagnostic accuracy of FFR_{CT} has been shown to be approximately 82%. However, 95% diagnostic accuracy was only seen for FFR_{CT} values

below 0.53 or above 0.93. In fact, for FFR_{CT} values between 0.70 and 0.80, the diagnostic accuracy fell as low as 46% [30]. This indicates that FFR_{CT} struggles primarily in accurately diagnosing patients with moderate ischemia, which are precisely the cases for whom accuracy is the most critical.

MRI, however, appears to have several advantages over CT in calculating vFFR. MRI does not use ionizing radiation, which could increase patient compliance and also enable use of vFFR in longitudinal studies or as an endpoint in treatment studies. Importantly from a fluid dynamics standpoint, MRI is able to determine flow velocity using the phase-contrast technique. This measurement can provide patient-specific input flow boundary conditions to the CFD model. Furthermore, PCMR can quantify the hyperemic behavior necessary to measure vFFR. It is known that CTA has a higher resolution than MRA for imaging the coronary arteries. However, the presence of calcium often mitigates these resolution advantages as the beam-hardening artifacts obfuscate the true stenosis geometry. Because calcium lacks mobile protons, however, these artifacts do not plague MRI as they do CT.

The first aim seeks to investigate a) what patient-specific flow information is necessary to calculate vFFR, and b) if PCMR is capable of acquiring this information. If it is seen that patient-specific hyperemic flow information is necessary to accurately quantify vFFR, then this would indicate that CT will always suffer from errors in quantifying vFFR due to its inability to quantify patient-specific CFR. Furthermore, while the ability of PCMR to quantify *in vivo* arterial flow has been proven previously, its specific application in quantifying coronary arterial flow is lacking in validation which this study will seek to provide.

The second aim investigates if self-gated MRI can sufficiently characterize coronary anatomic geometry for vFFR calculation. Self-gating is a novel technique with multiple implementations which show promise for applications where physiologic motion is present. These aims will attempt to investigate these implementations in coronary imaging of patients which have not yet been adequately studied.

The *major innovation* in this proposal is development of techniques that would enable a new, non-invasive method of determining vFFR with MRI. Having physiology-based coronary measurements in patients is critical for optimal patient management, but obtaining these measurements in the catheterization lab is time-consuming, expensive, and impractical on a routine basis. The ability to determine coronary physiology metrics non-invasively and without employing ionizing radiation would be a paradigm shift in guiding coronary intervention. The non-invasive nature of the test would allow FFR to be used to assess patient populations that could most benefit from PCI and also allow FFR to be used in trials to assess novel treatment therapies.

Multiple trials have shown the advantages of FFR-guided PCI for improving patient outcomes and for eliminating unneeded and expensive PCI procedures. However, due to cost, complexity, and reimbursement issues, FFR is not often employed in the catheterization lab. The development of an accurate, reproducible method of non-invasively determining FFR would dramatically increase its clinical use as the current barriers would be reduced. This would result in significant cost savings to the healthcare system by reducing the number of unnecessary catheterization procedures thus deploying stents only where they would benefit patient outcomes.

PCI requires high utilization of resources and use of individuals with a high level of clinical expertise. It is imperative to utilize these resources in a way that is most effective in improving and extending patients' lives. PCI guided by FFR yields improved patient outcomes for major adverse cardiac events compared to angiography-guided PCI. By removing the barriers of requiring an invasive test, we can dramatically increase the use of FFR, positively impact patient care, and improve allocation of cardiology resources to better serve the CAD population.

CHAPTER 4. DETERMINATION OF FLOW CONDITIONS NECESSARY TO CALCULATE VFFR

4.1 Introduction

To calculate vFFR through CFD, inlet flow boundary conditions must first be defined using a combination of patient-specific information and simplifying assumptions. For example, for FFR_{CT}, the subject is first imaged through CT which exclusively provides anatomic characterization. The total myocardial mass of the individual is estimated from the CT image data, which allows for an estimation of the patient-specific basal coronary arterial flow—that is, the flow through the coronary arteries when the subject is at rest—through allometric scaling [11]. The rationale behind this is that the rate of myocardial blood flow should be proportionate to the amount of myocardial tissue, and the ability to predict one with the other has been validated previously [12]. This relationship, however, only applies to basal coronary flow, while FFR is defined only during hyperemic—or stress—flow conditions.

To account for this, FFR_{CT} artificially scales the predicted basal flow by an estimated CFR value, which is done through modification of resistances in the overall lumped-parameter model. The epicardial resistance is automatically adjusted through the presence of a stenosis, but CFR is determined by both the epicardial and microvascular responses to stress, and CT has no means through which it can estimate patient-specific microvascular resistance. Therefore, the microvascular resistance is scaled by a factor of 0.25, which effectively assumes virtually no microvascular disease is present in the subject [15].

This assumption has not been validated or thoroughly investigated; however, it seems likely that it would weaken the predictive power of the technique. Because FFR is a measure of the pressure drop across the stenotic lesion and pressure gradient is directly related to the flow rate via Ohm's Law, it follows that any linear change in the inlet flow would likely result in a proportionate change in the calculated FFR. *Therefore, it is hypothesized that basal flow scaled by patient-nonspecific CFR cannot accurately calculate vFFR.*

Flow through the coronary arteries is naturally pulsatile, but hyperemia does not scale the flow waveform uniformly across the cardiac cycle, so scaling the basal flow by the patient-specific CFR will not produce the hyperemic flow waveform (Figure 9). Because of this, even if the patient-specific CFR is known, the simulated hyperemic flow would not be representative of the true hyperemic flow pattern. However, clinical FFR is

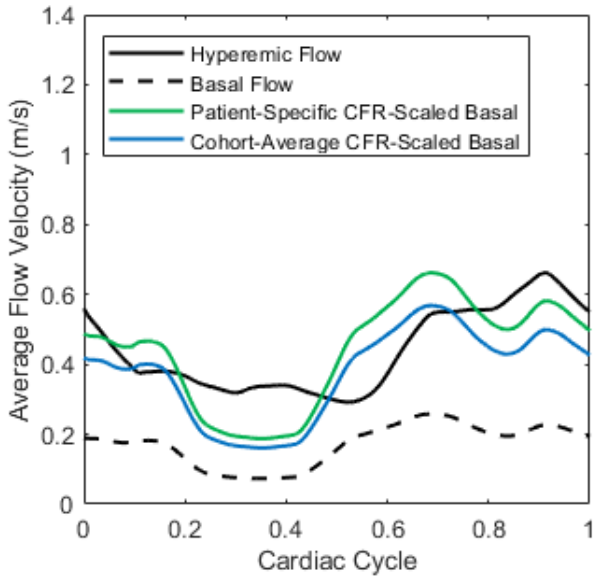

Figure 9: Representative flow waveform comparison for one patient. Both the basal and hyperemic flows were acquired using Doppler wire, and the basal flow was then scaled by a range of CFR values. When the basal flow is scaled by the patient-specific CFR—2.8—, the time-average flow rate is the same for both it and the hyperemic flow. Scaling the basal flow by the cohort-average CFR—2.2—produces the same basal waveform but with a different time-average flow rate from the hyperemic flow.

defined using the time-averaged pressure measurements, which, in theory, should not depend on the flow waveform used. *Therefore, it is hypothesized that scaling the basal flow by the patient-specific CFR should allow for an accurate calculation of vFFR.* In fact, by the same logic, time-dependent behavior should not influence the calculation of vFFR, meaning steady state flow simulations should provide the same estimation of vFFR as pulsatile simulations with the same time-averaged flow.

The purpose of this study is, therefore, to investigate the effect of varying CFR values on the accuracy of vFFR predicted from CFD. Specifically, we will use a coronary geometry determined by MRA coupled with basal and hyperemic coronary flow values measured by intra-coronary Doppler in a patient cohort undergoing physiologic evaluation of flow-limiting lesions in the catheterization lab. This allows for comparison of vFFR predictions using a clinically representative range of CFR values derived from patient-specific basal and hyperemic flow waveforms.

4.2 Methods

An overview of the experimental approach is presented below, followed by a detailed explanation of each component of the methodology. First, a coronary arterial computational model was constructed using MRA image data acquired from a single patient presenting with moderate CAD. Second, resting and hyperemic flows through the coronary arteries were measured in a separate cohort of patients (n=9) undergoing clinically indicated intracoronary Doppler ultrasound. Third, CFD was used to determine vFFR values with various applied hyperemic flow conditions, including: i) *in vivo* hyperemic flow by intra coronary Doppler (**true vFFR**), ii) basal flow scaled by the patient-specific CFR (**patient-scaled vFFR**), and iii) basal flow scaled by population-

average CFR estimates (**population-scaled vFFR**). The scaled vFFR values were predicted under both steady and transient flow conditions. These scaled vFFR values were compared with the true vFFR values to assess accuracy, correlation, and concordance, thereby evaluating how changing the hyperemic flow response—as measured by CFR—as well as time-dependent flow patterns affect vFFR prediction with a constant geometry. A graphical flowchart of these methods can be seen in Figure 10. The study was approved by the Institutional Review Board (**IRB**), and written informed consent was obtained from all subjects prior to either magnetic resonance scanning or intracoronary Doppler measurement.

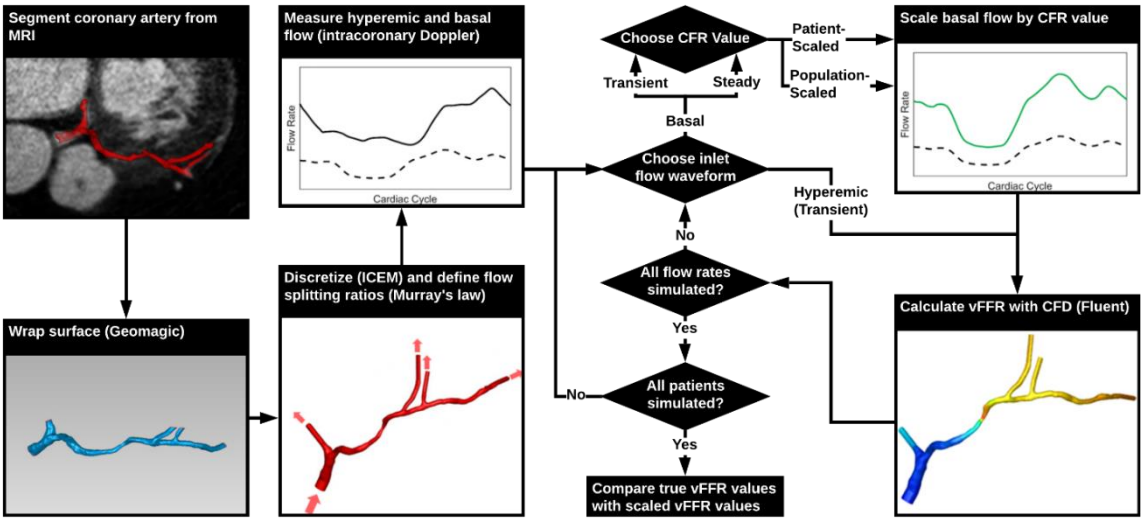

Figure 10: Overview of Aim 1a Experimental Design. A single left coronary artery tree was acquired from an MRI of a patient with a 50% stenosis in the LAD. Hyperemic and basal flow waveforms were measured in patients (n=9) with mild CAD using intracoronary Doppler. Each hyperemic flow waveform was applied as an inflow boundary conditions for the anatomic model to determine the true vFFR value via CFD. Each basal flow waveform was then scaled by either a patient-specific or estimated CFR value to approximate the hyperemic flow. These scaled flow rates were then applied as inflow boundary conditions to both steady and transient CFD simulations to estimate vFFR—i.e., CFR-scaled vFFR. These CFR-scaled vFFR values were then compared to the true vFFR values.

4.2.1 Coronary Anatomy Model Geometry

A patient presenting with NYHA class III ischemic heart failure was imaged prior to cardiac resynchronization therapy as part of an IRB-approved study [31]. Imaging was performed on a 3 T MRI scanner (MAGNETOM Trio, Siemens Healthcare) using a six-element phased-array cardiac coil. A 3D, whole-heart, navigator- and ECG-gated inversion-recovery FLASH sequence with a centric *k*-space trajectory acquired coronary images in the transverse plane at a resolution of 0.64 x 0.64 x 0.75 mm^3. Images were acquired in diastole during the slow infusion of a gadolinium-based contrast agent [32]. The left main (**LM**), left anterior descending (**LAD**), and left circumflex (**LCX**) arteries were segmented from the image data using a Frangi vessel enhancing post-processing filter followed by a colliding fronts segmentation algorithm (Vascular Modeling Toolkit) [33-35]. The resulting triangulated surface geometry was imported into Geomagic (Geomagic, Inc.) to generate a smooth 3D surface. This surface was imported into ICEM meshing software (ANSYS, Inc.) to generate the 3D computational mesh. The model was generated with approximately 100,000 tetrahedral elements and 150,000 six-node pentahedral elements comprising eight boundary layers with a linear growth factor of 1.1 such that each innermost element was the same volume as the adjacent tetrahedral element. Flow extensions were added to the inlet and each outlet by projecting the edge contour in line with the local trajectory of the boundary surface (Figure 10).

4.2.2 Coronary Flow Measurements

Intracoronary Doppler flow measurements were acquired in the LAD of patients (n=9) with mild CAD that participated in a previous IRB-approved study described elsewhere [36, 37]. Briefly, a coronary guide catheter was introduced into the ostium of

the coronary artery, and a 0.014-in pressure and Doppler flow velocity monitoring guidewire (ComboWire, Volcano Corp) was advanced through the catheter into the proximal, non-tortuous portion of the vessel to measure the inlet basal (resting) velocity. Subsequently, 140 $\mu g \cdot kg^{-1} \cdot min^{-1}$ intravenous adenosine was infused for 3 minutes to induce maximal coronary hyperemia, allowing for hyperemic velocity measurement.

4.2.3 Hyperemic Flow Conditions for CFD Simulations

Various hyperemic flow conditions were applied to evaluate their effects on computed vFFR values. The first condition was the pulsatile hyperemic flow measured *in vivo* for each patient, which was used to define the **true vFFR** against which the other predicted vFFR values would be compared.

Next, the patient-specific CFR value was calculated by taking the ratio of time-averaged, Doppler-wire measured hyperemic-to-basal flow rates across the cardiac cycle. For each patient, the measured basal flow was scaled by the patient-specific CFR value to give a flow waveform with the same time-averaged flow rate as the measured hyperemic flow (Figure 9). This flow was used to compute the **patient-scaled vFFR**.

For each patient, the basal flow rate was also scaled by a series of global CFR estimates which were not specific to the patient. A total of ten global CFR values were used, including nine values ranging from 1.0 to 5.0 by increments of 0.5 and a tenth value representing the average CFR across the patient cohort. These values were chosen to represent the scope of physiologically relevant CFR values in patients presenting with CAD. These flows were used to compute a series of **population-scaled vFFR** values for each patient. The specific population-scaled vFFR found using the cohort-average CFR was termed the **cohort-scaled vFFR**.

4.2.4 CFD and FFR Calculation

CFD simulations were run using Fluent (ANSYS, Inc.). While the true vFFR was computed only under transient flow conditions, the patient-scaled vFFR and population-scaled vFFR values were computed using both transient and steady conditions. For each of the nine patients on whom intracoronary flow measurements were obtained, 23 vFFR values were computed: the true vFFR found under transient flow, the patient-scaled vFFR found under both transient and steady flow, and the 10 population-scaled vFFR values found under both transient and steady flow.

For each case, the simulated hyperemic flow rate was prescribed as a blunt inlet flow boundary condition, inlet pressure was set at 100 mmHg, and outlet flow-splitting conditions were determined using Murray's law [13]. For the transient flow cases, the solution was computed across three cardiac cycles comprising 300 time steps, each at a heart rate of 60 beats per minute. Blood was modeled as Newtonian with a density of 1060 $kg \cdot m^{-3}$ and dynamic viscosity of 0.0035 $Pa \cdot s$. We used the SIMPLE algorithm for pressure-velocity coupling and second-order Green-Gauss node-based discretization for momentum and pressure. For each time step, convergence was achieved once the residuals of momentum and continuity fell below 10^{-5}. The computed pressure was then sampled along the centerline of the vessel and divided by the inlet pressure to calculate vFFR along the length of the vessel, in accordance with clinical practice. The clinically relevant vFFR value—found 4 mm distal to the region of minimal lumen area —was then recorded as the true vFFR. In the transient cases, the computed vFFR values were time-averaged to produce a single value.

4.2.5 Statistical Analysis

Continuous data are reported as mean ± standard deviation. Across all scaled CFR values, the difference between the true vFFR value and scaled vFFR was calculated. The error from each CFR group was evaluated by a Fisher-Pitman permutation test for matched-pairs at a significance level of 0.1. Correlation between scaled vFFR and true vFFR values for each patient was evaluated by calculating the Pearson correlation coefficient and the Spearman's rank correlation coefficient at a significance level of 0.001. Lastly, concordance was evaluated through a Bland–Altman analysis and calculation of Lin's concordance correlation coefficient [38, 39].

4.3 Results

4.3.1 Transient CFD Results

The CFR values for the cohort ranged from 1.45 to 2.87 with a mean value of 2.18 ± 0.55. The difference between the various scaled vFFR values and the true vFFR (vFFR

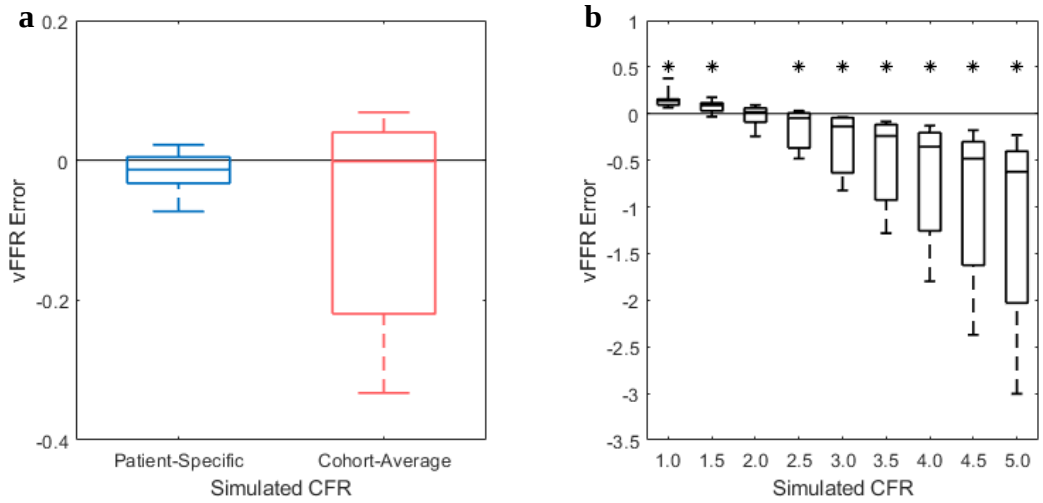

Figure 11: Results from transient CFD simulations for error in predicting true vFFR using different simulated hyperemic flow conditions. (a) Error of patient-scaled and cohort-scaled vFFR in predicting true vFFR. (b) Error for population-scaled vFFR across global CFR values ranging from 1.0 to 5.0. * indicates $p < 0.1$.

error) was determined across all 9 patients. Paired comparison of the patient-specific vFFR with the true vFFR produced the lowest mean error and standard deviation (-0.02 ± 0.03, $p > 0.1$) of the groups tested (Figure 11a). The cohort-scaled vFFR did not show significant differences with true vFFR (-0.08 ± 0.15), but its paired difference did show a much wider standard deviation than was seen with patient-specific vFFR (Figure 11a). The population-scaled vFFR values for global CFR ranging from 1.0 to 5.0 displayed significant error for nearly all values (Figure 11b). For example, using a CFR of 1.0—i.e., the unscaled basal flow—resulted in a mean difference of 0.15 ± 0.09; using a CFR of 4.8—the average value for the healthy population—gave a difference as large as -0.66 ± 0.64 [4, 15]. Aside from the cohort-scaled vFFR, the only other population-scaled vFFR which did not exhibit significant difference with true vFFR was the group tested with global CFR of 2.0 (-0.03 ± 0.11) which can likely be attributed to it being so close to the cohort-average CFR of 2.18.

The patient-scaled vFFR also showed the greatest bivariate correlation ($r^2 = 0.98$, $p < 0.001$), rank correlation ($\rho = 0.93$, $p < 0.001$), and concordance ($\rho_c = 0.98$) with true

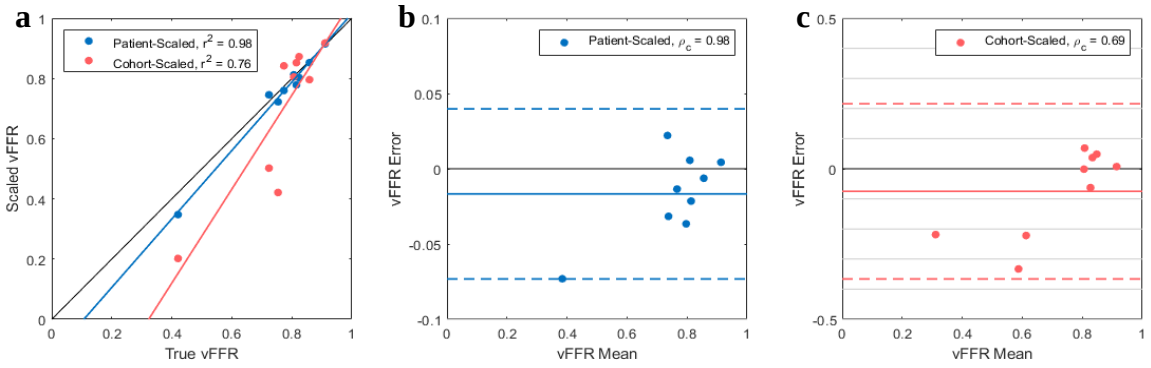

Figure 12: Correlation and concordance of true vFFR and scaled vFFR. (a) Correlation between true vFFR and scaled vFFR from transient CFD simulations. (b, c) Bland-Altman plots evaluating concordance of true vFFR with patient-scaled and cohort-scaled vFFR, respectively, estimated during transient CFD simulations.

vFFR of the groups tested (Figure 12a,b). Though cohort-scaled vFFR showed nonsignificant mean error, it does not show a high predictive power for true vFFR (r^2 = 0.76; ρ = 0.8; ρ_c = 0.69) (Figure 12a,c). Interestingly, the bivariate correlation for the population-scaled vFFR values estimating true vFFR were only seen to fall between 0.75 and 0.79, and the rank correlation was found to be 0.8 for every group. Unlike the correlation, the concordance with true vFFR was seen to vary for the population-scaled vFFR groups, with CFR of 2.0 showing the best agreement (ρ_c = 0.79) and CFR of 5.0 showing the worst (ρ_c = 0.10).

4.3.2 Steady-State CFD Results

Similar results were seen from the steady vFFR predictions. The patient-specific CFR again showed the lowest mean error and variance (0.00 ± 0.01, p > 0.1) and the greatest predictive power (r^2 > 0.99; ρ > 0.99; ρ_c > 0.99). CFR of 2.2—the patient

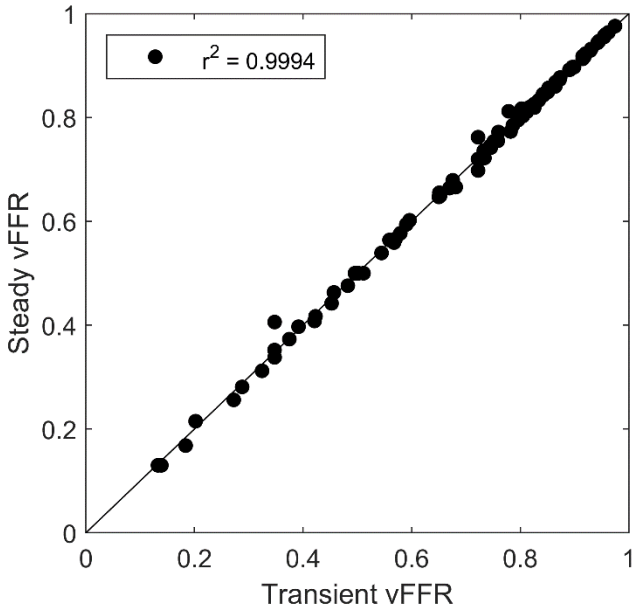

Figure 13: Correlation between steady and transient vFFR values across all simulations (n = 99).

average—and 2.0 were the only nonspecific CFR values which produced nonsignificant error, but all nonspecific groups showed only moderate predictive power ($0.74 < r^2 < 0.76$; $\rho = 0.8$; $0.1 < \rho_c < 0.8$). Direct comparison of the vFFR values predicted from steady simulations with those predicted from the transient simulations show a very strong predictive power ($r^2 = 0.9994$) (Figure 13).

4.4 Discussion

The major findings of this study are: 1) scaling the basal coronary flow waveform by the patient-specific CFR yields equivalent vFFR results to using the actual measured hyperemic flow waveform, 2) using a population average CFR for scaling will *on average* yield accurate vFFR results but will not provide predictive results for individuals whose CFR deviates from the average, 3) steady-state CFD estimates of vFFR are equivalent to transient CFD estimates for a given CFR value.

Myocardial ischemia can result from epicardial disease, microvascular disease, or a combination of both. Clinical indication for intervention on epicardial stenosis has been shown to be most successful when guided by the FFR, which approximates the reduction in flow through a given vessel due to an anatomic narrowing. Accurate measurement of this flow reduction relies on the assumption of maximal hyperemia, in which the downstream microvascular resistance is minimized. The physiologic response to hyperemia is, however, patient-specific, and depends on both the stenotic resistance contributed by the epicardial vessels and the downstream hyperemic microvascular resistance. Though it is possible to estimate the value of HSR through anatomic measurements and allometric scaling, HMR can only be measured through direct quantification of flow [16]. Though the comorbidity of both epicardial and microvascular

coronary disease is not uncommon, the presence or severity of one cannot be used as a direct indicator of the presence or severity of the other. In 2017 it was shown that as few as 68% of patients with moderate coronary stenosis had concordant FFR and CFR findings [16].

vFFR is an emerging methodology that seeks to provide a non-invasive alternative to invasive catheter-based FFR. Arguably the most well-known of these approaches is FFR_{CT} [11]. As CT is incapable of quantifying the CFR or HMR, its flow boundary conditions rely on population-average physiologic responses to hyperemia. Though results of this methodology for vFFR have shown some success in predicting invasive FFR, the correlation between the two measurements does not indicate strong correlation (r^2=0.54), and its diagnostic accuracy has shown to suffer substantially when predicting FFR values near the clinical cutoff (0.80) where specificity is most needed by clinicians [30]. It is possible that these limitations in efficacy are due at least in part to the assumptions made regarding HMR and, by extension, CFR.

Scaling the basal flow waveform by the time-averaged, patient-specific CFR does not replicate the exact hyperemic time-dependent flow waveform for a given patient. This is due to the interactions between the myocardium and the microvasculature, resulting in phasic fluctuations of the intracoronary resistance [40]. Since the intracoronary resistance is not uniform across the cardiac cycle during resting flow, it has varying levels of response to hyperemic induction as well, resulting in a time-dependent CFR, which can be seen in Figure 9. However, because FFR is calculated as the time-averaged ratio of distal and proximal pressure in the coronary, it is effectively insensitive to temporal fluctuations and depends only on the time-averaged flow rate and epicardial anatomy. Therefore, vFFR

predicted with either the hyperemic flow waveform or the basal waveform scaled by the patient-specific CFR was found to be nearly identical. This means that to define the boundary conditions necessary for computing vFFR, inlet coronary flow during hyperemia does not need to be obtained directly and can instead be approximated using basal coronary flow measurements and patient-specific CFR.

Because we found that vFFR would be insensitive to temporal fluctuations, it follows that running steady-state simulations using the time-averaged hyperemic flow would similarly provide accurate predictions of hyperemic vFFR. In fact, vFFR calculated with the time-averaged hyperemic flow rate was seen to predict hyperemic vFFR with the same accuracy as the transient CFD simulations. These results agree with those published by Morris et al. in 2017 who developed a "psuedotransient" methodology to calculate time-dependent vFFR values driven by values calculated from a steady CFD solution[41]. Their psuedotransient vFFR values showed strong correlation with the fully transient vFFR because the time-average results show negligible difference. Because the time-average FFR value is used as the primary indicator for clinical guidance, this supports that a steady-state analysis is sufficient. The implications of this are twofold. First, computation time for steady conditions is significantly lower than for unsteady conditions, allowing for utilization of stricter convergence criteria and for results to be returned much more quickly to the clinician. Second, it means that only the time-averaged basal coronary flow and CFR are needed to fully define the inflow boundary condition, and this information may be significantly easier to obtain *in vivo*.

Though the calculation of vFFR appears to be time-insensitive, it is still sensitive to changes in time-averaged flow over the cardiac cycle. Scaling the basal flow by some

non-patient-specific CFR values near the population average produced vFFR values that were, on average, not significantly different from hyperemic vFFR, but deviations from the population average resulted in increasingly large deviations in estimating vFFR. Predictive power of CFR-scaled vFFR for hyperemic vFFR was never strong for any estimated CFR value, and correlation was independent of the estimated CFR as well. This indicates that patient-specific characterization of the hyperemic flow rate needs to be used to accurately predict vFFR. Therefore, the choice in imaging modalities is limited to those that can measure both anatomy and flow. One could use a combination of imaging modalities to accomplish this, such as using both CT—to acquire the coronary anatomy and estimate the basal coronary flow rate through allometric scaling as described by Choy and Kassab [12]—and positron emission tomography (PET)—to assess the patient-specific CFR and determine the hyperemic response [42]. Perhaps a more feasible clinical solution would be to use MRI which can acquire both the anatomy and flow directly.

There are limitations to this study. All comparisons were made between vFFR values without comparison with true, invasive FFR. Though the intracoronary Doppler used to measure the flow also acquired the necessary pressure information to obtain invasive FFR, a direct comparison between the vFFR and FFR would not have been appropriate due to the fact that we used a single patient geometry from a subject where flow was not measured. The geometry was kept constant throughout all simulations to remove it as a variable and focus on how the model was sensitive to the inflow boundary condition, but this resulted in an inability to directly validate these measurements against invasive ones.

4.5 Conclusion

This study found that using patient-specific CFR to scale the basal flow waveform can accurately predict the vFFR calculated with the hyperemic flow, while using patient-nonspecific CFR to scale the basal waveform cannot accurately predict vFFR for individual patients. It was also found that steady simulations can predict vFFR accurately compared with unsteady simulations. These results are important for future work in quantifying vFFR in patient studies. The necessity for having patient-specific hyperemic flow behavior means that assumptions about CFR cannot be used to scale the patient's basal flow prior to its use as a boundary condition without significantly sacrificing the model's predictive power. The results also show that it would only be necessary to acquire the time-average basal flow rate and the patient-specific CFR, which could prove to be significantly easier than directly measuring time-dependent hyperemic flow behavior.

CHAPTER 5. INVESTIGATION OF CORONARY PCMR

5.1 Introduction

Nuclear magnetic resonance stems from Larmor's equation which relates the angular momentum of a particle to its gyromagnetic ratio and the strength of an externally applied magnetic field [43]. Spatially varying the magnetic field causes protons at different locations to spin at different speeds, thereby encoding spatial information into recorded signals and allowing for MRI. When spinning protons are exposed to a bipolar magnetic gradient—two gradients of equal magnitude but opposite direction—a phase shift is encoded into the spins. For stationary particles, the phase shift induced by the first half of the gradient is undone by the second half. However, for a moving particle, the phase shifts induced by each half of the gradient will not be equal in magnitude as the applied magnetic field will vary with the particle's location. Therefore, a net phase shift will be created in the particle, proportionate to the particle's average velocity over the duration of the applied bipolar gradient. This is the underlying principle which allows for PCMR to directly quantify velocity *in vivo* [17, 18, 44].

In clinical cardiac scans, the most common implementation of PCMR is single slice, time-resolved one-dimensional velocity-encoding phase-contrast MRI (**2D PCMR**), which is typically acquired during a breath-hold. Data are acquired in one plane of interest with velocity encoded into a single direction. For quantifying arterial blood flow, this plane would be positioned normal to the vessel with velocity encoded in the through-plane direction (Figure 14) (Figure 15). Having the patient hold their breath removes breathing

motion from the image, and ECG-gating is used to correctly align the acquired data into their discretized time phases across the cardiac cycle.

Navigator-gating can be employed to allow for a free-breathing approach. As described in section 2.2, the navigator records the position of the diaphragm, and imaging is prospectively-gated to only occur when it is in a user-defined position. For whole-heart imaging, this can be very problematic due to the quantity of data needed for the acquisition, but PCMR requires much less data which makes navigator-gating a viable option for respiratory motion compensation. Time-resolved, three-dimensional phase-contrast MRI (**4D PCMR**) is a novel application of navigator-gated PCMR in which velocities are measured across time in three orthogonal velocity encoding directions [45].

In Chapter 3, it was concluded that to accurately calculate vFFR, patient-specific hyperemic flow information is necessary in addition to the patient-specific geometry. MRI becomes an obvious candidate as the imaging modality for vFFR due to its ability to measure velocity directly. Using PCMR to quantify arterial blood flow *in vivo* has been theoretically and experimentally validated in multiple studies, and has been used as a staple of cardiovascular imaging for decades [17, 18, 44, 46]. Its specific utilization in the coronary circulation, however, has not been well validated. *Therefore, it is the purpose of this study to determine if PCMR can be used to measure blood flow in the coronary circulation such that the boundary conditions necessary for vFFR calculation can be determined.*

Because only time-averaged hyperemic arterial flow is needed to accurately calculate vFFR, there are two potential options available to acquire the needed information through PCMR:

1) The time-resolved hyperemic arterial inflow waveform can be measured directly, averaged across time, and then applied as the inlet flow boundary condition. Doing so, however, is clinically impractical due to the constraints on adenosine administration.

2) The time-resolved basal arterial inflow waveform can be measured directly and averaged across time. Then, the patient-specific CFR can be acquired through PCMR of the coronary sinus, and the basal flow rate can be scaled linearly to acquire an approximation of the hyperemic arterial flow rate.

Though direct measurement of coronary arterial flow through PCMR has not been well validated, its use in the coronary sinus has been shown to be reliable [47-49]. Therefore, to determine if PCMR can directly quantify coronary arterial flow rates, the following two hypotheses were tested with regard to PCMR: 1) repeated measurements of coronary arterial flow will produce repeatable time-averaged flow rates, and 2) the sum of the time-averaged flow rates in the LM and right coronary artery (**RCA**) will equal the time-averaged flow through the coronary sinus.

5.2 Methods

Coronary flow was measured in seven volunteers (age 20-65, five female) with no previous history of cardiovascular disease. Arterial flow was measured in a total of 13 vessels (six LM, seven RCA), and venous flow was measured in seven coronary sinuses. Informed consent was obtained prior to MRI scans and the study was approved by the university's IRB. All scans were performed on a 3 T scanner (MAGNETOM Prisma^{fit}, Siemens Healthcare) with a multi-element array coil.

To plan the coronary flow measurements, a stack of 192 transverse slices were acquired over the heart during mid-diastole using a navigator-gated 3D whole-heart coronary MRA sequence [32, 50]. The navigator beam was placed in the superior-inferior orientation over the right hemi-diaphragm and was acquired at the start of each cardiac cycle. An acceptance window of 3 mm was used to prospectively gate the acquisition to end-expiration. Total time for the MRA stack was approximately 10-20 minutes during free-breathing. Following acquisition, multiplanar reformation (**MPR**) was performed on the motion-resolved image volume to isolate 2D planes which passed perpendicularly

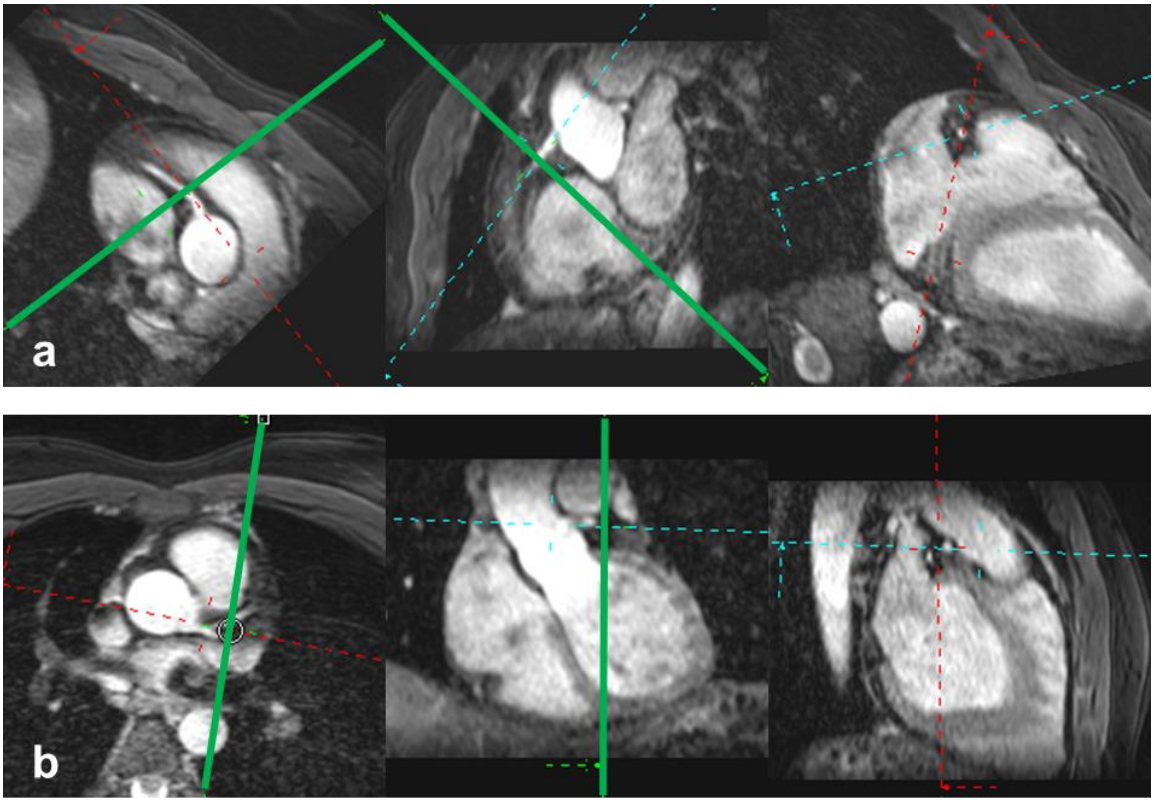

Figure 14: Example images for planning coronary PCMR acquisition. (a) MPR to isolate through-plane view of the RCA. (b) MPR to isolate through-plane view of the distal LM and proximal LAD and LCX, following bifurcation of the LM. In each, the green line indicates the intersection of the acquisition slice used in the flow measurement.

through the ostia for each of the LM, RCA, and coronary sinus. Example images from one volunteer can be seen in Figure 14.

The PCMR sequence used for the study was a modification of a navigator-gated 4D PCMR sequence [45], but set to acquire a single slice with only through-plane velocity measurements. A navigator approach was used to increase the effective resolution of the scan without creating fold-over artifacts or mandating a very long breath-hold. Again, a navigator beam was placed over the right hemi-diaphragm to acquire at the beginning of each cardiac cycle as determined through R-peak detection in the subject's ECG. An acceptance window of 1 mm was used to prospectively gate the acquisition to end-inhalation. If the respiratory position was recorded to be within the acceptance window, PCMR measurements were acquired across the entire cardiac cycle and were binned into approximately 25 temporal phases depending on the subject's heart rate. The velocity encoding (**VENC**) parameter was set between 40 and 70 cm/s according to the subject-specific coronary flow to maximize the dynamic range without introducing aliasing artifacts. Each pixel was 1 mm^2, and the field-of-view (**FOV**) and matrix size were variably set for each subject to ensure no fold-over artifacts would occur in the image. Acquisition

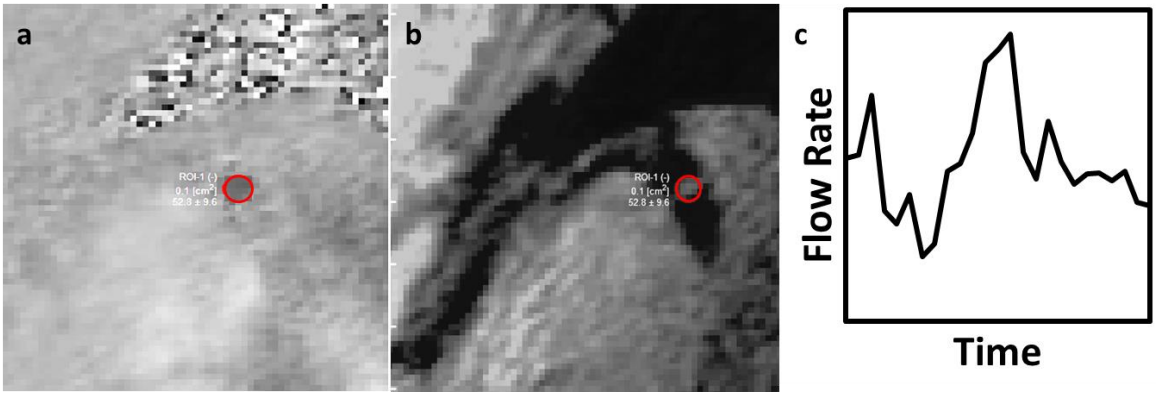

Figure 15: Representative image of coronary PCMR flow quantification. (a) Phase image with RCA segmented in red. (b) Magnitude image with RCA segmented in red. (c) Resultant flow waveform following segmentation of RCA at all time points.

time for each PCMR scan was approximately five minutes during free-breathing, and measurements were acquired for each vessel twice.

Following data acquisition, images were exported offline and analyzed using the freely available software Segment version 2.0 [51]. For each image stack, the magnitude and phase images were coupled and used to identify the luminal contours of the target vessel. A constant region-of-interest (**ROI**) was used across each temporal phase, and the ROI size was maintained when evaluating repeated measurements of the same vessel. Static tissue regions at the chest walls were automatically identified and used to calculate a second-order polynomial map to represent the estimated phase error induced by eddy current effects and correct for this [51]. The through-plane velocities of the pixels contained within the ROI were then added to provide a time-dependent flow waveform, from which the time-averaged flow rate could be recorded. An example image showing the vessel segmentation and flow waveform extraction can be seen in Figure 15.

To compare the arterial flow rates against the already validated coronary sinus measurements, the coronary arterial flow rates were added together, and the sum was compared against the corresponding coronary sinus flow rate. Because duplicate measurements were acquired in several of the vessels, all combinations of arterial and sinus flow rates were tested individually for correlation, and the best and worst performing sets were selected to provide upper and lower bounds for the solution.

5.3 Results

A total of 24 coronary artery (13 RCA, 11 LM) and 12 coronary sinus flow measurements were acquired across the five volunteers. Average arterial flow was 0.058 ±

0.030 L / min (0.045 ± 0.028 for RCA, 0.073 ± 0.025 for LM), and average sinus flow was 0.122 ± 0.048 L / min. Repeated flow measurements were acquired on 11 coronary arteries, and Pearson's correlation coefficient for the matching pairs was calculated to be r = 0.97 which is a strong indication of repeatability (Figure 16a). In six volunteers, both coronary arterial flow rates and the coronary sinus flow rate were measured. The sums of the arterial flow rates were plotted against the sinus flow rates, and the correlation coefficient for the relationship was estimated to be between 0.94 and 1.0 (Figure 16b,c). Bland–Altman analysis of these measures was also performed, and the concordance coefficient was estimated to be between 0.93 and 1.0 (Figure 16d,e).

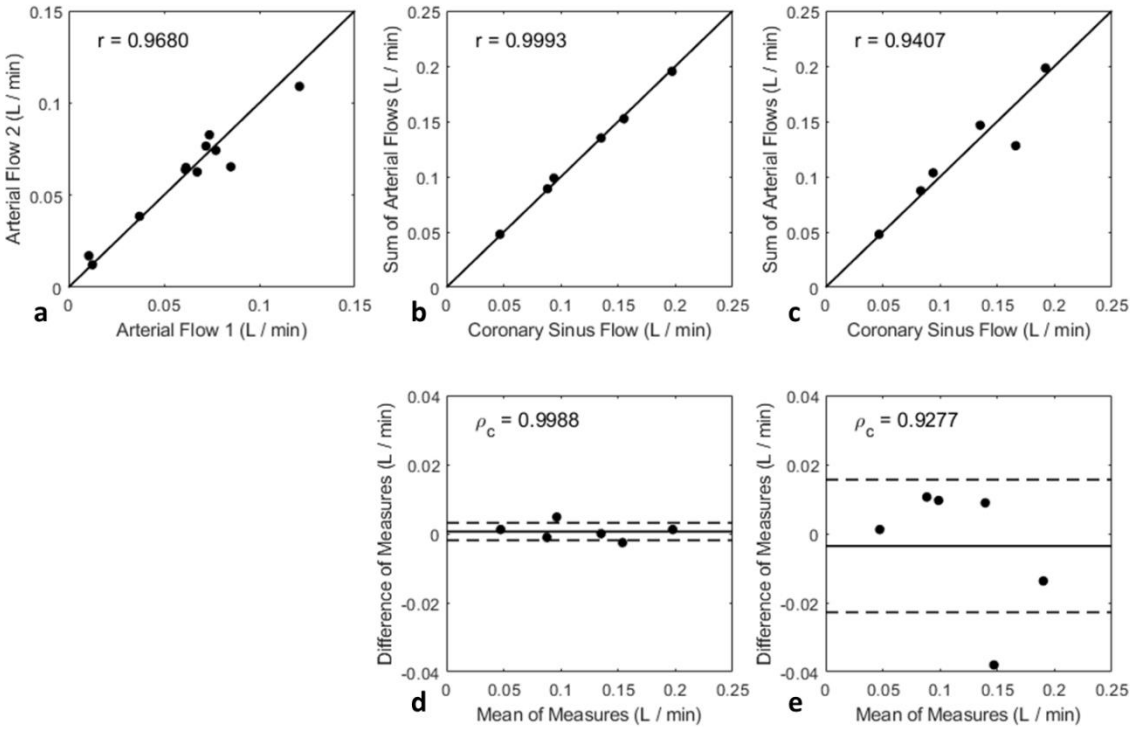

Figure 16: Coronary PCMR flow comparison. (a) Time-averaged flow rates of coronary vessels were measured with PCMR in seven volunteers. Duplicate measures were acquired in 11 coronary arteries (6 RCA, 5 LM) and plotted against each other with correlation evaluated via Pearson's r. Then, the sums of corresponding LM and RCA flows were computed and plotted against the coronary sinus flows (b-c), and the means of the measures were plotted against the differences (d-e). Because duplicate measures were acquired, every combination of of the healthy volunteers (n = 6 for each) was evaluated for correlation with Pearson's r and for concordance with Lin's ρ_c, and the best (b, d) and worst (c, e) performing data combinations are presented here.

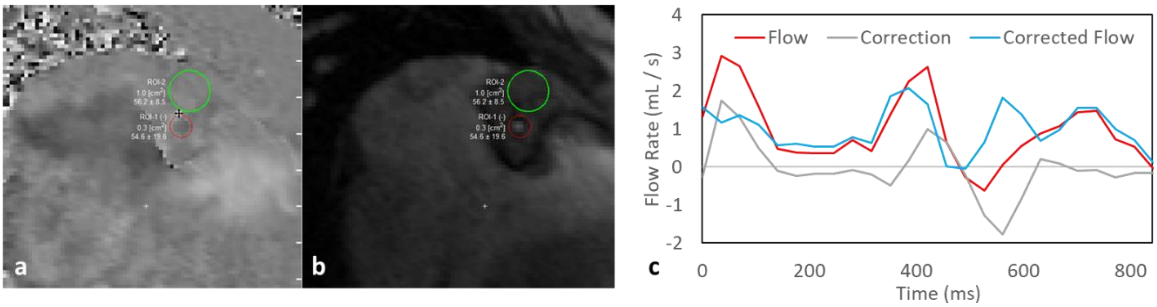

Figure 17: Representative LM arterial flow waveform and myocardial tissue motion correction.(a, b) Coupled PCMR phase and magnitude images with RCA outlined in red and adjacent myocardial tissue outlined in green. (c) Arterial flow waveform measured through segmentation of the RCA luminal contour in each temporal phase of the PCMR image data in red. The 'flow' measured through the myocardial segmentation was recorded and divided by the ROI area to obtain the average tissue velocity. This velocity was then multiplied by the arterial ROI area to obtain the amount of measured arterial flow which was caused by myocardial motion, plotted in gray. The negative of this waveform was subtracted from the measured arterial flow to obtain a corrected arterial flow waveform, plotted in blue.

Despite the presence of strong correlative relationships between the time-averaged values, an interesting phenomenon was observed from the time-resolved flow waveforms. Typically, coronary flow waveforms adhere to a primarily biphasic shape, wherein flow is slowed or even reversed during systole and is mostly positive during diastole. Consistently, however, a strong positive pulse was observed during systole with a negative pulse seen during diastole. When the myocardial tissue adjacent to the arteries was segmented, we observed non-zero velocities at many time points throughout the cardiac cycle. Subtraction of the myocardial velocity over the arterial cross-sectional area was able to mostly recover the expected arterial flow waveform. An example of this can be seen in Figure 17.

5.4 Discussion

The results indicate that 1) repeated PCMR measurements of coronary arterial flow produce consistent time-averaged flow rates, and 2) the sum of the time-averaged flow rates in the LM and RCA equal the time-averaged flow through the coronary sinus, thereby supporting both hypotheses. The consistency seen in the repeated flow measures indicates

a relative lack of random error, while the continuity between the arterial measurements and sinus measurements indicates a lack of systematic error due to the latter's aforementioned validation [47-49]. Overall, this supports the accuracy of time-averaged coronary arterial flow measurements obtained through PCMR.

The time-dependent velocity offset seen in the flow waveforms, however, does create several implications for evaluating coronary flow through PCMR. As described earlier, PCMR works through the application of a bipolar gradient which induces a phase-offset in each particle which is linearly proportionate to the component of the particle's velocity in the encoding direction. The phase offset recorded in each voxel is therefore the average of the phase offset of the particles contained within that voxel during the acquisition window. Ideally, if the 2D slice is placed such that the coronary vessel runs through-plane, then the velocity measured in each voxel would be representative of the blood-flow velocity at that location. However, as can be deduced from Figure 17, there is a secondary source of motion created by the heart itself. During cardiac contraction, the heart rotates which results in a through-plane motion of the myocardium and adjacent coronary vessel. Therefore, the velocity recorded through segmentation of the coronary lumen in PCMR images is actually the sum of the blood velocity relative to the vessel and the vessel's velocity relative to the fixed external reference.

The cardiac motion is periodic, meaning that within each cardiac cycle the expected net rotation of the heart should be zero. In the example waveform in Figure 17, the time-averaged flow rate of the waveform without correction was 0.96 mL / s, while the 'corrected' waveform showed an average rate of 0.99 mL / s. This indicates that for the time-averaged flow measurement, the cardiac motion should not contribute significantly to

the measured value. However, this only holds true so long as the ROI used to measure the coronary flow rate is kept constant throughout every temporal phase. If, for example, a large ROI is used during systole when ‘positive’ motion is recorded, while a small ROI is used during diastole when ‘negative’ motion is observed, then the net influence of the cardiac contraction will be non-zero. Furthermore, the through-plane velocity of the myocardial tissue will vary with radial distance from the rotational center of the heart. For smaller vessels such as the LM and RCA, this variation is not likely to be large enough to cause significant effects. However, for individuals with especially large coronary sinuses, this may indeed become a source of error.

This effect can introduce difficulty in coronary PCMR analysis. Though these arteries are typically not observed to dilate significantly, the visible cross-sectional area of the vessel can change considerably as it moves into and out of the slice. Proximal segments of the vessel will be larger than distal portions, and the vessel can shift into an oblique position at certain time-points which will create a larger, non-circular intersection with the viewing plane. Additional complications can arise in individuals with short LM arteries which quickly bifurcate into the LAD and LCX. If the viewing plane is placed such that some temporal phases capture both the LAD and LCX while others capture the LM by itself, then the combined areas of the ROIs must be carefully monitored such that a constant area is maintained. The coronary sinus presents even more difficulties due to its distensibility and relative proximity to the heart chambers, namely the left atrium. In many individuals, the cross-section of the coronary sinus, especially near the ostium to the right atrium, can drastically change in size and ellipticity over the cardiac cycle. Maintaining a constant ROI set to capture the maximum cross-section of the sinus can result in

measurement of flow velocities within the neighboring structures such as the left atrium. These effects can produce significant hurdles for full clinical implementation of coronary flow measurements.

Despite these hurdles, if a constant ROI is maintained which contains only the through-plane vessel of interest and minimal surrounding myocardial tissue, the contribution of the vessel velocity relative to a fixed reference should be negligible once the flow-rate is averaged across the cardiac cycle. To calculate vFFR, it was determined that only time-averaged coronary flow rates were necessary; therefore, these results appear to indicate that it is possible to acquire the flow information needed for vFFR calculation through PCMR, if an appropriate image analysis is undertaken.

However, the time-dependent velocity contribution of the myocardial motion does still affect the measured time-resolved waveform. Figure 17 represents a very rough approach to approximate the different velocity contributions, but it does not necessarily represent a comprehensive solution for fully separating the flow velocity from the vessel velocity. As it is, the velocity waveforms obtained through PCMR do not appear to accurately portray the true time-resolved coronary flow waveforms. Though this is not significant for vFFR calculation, this implies limitations for the use of PCMR in defining coronary boundary conditions for computational models wherein the time-dependent behavior is critical, such as in calculating wall shear stress. The maximum wall shear stress and oscillating shear index of vessels have both been linked with the nucleation and progression of atherosclerotic plaques, and study of this area is of particular interest. These results indicate that, without a more comprehensive solution to accurately resolve the

coronary flow velocity from the vessel velocity, PCMR cannot be used in these applications.

The time-averaged flow rates observed here do show general agreement with what has been published previously. In 2008, Johnson et al. published preliminary validation of coronary arterial flow measurements in which they reported RCA flow rates of 0.038 ± 0.019 L / min, LAD flow rates of 0.030 ± 0.017 L / min, and LCX flow rates of 0.028 ± 0.020 L / min [52]. The average coronary sinus flow rate recorded here—0.122 ± 0.048 L / min—also showed agreement with the 0.107 ± 0.019 L / min reported by Ganz et al. in 1971 [53].

This study does have several limitations. The cohort investigated were healthy volunteers, while the utilization of PCMR toward calculating vFFR will primarily be used in patients with CAD. Such patients may exhibit irregular breathing patterns or cardiac cycles which can complicate the prospective navigator- and ECG-gated scans used for planning and acquiring the PCMR flow data. The cohort would also benefit from a larger sample size for a more robust statistical analysis. The experiment was designed such that the effects of random and systematic error could be quantified; however, user error was not considered. Due to the necessary complexity of the flow analysis, reproducibility by different operators should also be quantifiably tested as well.

Lastly, invasive arterial flow measurements were not available for direct comparison with the PCMR-derived measurements. Though the coronary sinus flow measurements via PCMR have been previously validated against invasive flow measurements, this still creates a limitation for the overall results presented here. A future study comparing this methodology either in patients with clinically-indicated invasive flow

measurements or in an animal model would be necessary for full validation. Validation could also be provided through a phantom model, which would allow for direct ground-truth measurements for comparison, though such a model would of course need to be very complex to correctly simulate the physiologic processes involved.

5.5 Conclusion

The study suggests that the time-averaged coronary flow measurements obtained through PCMR and subsequent image analysis can be accurate. The time-dependent flow waveform was observed to be a superposition of the blood flow velocity and the vessel velocity as the heart moves through the imaging plane. If the ROI is maintained at a constant size, the time-averaged contribution from the vessel motion should be negligible, therefore allowing the flow measurement to be used for applications wherein time-dependent behavior is not necessary, such as in calculating vFFR.

CHAPTER 6. SELF-NAVIGATION CORONARY MRA

6.1 Introduction

To calculate vFFR through CFD, the patient-specific coronary anatomic geometry must be defined through whole-heart MRA. There are two primary sources of motion which must be considered for an acquisition of whole heart coronary anatomy to be successful. The first is the contractile motion of the heart itself. Because heart motion is typically periodic, this can be handled through ECG-triggering and gating acquisition to a quiescent interval of the cardiac cycle—usually mid-late diastole (Figure 18). If data are acquired at the same temporal location during each cardiac cycle, then it is expected that the heart will be in the same position, thereby reducing motion artifacts. The second source of motion is caused by respiration. Due to the amount of data necessary for a whole-heart angiogram, the subject cannot be expected to hold their breath over the required time frame. Rather, a free-breathing acquisition must be utilized. The most common technique to allow for free-breathing whole-heart MRA utilizes the previously described navigator beam. A navigator beam can be created by two secant planes oriented such that the line of intersection is in the SI direction of the subject. By placing this beam over the right

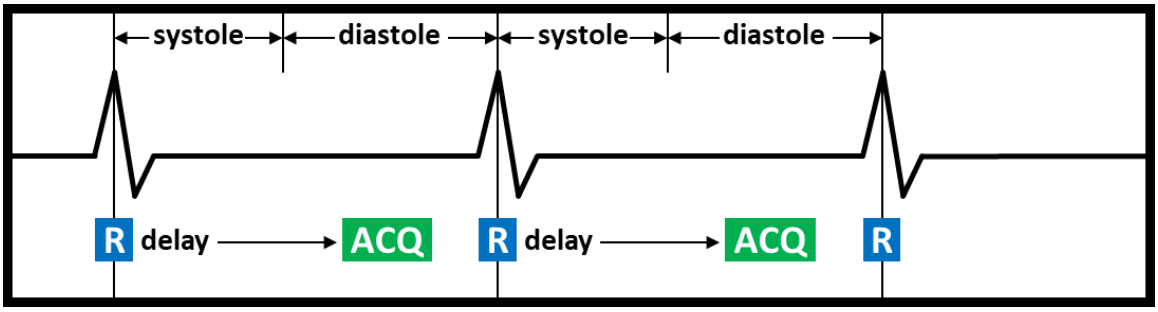

Figure 18: Prospective cardiac-gated acquisition window.

hemidiaphragm, a one-dimensional image can be acquired at the start of each cardiac cycle, and edge detection within a set positional range can be used to determine the respiratory motion state. If this respiratory state is contained within a pre-defined acceptance window, then data are acquired; otherwise, the scan acquisition is idle (Figure 4).

Both of these techniques represent what is known as *prospective navigator-gating*. Positional information about the heart is acquired in real-time and used to determine if data will be acquired *prior* to their acquisition. In individuals with consistent and predictable cardiac rhythms and respiratory cycles, such techniques can be very successful. Utilization of these techniques toward whole-heart angiography have previously allowed for full three-dimensional characterization of coronary arteries sufficient for vFFR calculation without significant motion artifacts [28]. In practice, however, such protocols can prove problematic.

Prospective navigator-gating requires the operator to identify the relative height of the diaphragm at end-inhalation. Tidal volumes, however, can frequently change, which can raise or lower the position of the diaphragm at end-inhalation. This can lead to very low acceptance rates which can cause unpredictably long scan times. Furthermore, the size of the coronary arteries necessitates that the acceptance window must be sufficiently small as well so that the effective motion-resolved resolution can accurately characterize the vessels, which can further extend scan times. To address these problems, respiratory self-navigation was first proposed as an alternative in 2005 [19]. The goal of this technique is to extract physiologic signals from the raw image data and use these signals to perform retrospective motion compensation. The specific approach utilized in this study is fully described by Piccini et al [21], however an abridged description is offered here.

During each cardiac cycle, data are acquired using a three-dimensional spiral phyllotaxis *k*-space trajectory which begins with a radial readout in the SI direction. Performing a one-dimensional Fourier transform on this SI readout provides a projection of the imaging volume onto the SI axis at the time of acquisition. Cross-correlation of the SI projection at each temporal location with a reference projection acquired at the beginning of the scan then allows for the absolute displacement of the heart in the SI direction to be approximated. Utilization of the Fourier shift theorem—which relates a translation in the image domain to a phase offset in the frequency domain—can then be used to perform motion correction on the data prior to regridding and image reconstruction (Figure 19). This technique, therefore, does not rely on any navigator gating to reduce motion artifacts, and has a 100% scan efficiency. This results in a very predictable scan time—usually between 4 and 7 minutes, depending on the patient's heart rate

This technique has been demonstrated on both healthy volunteers [21] and patients [22, 54], and these results support that it affords similar image quality to whole-heart MRA with navigator beams. Prior studies, however, have not specifically investigated whether this approach could provide images which allow for full three-dimensional segmentation and generation of coronary computational models. Furthermore, all prior studies investigating the image quality of this technique have been performed by the author of the

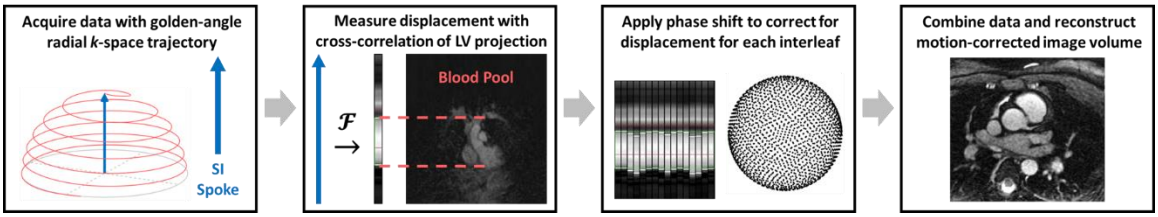

Figure 19: Overview of self-navigation MRA acquisition and reconstruction framework.

sequence, and it is not known if it is more widely applicable. *Therefore, this study sought to objectively assess whether the motion-corrected self-navigation whole-heart MRA can successfully and consistently provide images which can ultimately be used in the calculation of vFFR.*

6.2 Methods

Images were acquired in 33 patients (12 females; average age 44.4 ± 17.6 years) with congenital heart disease (**CHD**) undergoing clinically indicated cardiac MRI with IRB approval. All scans were performed on a 1.5 T MR scanner (MAGNETOM Avanto^{fit}, Siemens Healthcare) at Emory University Hospital in Atlanta, Georgia. Prior to data acquisition, a ventricular long-axis 2D cine was acquired to allow for the approximate diastatic window in the cardiac cycle to be determined. A low resolution localizer scan was run during free-breathing without cardiac gating over the desired FOV containing the heart. Automatic segmentation of the LV blood pool was then performed to determine which coil elements were most sensitive in detecting the LV, and this information was stored in the scanner PDS memory.

Images were then acquired using a 3D spiral phyllotaxis acquisition with a balanced steady-state free precession (**bSSFP**) readout over a cubic (220 mm) FOV with an isotropic voxel size of 1.15 mm and a flip angle of 115°. Image acquisition was gated to the predetermined diastatic temporal window using the patient's ECG. Following acquisition of each interleave, the SI readout lines collected by the two coil elements which were determined to be most sensitive to the LV blood pool were transformed to the image domain and compared against the reference projection acquired at the start of the scan to determine the respiratory positional offset of the data. The data in this interleave were then

phase-shifted to correct for this positional offset. Each interleave consisted of 32 radial segments, and a total of approximately 375 interleaves were acquired to provide ~12,000 radial lines of data. Prior to acquisition of each interleave, fat saturation and T2 magnetization preparatory pulses were applied, and a coronal saturation slab was placed over the anterior chest wall to better isolate motion signal from the LV blood pool.

The vessels of interest—LM, LCX, LAD, and RCA—were each qualitatively assessed for clarity on a scale of 0 to 4 by a single observer. A score of 0 indicated that the vessel was not visible at all; 1 indicated that only the presence of the vessel was observable; 2 indicated that the vessel trajectory could be followed for at least 30 mm; 3 indicated that some details regarding the vessel geometry could be observed; and 4 indicated that image quality was sufficient for the vessel to be fully segmented and used to generate a computational fluid model. For each patient, the average of these four scores was then calculated to provide an overall score.

6.3 Results

Overall, images acquired using the motion-corrected self-navigated whole-heart MRA did not appear to adequately provide quality sufficient for full three-dimensional characterization of the epicardial vessels. The average overall score for the patients was 1.7 ± 0.98 with per vessel scores of 2.14 ± 1.15 for LM, 1.15 ± 1.35 for LCX, 1.79 ± 1.08 for LAD, and 1.7 ± 1.02 for RCA.

During each scan, the inline display was used to monitor self-navigation. For the majority of patients, visual assessment of self-navigation did not meet expectations. For successful motion correction, the LV blood pool needs to be prominently visible against

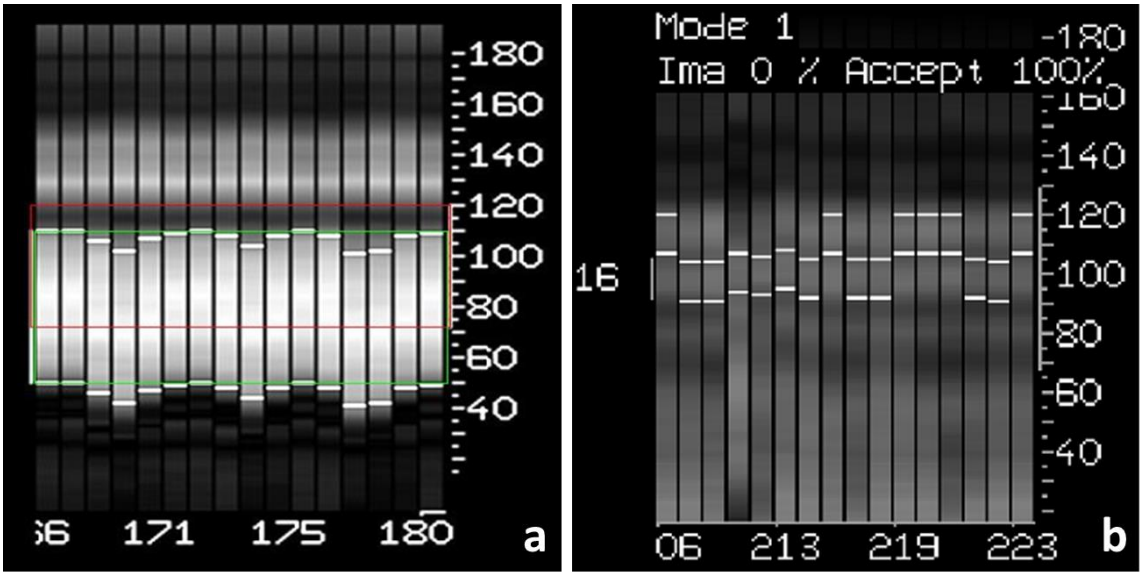

Figure 20: Representative view of self-navigation SI projections and LV blood pool detection. (a) What is expected to see from the SI projections with a bright LV blood pool projection and sharp edges delineating it from the adjacent tissue signal. (b) What was typically seen in these acquisitions. LV signal was not especially bright or easy to identify, and motion detection did not appear to represent an expected respiratory motion pattern.

the adjacent tissue (Figure 20a). This was not observed in majority of patients scanned (Figure 20b). If the navigator was seen to be obviously not working correctly and time permitted, the scan was stopped and the position of the FOV and saturation slab were adjusted to attempt to correct the motion detection. Frequently, however, these adjustments were either not possible to do within the time constraints of the clinical scan or no visible differences could be seen in the navigator following adjustments.

6.4 Discussion

The results indicate that this implementation of self-gating cannot consistently provide the image quality necessary for vFFR calculation through CFD. Considering that successful coronary characterization is possible through MRI—both Cartesian [28] and 3D radial [21]—it is not suspected that the imaging modality or readout trajectory are inherently flawed. Rather, it seems to be *the result of the respiratory motion detection and*

subsequent motion correction not performing as expected. More often than not, the LV blood pool projection could not be visibly seen in the SI projections, and the respiratory signal produced from the cross-correlation algorithm did not usually reflect a physiologically typical breathing pattern. Because tidal volumes can shift the diaphragm position by 10 or 20 mm during each breath, it is not surprising that inaccurate respiratory motion correction and subsequent artifacts can mostly or completely obstruct visibility of the coronary arteries.

There were several factors which may have contributed to the self-navigation not functioning as intended. The LV blood pool signal was not as strong as expected, which may have been due to the automatic LV segmentation and optimal coil selection not working successfully. It is possible that this was a result of the population recruited. Because these were congenital patients, many of them had anomalous anatomy, which may not have worked with the algorithm used to automatically detect and segment the LV blood pool. This, however, would appear to be an oversight as whole-heart MRA is very frequently employed in congenital patients to aid in planning functional scans where the anatomy may be atypical. Furthermore, comorbidity of CAD in patients with CHD is over four times greater than in patients without CHD ($p < 0.001$) [55].

Though the LV blood pool signal was not strongly visible on the navigator, visual inspection of the SI projections could usually identify a possible respiratory pattern (Figure 20b). It was therefore suspected that a more robust motion detection approach could instead be utilized on the acquired data, which could allow for successful motion compensation. The method used in this technique seems particularly sensitive to unexpected respiratory behavior. Each acquisition is considered in isolation of its temporal neighbors, which can

therefore result in discontinuous signals, an example of which can be seen in Figure 20b. Furthermore, successful cross-correlation of the LV requires that 1) the automatic segmentation of the ventricle is correctly performed, 2) the corresponding coil elements with the strongest signal contribution from the LV are identified, and 3) the LV signal is very bright against the neighboring tissue and shows a strong, consistent delineation. If any one of these does not perform as expected, then the resulting motion detection can become inaccurate. Lastly, this approach assumes that the respiratory motion is entirely within the SI direction, and that the heart moves rigidly without rotation. Even if both of these assumptions are invariably correct for all patients—which they frequently are not—this relies on the patient lying perfectly in alignment with the MR scanner.

The methods presented here are not without limitations. The heuristic evaluation of the vessel quality is qualitative, and arguably more substantial metrics could instead be used, such as vessel sharpness, signal-to-noise ratio, etc. Furthermore, comparison of these image sets against images acquired with alternate modalities—such as CT—could provide objective validation of the potential of these images in three-dimensional coronary segmentation. However, considering that the images underperformed as much as they did, it was determined that such metrics would not be necessary. It was visually apparent that these images could not be used for the intended application of calculating vFFR, and therefore attempting to quantitatively validate these images would not be worthwhile.

6.5 Conclusion

The images acquired through self-navigated, motion-compensated, whole-heart MRI were determined to be of suboptimal quality for full three-dimensional coronary characterization and segmentation. The most likely cause of this is suspected to be the

inability of the LV cross-correlation motion-detection algorithm, and subsequent motion-correction. The underlying principle—extracting physiologic signals from a 3D radial *k*-space trajectory—did not, however, appear to be inherently flawed. Therefore, utilization of this principle with a more robust motion-detection and compensation algorithm could likely improve upon this imaging technique.

CHAPTER 7. RESPIRATORY MOTION–RESOLVED 4D-GRASP CORONARY MRA

7.1 Introduction

In Chapter 5, it was concluded that using image self-navigation for absolute LV positional tracking during free-breathing and subsequent motion-correction could not consistently provide the image quality needed for reconstruction of the 3D coronary anatomy and vFFR calculation. Recent publications have utilized the underlying principle of self-gating toward motion-compensation in ways which should be more robust, particularly with regard to the suspected failures of the previously investigated technique—hereafter referred to simply as '**self-navigation MRA**'.

In 2015, Chandarana et al. first published preliminary feasibility of the novel reconstruction framework XD-GRASP [56], which was followed the next year with a more comprehensive explanation and investigation by Feng et al. [25]. The golden-angle radial sparse parallel (**GRASP**) acquisition technique utilizes a sparse radial sampling scheme with repeated *k*-space center samples which could then be combined with compressed sensing reconstruction to recover the desired image [57, 58]. Owing to the similarities in the *k*-space trajectories, combining GRASP with the principles of self-gating was a logical next step as it would theoretically afford improvement of both techniques.

The acquisition used in self-navigation MRI provides a fully sampled *k*-space volume from which the image volume can be reconstructed. If the physiologic signals contained within the *k*-space data are extracted and then used to bin the collected interleaves into discrete bins representing different respiratory phases, this results in

multiple artificially undersampled data sets which can be reconstructed using compressed sensing strategies. The application of this technique for respiratory motion–resolved whole-heart imaging was first described by Piccini et al. in 2016 [24] and is hereafter referred to as '**4D-GRASP MRA**'.

Binning the data rather than applying motion-correction affords several advantages to 4D-GRASP MRA over self-navigation MRA. For accurate motion-correction, the absolute three-dimensional positional displacement of the heart needs to be known for each data interleave. This requires an algorithm that can provide absolute displacement measurements—such as a cross-correlation of the LV blood pool SI projection against a reference projection. This was already discussed in Chapter 6 to be sensitive to erroneous input and unexpected behavior, and also relies on the assumptions that the respiratory motion of the heart is a strict translation in the SI direction and the patient is in perfect alignment with the scanner. Furthermore, aligning data such that the heart is always in the same position artificially creates motion artifacts in static tissue.

4D-GRASP MRA, however, has fewer constraints regarding the physiologic motion signal. Binning data acquired during similar respiratory phases automatically enforces that respiratory motion–induced artifacts are minimized within each bin, meaning that no motion-correction is needed prior to reconstruction. This removes the need to measure absolute positional displacement, allowing for more relative measures of the physiologic state such as independent component analysis (**ICA**) of the *k*-space center amplitude [24] or principal component analysis (**PCA**) of the SI projections [59] which are both potentially more robust in detecting motion than the LV cross-correlation approach. The 4D-GRASP approach does not rely on the assumption of strict translation in the SI

direction, either, only that 1) a sufficient component of the motion is in the SI direction to create a measurable signal and 2) the motion is periodic and does not exhibit significant hysteresis. Furthermore, 4D-GRASP MRA also produces a four-dimensional image: three spatial dimensions and one respiratory position dimension.

The 4D-GRASP technique had previously been applied in a small cohort of both patients and volunteers, and the vessel quality seen in the resulting images was evaluated to be greater than or equal to that seen in images from self-navigation MRA [24]. However, again, these images were not evaluated for their ability to provide a full three-dimensional characterization of the coronary arteries. Therefore, *the purpose of this study was to 1) more comprehensively compare the images acquired by 4D-GRASP MRA with those produced by self-navigation MRA and 2) evaluate the ability of 4D-GRASP MRA to sufficiently characterize three-dimensional coronary geometry for determination of the geometric boundary conditions needed for calculation of vFFR.*

7.2 Methods

Images were acquired in 23 patients (age = 39.8 ± 17.4, 10 female) with congenital heart disease who were undergoing a clinically indicated cardiovascular MRI at Emory University Hospital on a 1.5 T scanner (MAGNETOM Avanto^{fit}, Siemens Healthcare) with a multi-element array coil following IRB approval. Data were acquired using the same acquisition scheme, motion-correction, and reconstruction framework described in Chapter 6. Additionally, the raw *k*-space data—prior to motion-correction—were exported for offline reconstruction.

Offline reconstruction of the undersampled data sets was performed using a k-t sparse sensitivity-encoding (**SENSE**) algorithm [24, 26], exploiting sparsity in the respiratory dimension. All calculations were completed in MATLAB (MathWorks) to solve the optimization equation:

$$m = \arg\min_{m} \|F \cdot C \cdot m - d\|_2^2 + \lambda_c \|D_c \cdot m\|_1 + \lambda_r \|D_r \cdot m\|_1$$

where m is the five-dimensional image; F is the nonuniform fast Fourier transform operator; C is the coil sensitivity map; d is the *k*-space data; D_c and D_r are the first order difference operators along their respective dimensions; and λ_c and λ_r are the regularization weights for their respective dimensions. Prior to the offline reconstruction, the respiratory motion signal was extracted through the one-dimensional Fourier transform of the SI *k*-space lines and PCA of the temporal projection. Each interleaf was then binned into one of four respiratory positions as determined by the motion signal, such that each bin contained the same number of data sets [24]. A visualization of the overall methodology can be seen in Figure 21.

For each subject, the vessels of interest—LM, LCX, LAD, and RCA—were each qualitatively assessed for clarity on a scale of 0 to 4 by a single observer as described in the previous chapter. A score of 0 indicated a complete inability to see the vessel, while a

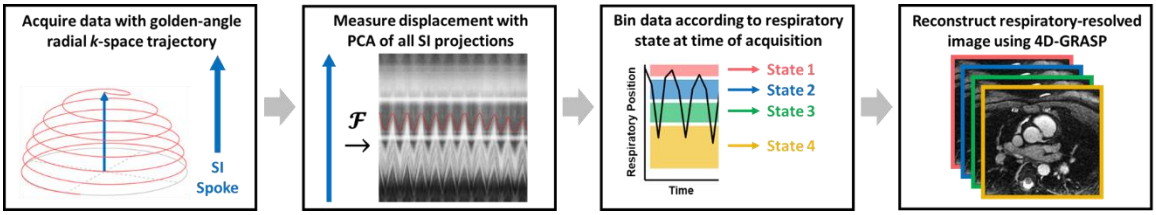

Figure 21: Visualization of the 4D-GRASP MRA data acquisition and reconstruction framework.

score of 4 indicated that the vessel had full three-dimensional characterization. This was performed for image sets reconstructed for each set of data both online (self-navigation MRA) and offline (4D-GRASP MRA).

The 4D-GRASP MRA vessel scores were evaluated with a one-sample, one-tail t-test against the hypothesis of a score of 4 both individually and when grouped together. Additionally, each vessel from the 4D-GRASP MRA was compared against the corresponding vessel from the self-navigation MRA using a paired, one-tail t-test to evaluate if the increase in score was significant, both individually for each vessel and when all vessels were grouped together.

7.3 Results

The overall image quality score for all vessels evaluated from the 4D-GRASP MRA images sets was 2.34 ± 1.07. Individual vessel scores were 3.00 ± 0.90 for LM, 1.70 ± 1.11

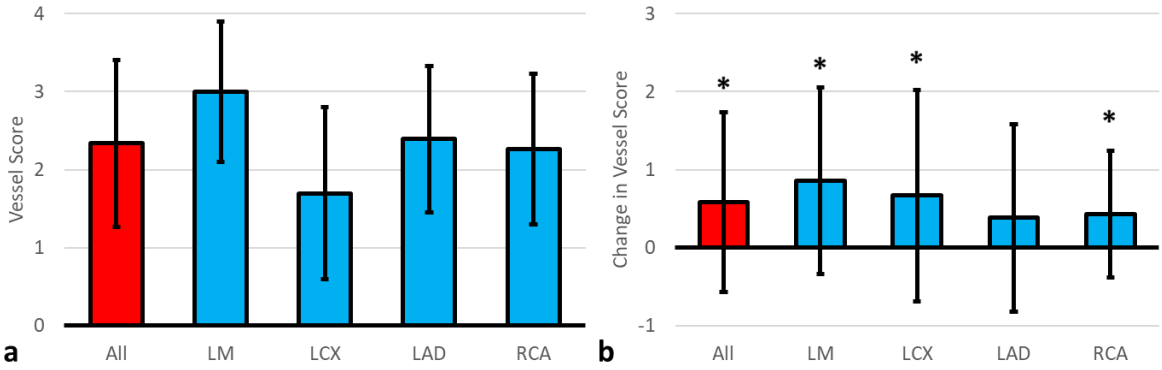

Figure 22: Vessel score results from images reconstructed using 4D-GRASP MRA. (a) All vessels were qualitatively evaluated on a scale from 0 to 4 for ability to characterize the three-dimensional coronary geometry.Significance was seen for each individual vessel (n = 23) and all vessels grouped together (n = 92) when compared against the null hypothesis of 4 with a one-sample, one-tail *t*-test ($p < 0.001$). (b) Vessel scores from the 4D-GRASP MRA images were then subtracted by the corresponding scores for the self-navigation MRA images, and these differences were plotted individually for each vessel (n = 23) and when grouped together (n = 92). Score differences were evaluated with a one-tail, one-sample *t*-test against the null hypotheses of 0 indicating no significant difference from self-navigation MRA to 4D-GRASP MRA. All groups showed significance ($p < 0.05$) except for LAD.

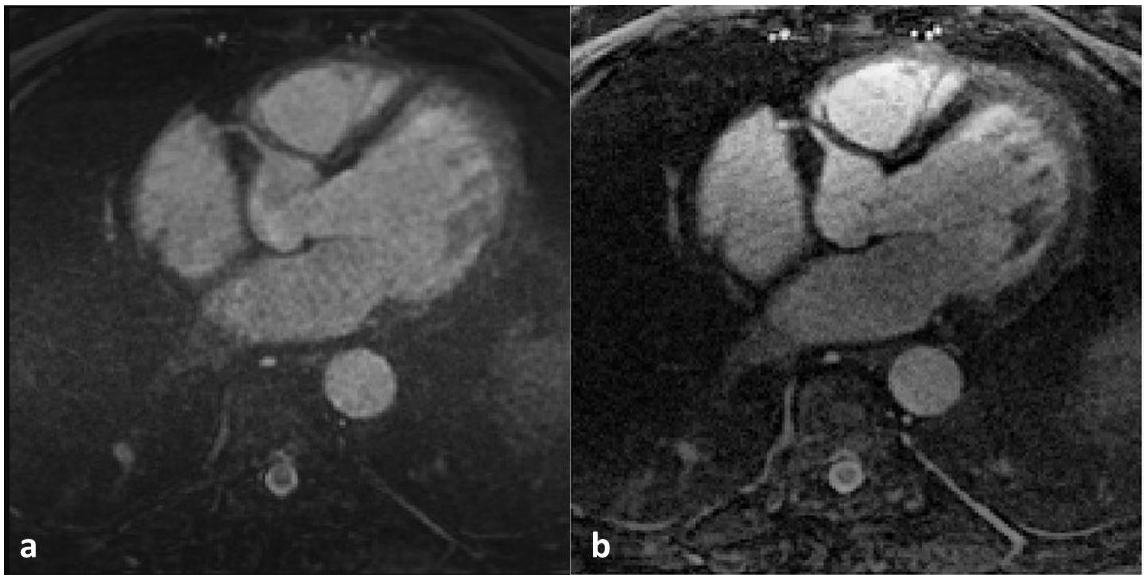

Figure 23: Representative comparison of two images acquired from the same data set using (a) the self-navigation MRA approach and (b) the 4D-GRASP reconstruction approach.

for LCX, 2.39 ± 0.94 for LAD, and 2.26 ± 0.96 for RCA (Figure 22a). All vessel groups were seen to be significantly below 4. In total, of the 92 vessels assessed, only 14 of the 4D-GRASP MRA group achieved a score of 4, though this was higher than the self-navigation MRA group which only had four vessels achieve a score of 4. On average, 4D-GRASP MRA was seen to give higher scores for all vessels combined as well as for the LM, LCX, and RCA (Figure 22b) (Figure 23).

The SI projections and resultant motion tracking was observed visually to be much more successful with the PCA approach used in 4D-GRASP MRA than the cross-correlation approach used in self-navigation MRA. An example comparison can be seen in Figure 24. Both motion-tracking images come from the same data set, and though some respiratory motion can be seen in the projections in Figure 24a, the cross-correlation–based approach does not appear to successfully track this. Conversely, a much more compelling respiratory signal can be seen from the PCA in Figure 24b.

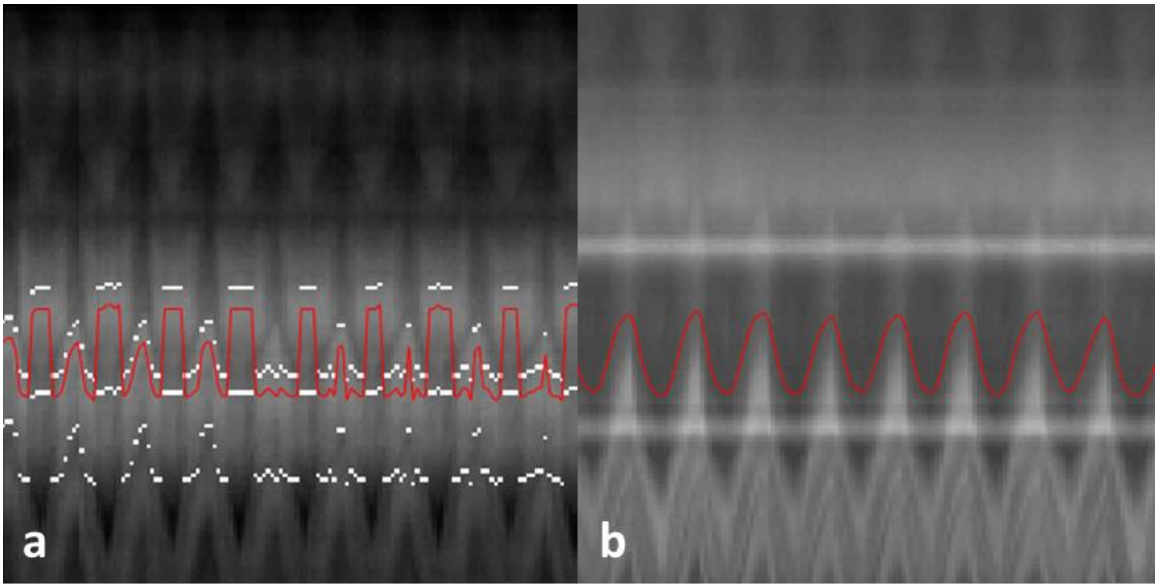

Figure 24: Representative comparison of (a) LV cross-correlation motion tracking and (b) PCA motion tracking. Both were acquired from the same data set, extracted respiratory position overlaid in red.

7.4 Discussion

Overall, 4D-GRASP MRA showed improvement over self-navigation MRA in a direct, paired comparison. Due to the improvement seen in the respiratory motion tracking, this is likely a large contributing factor. PCA was seen to be generally more robust for handling data were the LV projection was not clearly identifiable on the navigator images and therefore would not be easily detected through cross-correlation with a reference image. The ability to correctly track the respiratory motion is integral for both reconstruction approaches to work, and it therefore yielded an improvement in the vessel quality.

Other factors may have also contributed to the improved quality. Beyond the motion-tracking methods, 4D-GRASP MRA also differs from self-navigation MRA in that it bins the data rather than attempting to correct the motion. This makes 4D-GRASP MRA

less susceptible to artificial motion induction in the static tissues of the image. The 4D-GRASP motion-compensation is not reliant on absolute displacement measurements, nor does it rely on an assumption of a purely superior-inferior respiratory motion.

The measured improvement of 4D-GRASP MRA over self-navigation MRA agrees with a previously published comparison primarily in healthy volunteers and was therefore expected [24]. Though an overall improvement in image quality was observed, the images were still not deemed to be acceptable for full three-dimensional coronary characterization. More individual vessels were seen to be of sufficient quality, but the population as a whole did not have the image quality needed. There are several factors which may have contributed to this.

First, although the respiratory signal recovered through PCA was visually observed to more accurately represent the SI projections, it was not quantitatively validated against the true respiratory position, as this would be difficult or impossible to do. Because the images do show a relative lack of respiratory motion artifacts, it can be assumed that some degree of compensation was achieved, though of course there may be errors, such as blurring, which are difficult to detect. Furthermore, the self-navigated approach does assume that the respiratory position remains constant throughout the duration of each data acquisition, and bins the entire interleaf based on the physiologic state exhibited when only the first line of *k*-space was acquired. Each data acquisition occurred over approximately 150 ms, which is relatively short compared to the period of a breathing cycle, but a significant amount of motion may occur during this time. Attempting to correct for this, however, would require an interpolation of the respiratory position between each acquisition to predict where each interleaf should be placed, but doing so can be

fundamentally difficult due to the unpredictable and variable nature of the respiratory cycle.

The k-t SENSE algorithm used to reconstruct the undersampled data takes advantage of compressed sensing strategies to recover information in the reconstructed image, but the data are still inherently undersampled. Acquisition of more interleaves to reduce the reliance on k-t SENSE may help improve image quality, however this would result in increased acquisition time.

Another likely source of error can be attributed to the prospective cardiac-gating. The acquisition time was prospectively set to occur during mid-late diastole; however, this did not always occur consistently. Many patients' heartrates were observed to change over the course of the 5-7 minute scan, which would often result in the acquisition occurring earlier in the cycle at end-systole or early-diastole, or it may occur too late in the cycle and be interrupted by the R-peak detected at the beginning of the next cycle. Furthermore, many patients exhibited end-diastolic stasis windows which were significantly shorter than the 150 ms needed for the acquisition. Correcting for this without reducing the total number of samples acquired would have required a much longer acquisition, however this might be preferable for these patients. In a small subset of patients, the acquisition itself would induce an artifact in the recorded ECG which would be detected as an R-peak. When this occurred, acquisition would be interrupted consistently during each heart-beat. Usually, however, when this was observed, the acquisition would be aborted early and attempted again after repositioning the FOV, but this did not always fix the problem.

7.5 Conclusion

Images acquired through 4D-GRASP MRA were seen to offer overall improvement on the vessel quality as compared with self-navigation MRA. This can likely be attributed to the improved motion tracking afforded by PCA, though other factors may also be involved. Image quality afforded by 4D-GRASP MRA was not, however, seen to be sufficient for full three-dimensional vessel characterization, and therefore cannot be used for consistent vFFR calculation. It is suspected that cardiac motion may still be a significant factor in degrading the image quality, specifically with regards to the acquisition window size and the prospective-gating approach.

CHAPTER 8. RESPIRATORY AND CARDIAC MOTION–RESOLVED 5D-GRASP CORONARY MRA

8.1 Introduction

Although 4D-GRASP MRA could not consistently acquire images of sufficient quality for vFFR calculation, there was a definite improvement over self-navigation MRA presumably due to the increased robustness of the methodology used to compensate for respiratory motion. PCA of the SI projections to calculate a relative measure of respiratory motion proved to more reliable than attempting to determine the three-dimensional displacement of the heart through cross-correlation of the LV blood pool. Binning the data according to respiratory motion state inherently minimizes motion artifacts within each bin, and compressed sensing reconstruction was capable of recovering information from undersampled data.

One of the major advantages offered by 4D-GRASP MRA is shared with self-navigation MRA: retrospective navigation to compensate for respiratory motion. Prospectively gating image acquisition according to respiratory position can be sensitive to changes in the respiratory pattern. For the acquisition to be successful, the subject's breathing needs to remain constant throughout the duration of the acquisition. Conversely, retrospective navigation can much more easily adapt to changes in the respiratory pattern, allowing for more consistently reliable acquisition.

To further improve upon 4D-GRASP MRA, this same rationale can be extended and applied to the other primary source of motion during a whole-heart MRA—cardiac motion—to produce respiratory and cardiac motion–resolved images, hereafter referred to

as '**5D-GRASP MRA**'. A five-dimensional whole-heart MRA utilizing the XD-GRASP reconstruction framework was first described by Feng et al. in 2018 [26], however the methodology used in this study more closely resembles the technique described by Sopra et al. in 2019 [27]. For 5D-GRASP MRA, a golden angle readout initiating from an SI radial line is used to perform a continuous, free-running data acquisition without prospective respiratory gating or ECG triggering. Performing PCA on the SI projections will therefore yield a physiologic signal which is a superposition of both respiratory motion and cardiac motion. By separating these signals, the specific cardiac temporal phase and respiratory position exhibited by the subject at the time of each interleaf acquisition can be determined, and binning can be performed accordingly. The result is a whole-heart image volume which is resolved across both the cardiac and respiratory cycles—i.e., a five-dimensional image (Figure 25).

The benefits afforded to the implementation of retrospective navigator-gating are also true for retrospective cardiac-gating. Rather than prescribing the acquisition window to occur at a fixed time delay following detection of an R-peak, temporal phases within the cardiac cycle are determined by relative temporal location. This allows the algorithm to adapt to changes in the subject's heart rate in the same way that 4D-GRASP MRA could adapt to changing respiratory behaviors. The result, theoretically, should be a more reliable

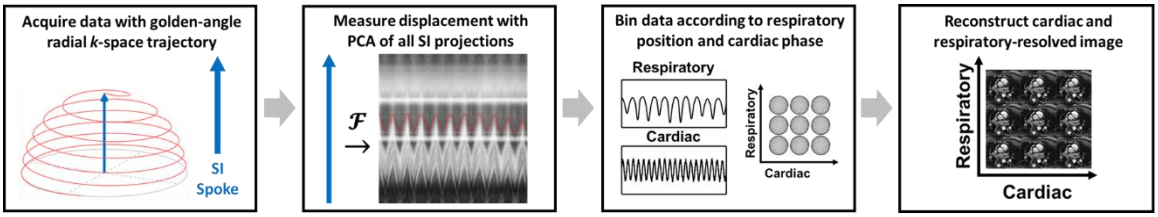

Figure 25: Visualization of acquisition and reconstruction framework for 5D-GRASP MRA.

whole-heart MRA. In practice, this approach has shown preliminary success, though only in healthy volunteers [26, 27].

Transitioning from a prospective cardiac-gated acquisition to a free-running, ungated acquisition does, however, introduce one major drawback. The acquisition scheme used in both self-navigation MRA and 4D-GRASP MRA employs a series of preparatory pulses prior to data collection. First, a T_2 prep module consisting of nonselective radiofrequency (**RF**) pulses saturates tissues with short T_2 values, such as the myocardium, thereby accentuating signal from blood. Next, a fat saturation pulse suppresses the epicardial fat which surrounds the coronary arteries. Lastly, a saturation slab on the anterior

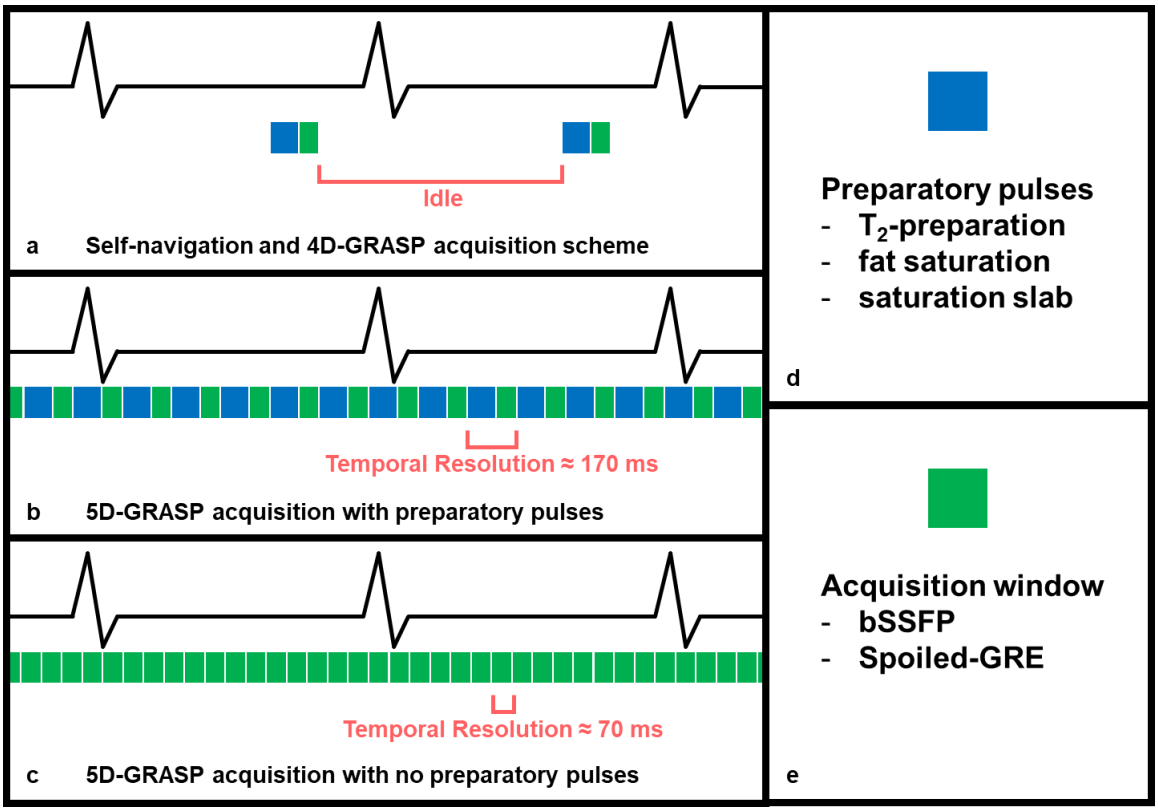

Figure 26: Comparison of acquisition schemes. (a) In a prospectively cardiac-gated sequence, acquisition (green) is limited to mid-late diastole and is preceded by a series of preparatory pulses (blue). Otherwise, the scan is idle. (b) In a continuous acquisition, the preparatory pulses significantly worsen the temporal resolution, when compared with (c) a continuous acquisition with no preparation.

chest wall suppresses chest motion which could otherwise obstruct LV blood pool motion-detection and produce fold-over artifacts which would manifest as radial streaking. The total time necessary for these preparatory pulses—approximately 100 to 150 ms—is usually negligible when acquisition is limited to only once per cardiac cycle (Figure 26a). When data acquisition is occurring continuously to fully resolve images across the cardiac cycle, however, these preparatory pulses can reduce effective the temporal resolution of acquisition by more than half (Figure 26b-c). Furthermore, application of these preparatory pulses can disrupt the steady-state free precession (**SSFP**) used to maintain a transverse coherence, which can significantly deteriorate the image quality. To address this problem, we considered three different solutions.

1. The first was the utilization of the bSSFP sequence described by Sopra et al. [27] without the T_2-prep or the saturation slab. The signal intensity for a bSSFP sequence is directly related to the ratio of T_2 / T_1 which naturally produces contrast between blood and myocardium [60], and fat-suppression was used to reduce the epicardial fat signal. The drawback to this method is that the lack of anterior chest wall suppression could affect motion-detection and produce streaking artifacts, and the blood-myocardium contrast would be reduced without the T_2-prep pulse.
2. The second solution used a spoiled–gradient echo (**GRE**) sequence with gadolinium-based contrast agent. A spoiled-GRE sequence is designed to disrupt T_2 coherences, thereby resulting in a T_1-weighted image. Because gadolinium is strongly paramagnetic, it reduces blood T_1 following injection. By shortening the T_1 in blood and disrupting T_2 coherences, the resulting image should preferentially provide strong vascular signal. A drawback to the GRE plus gadolinium methodology is that

gadolinium very quickly begins to perfuse into the surrounding myocardial tissue, thereby reducing the contrast afforded between the myocardium and blood as a function of time. The time-scale over which this occurs is on the order of minutes, meaning the window during which the gadolinium can be effectively used is limited. Due to the number of radial lines needed for a five-dimensional image reconstruction, the free-running acquisition lasts for approximately 10 minutes. Even if contrast is still afforded by the gadolinium throughout this acquisition, the relative signal intensities of the blood and myocardium would not remain constant. Therefore, the outcome of this approach could not be fully anticipated.

3. The third solution considered was use the of ferumoxytol, an MRI contrast agent, combined with a spoiled-GRE acquisition. Ferumoxytol is a superparamagnetic iron oxide–based drug which has been primarily used to treat anemia but has shown great potential for off-label diagnostic use as a T_1 shortening contrast agent for cardiovascular MRA. At a concentration of 4 mg Fe / kg body weight, the T_1 of blood has been shown to decrease from 1990 ± 573 ms to 80 ± 42 ms, with an *in vivo* R_1 relaxivity of 12 mM^{-1} s^{-1} at 1.5 T [61]. By comparison, the R_1 relaxivities of gadolinium-based agents are usually in the range of 4 to 5 mM^{-1} s^{-1} at 1.5 T [62]. With a spoiled-GRE T_1-weighted acquisition, this very preferentially increases blood signal intensity in the images. Furthermore, the particle size of ferumoxytol is substantially larger, preventing it from leaving the vasculature. Without redistribution into the extravascular space, the concentration differential between blood and myocardium is maintained, and plasma elimination half-life in humans is

approximately 10 to 14 hours [61]. Therefore, the properties of ferumoxytol make it particularly well-suited for use in 5D-GRASP MRA.

The purpose of this study was to investigate the use of ferumoxytol-based contrast-enhancement in 5D-GRASP MRA to determine if it could provide full three-dimensional characterization of the coronary vasculature. Though its success was expected, the other two 5D-GRASP MRA approaches described were also pursued to potentially identify more clinically feasible alternatives to ferumoxytol. Testing of the non-contrast–enhanced SSFP acquisition and the gadolinium-enhanced spoiled-GRE acquisition was performed in two separate cohorts of patients with CHD, while the ferumoxytol-enhanced protocol was tested in a cohort of pigs.

8.2 Methods

8.2.1 Non-Contrast, bSSFP 1.5 T Free-Running Acquisition

Imaging was performed in nine patients (age = 46.4 ± 17.3 years, five female) with congenital heart disease who had been clinically indicated for cardiovascular MRI at Emory University Hospital on a 1.5 T scanner (MAGNETOM Avanto^{fit}, Siemens Healthcare) with a multi-element array coil with IRB approval. Data were acquired using a previously reported free-running, three-dimensional radial bSSFP sequence [23]. The sequence employed a continuous, ungated acquisition (Figure 26c) over a 192 x 192 x 192 mm^3 FOV with 192 samples per readout, giving an isotropic spatial resolution of 1 mm^3. Excitation utilized a non-slice-selective RF pulse with a 71° flip angle which was preceded by a chemically shift–selective fat saturation pulse and 10 linearly increasing ramp-up RF pulses. A total of 107,932 radial readouts were acquired with 22 segments per interleaf over a total, constant scan time of 8 minutes and 11 seconds. Acquisition of each interleaf

occurred over 83 ms. Following the scan, the anonymized raw data were exported offline for reconstruction.

8.2.2 Gadolinium-Enhanced, Spoiled-GRE 1.5 T Free-Running Acquisition

Imaging was performed in 13 additional patients (age = 49.15 ± 16, nine female) with congenital heart disease who had been clinically indicated for cardiovascular MRI at Emory University Hospital on a 1.5 T scanner (MAGNETOM Avanto^{fit}, Siemens Healthcare) with IRB approval. Data were acquired using a continuous, free-running, golden-angle radial spoiled-GRE sequence over a 192 x 192 x 192 mm^3 FOV with 192 samples per readout, giving an isotropic spatial resolution of 1 mm^3. Excitation used a 15° flip angle and was preceded by a shift-selective fat saturation pulse and 10 linearly increasing ramp-up pulses. A total of 107,932 radial readouts were acquired with 22 segments per interleaf over a total, constant scan time of 7 minutes and 45 seconds. Acquisition of each interleaf occurred over 79 ms. Immediately prior to data acquisition, 0.01 mmol / kg of gadoteridol was injected into each patient. Following the scan, the anonymized data were exported offline for reconstruction.

8.2.3 Ferumoxytol-Enhanced, Spoiled-GRE 3 T Free-Running Acquisition

Imaging was performed in a cohort of three hypercholesterolemic Wisconsin miniature pigs at the Emory School of Medicine Center for Systems Imaging Core on a 3 T scanner (MAGNETOM Prisma^{fit}, Siemens Healthcare) under an IACUC approved protocol in collaboration with the Emory University School of Medicine Heart Research and Innovation Laboratory. Prior to scanning, each pig was anesthetized, intubated, and placed on respiration. Ferumoxytol at a concentration of 4 Fe mg / kg was dissolved into 100 mL of saline and infused into the auricular artery over 15 to 20 minutes, followed by

a saline flush. The pigs were then placed in the scanner head-first and supine. Data were acquired with a continuous, ungated, golden-angle radial spoiled-GRE sequence over a 192 x 192 x 192 mm^3 FOV with 192 samples per readout, giving an isotropic spatial resolution of 1 mm^3. Excitation used a 15° flip angle and was preceded by 10 linearly increasing ramp-up pulses. A total of 129,000 radial lines were acquired with 22 segments per interleaf. Acquisition of each interleaf occurred over 66 ms, and the time required to sample all 5983 interleaves was 6 minutes and 29 seconds. Following acquisition, the raw data were exported offline for reconstruction.

8.2.4 Physiologic Signal Extraction and Binning

For all data sets, cardiac and respiratory motion signals were extracted from the raw data using a previously reported methodology via MATLAB (MathWorks) [27]. For a given interleaf, the first radial line oriented in the SI direction for each coil was one-dimensionally fast Fourier transformed to give a projection of the volume at the time of acquisition. Projections from each coil were stacked, and then concatenated temporally. Subsequent PCA of the resulting temporally-resolved SI projection matrix produced a physiological motion signal which spanned the duration of the sequence acquisition. The major components contained within this signal represented both cardiac and respiratory motion. To separate these two signal components, the power spectral density (**PSD**) of the first 10 principal components was computed and analyzed to determine the frequency center of mass of the cardiac motion, starting with frequencies between 0.5 Hz and 2.0 Hz. A similar methodology was then used to identify the respiratory signal beginning with frequencies between 0.1 Hz and 0.7 Hz. Once the signals were successfully identified and

separated, data were binned into four respiratory states and a variable number of cardiac phases determined such that each phase represented a 50 ms window (Figure 25).

8.2.5 Image Reconstruction

Image reconstruction of the highly undersampled data sets was then performed using the SENSE algorithm [24, 26] exploiting sparsity in both the cardiac and respiratory dimensions. All calculations were performed in MATLAB (MathWorks) on a server equipped with two 24-core CPUs, 384 GB RAM, and an 11-GB NVIDIA GPU. Reconstruction was performed to solve the optimization equation:

$$m = \arg\min_{m} \|F \cdot C \cdot m - d\|_2^2 + \lambda_c \|D_c \cdot m\|_1 + \lambda_r \|D_r \cdot m\|_1$$

where m is the five-dimensional image; F is the nonuniform fast Fourier transform operator; C is the coil sensitivity map; d is the *k*-space data; D_c and D_r are the first order difference operators along their respective dimensions; and λ_c and λ_r are the regularization weights for their respective dimensions.

8.2.6 Regularization Parameter Optimization

The optimization equation used to iteratively calculate the image volume attempts to find a solution which minimizes the summation of three separate components. The first of these components represents the error associated with the transform of the image and the recorded data. The other two components each represent the differences between adjacent motion states along the cardiac and respiratory dimensions. These components, therefore, attempt to enforce a continuity along each of these dimensions which must then be balanced against the error minimization. The values prescribed to each of the two regularization parameters control the relative weight of these three components, and

determination of the optimal values for these parameters is critical for success of the image calculation.

The options currently available to predictively optimize these parameters are limited. Rather, they need to be optimized experimentally. Furthermore, the relative

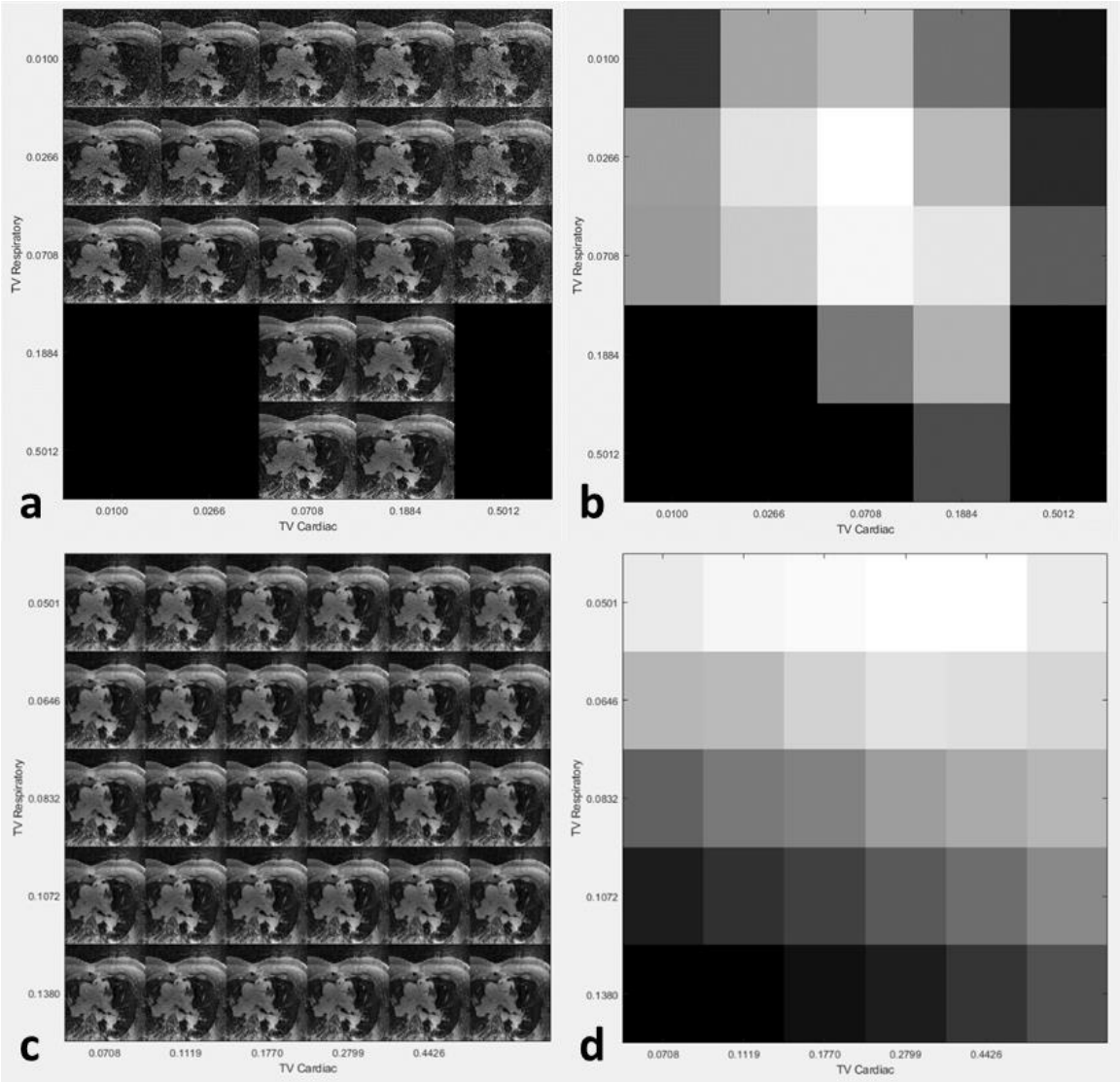

Figure 27: Representative display for regularization parameter optimization. (a) A coarse array of regularization parameters were used to reconstruct images from the raw data. (b) The SNR of the blood was then sampled for each of these reconstructions and used to determine a local maximum within the array. (c) A more granularized array was then selected and used for reconstruction, (d) followed by further refinement of the parameter selection through SNR measurement.

weights can vary substantially for different cohort demographics and acquisition schemes. Therefore, for each of the three acquisition schemes utilized in this study, a single data set was used to perform an experimental optimization of these two parameters. First, a coarse array of values was set, and images were reconstructed for each value combination (Figure 27a). To quantitatively compare each parameter combination, the signal-to-noise (**SNR**) of the aortic blood pool was calculated. For this, a single transverse slice was chosen which contained the aortic trunk near the coronary ostia. The aortic lumen was manually traced, and the mean signal intensity was calculated, then divided by the standard deviation of the signal to give an estimation of the blood pool SNR. The voxels used for this calculation were stored in memory and used to perform the same SNR calculation for each parameter combination, and the region of the array with the local maximum was identified (Figure 27b) and used to select a more granular array of values with which to repeat the experiment (Figure 27c-d). This was repeated until an optimal parameter set was identified, which was then used to reconstruct all other images within that image group.

8.2.7 Image Quality Evaluation

All reconstructed image sets were evaluated heuristically for all three techniques by scoring the epicardial vessels—LM, LAD, LCX, and RCA—on a scale from 0 to 4 as described in the previous chapter, again with 0 indicating a complete inability to detect the vessel and 4 indicating excellent three-dimensional characterization sufficient for use in a computational fluid model.

8.2.8 Ejection Fraction

For further validation of the cardiac binning of the data, the ejection fraction (**EF**) for a subset of patients was calculated using 1) the short-axis LV cine stack acquired as part of the routine clinical scan and 2) an MPR of the five-dimensional image set used to create a short-axis LV cine stack. For each cine stack, clinical or reformatted, Simpson's method of discs was used to estimate the end-diastolic volume (**EDV**) and end-systolic volume (**ESV**) which were then used to compute the EF. Comparison between values was performed through calculation of the linear correlation coefficient. MPR of the cardiac-resolved image volume (Figure 28) and generation of the simulated cine stack (Figure 29)

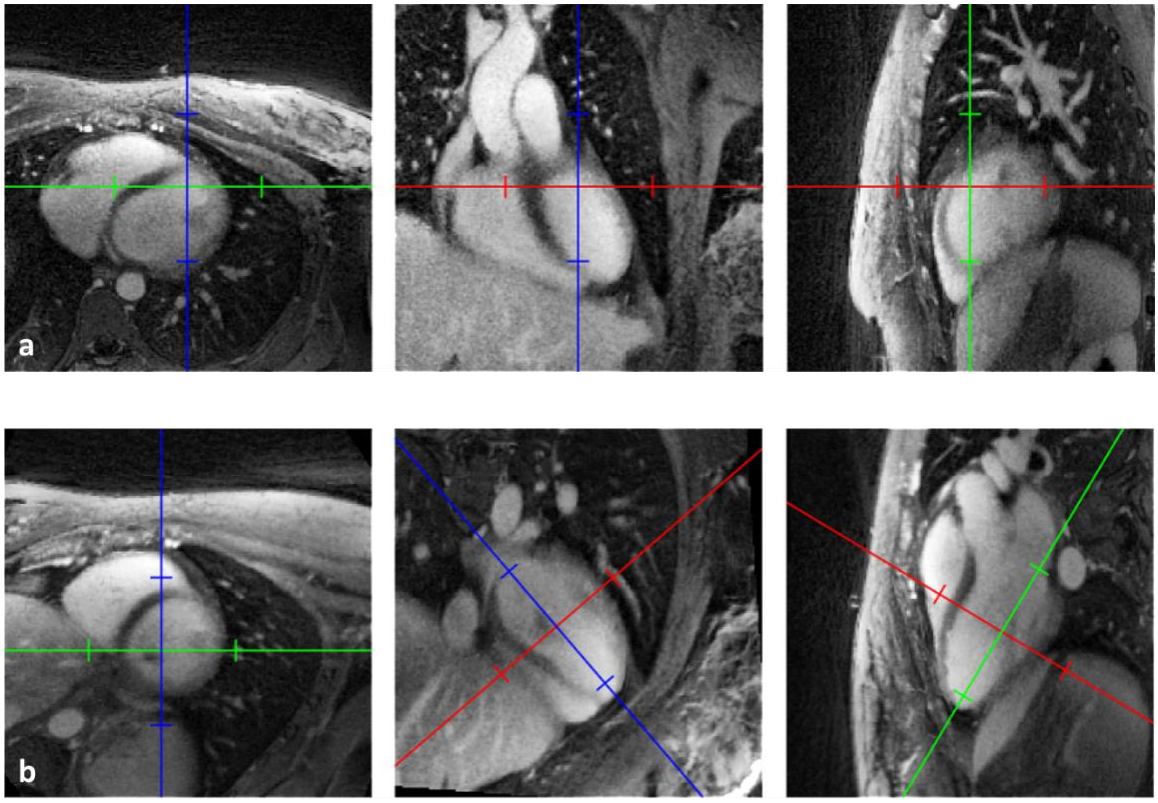

Figure 28: Example MPR of cardiac-resolved image volume. (a) Original configuration of orthogonal slices in the axial, coronal, and sagittal views, respectively. (b) Reformatted volume showing short-axis view of the LV in the first image and long-axis views in the others.

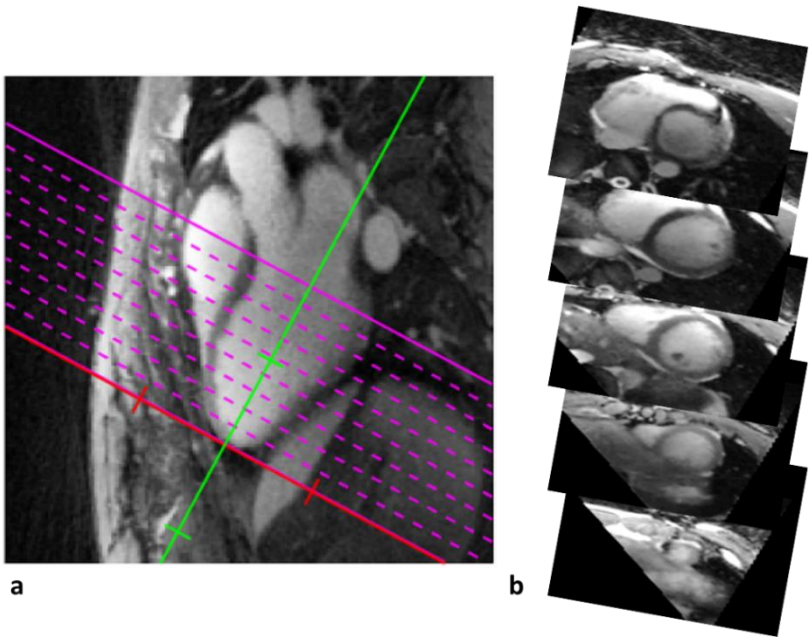

Figure 29: Example of short-axis cine stack generation from 5D-GRASP MPR. (a) Long-axis view of the LV with projection of short-axis cine stack placement. (b) Stack of short-axis views generated.

was performed via MATLAB (MathWorks), and calculation of EDV and ESV was performed via Segment version 2.0. For each case, the mean signal of the LV blood pool was calculated at the short-axis view located mid-ventricle and was divided by the mean signal of the septal myocardium in the same view. This was done through manual segmentation. Paired comparison was performed between 5D MPR and 2D cines.

8.2.9 Limited Dimension Reconstruction

In two of the ferumoxytol-enhanced five-dimensional acquisitions, a series of additional reconstructions were performed utilizing a limited cardiac dimension. Using previously reconstructed cardiac-resolved image sets, the cardiac phase visually determined to occur during diastasis was selected. Then, rather than use the entire array of cardiac phases for the reconstruction, only the end-diastolic stasis phase and a limited number of adjacent phases were used (Figure 30). For each raw data set, this limited

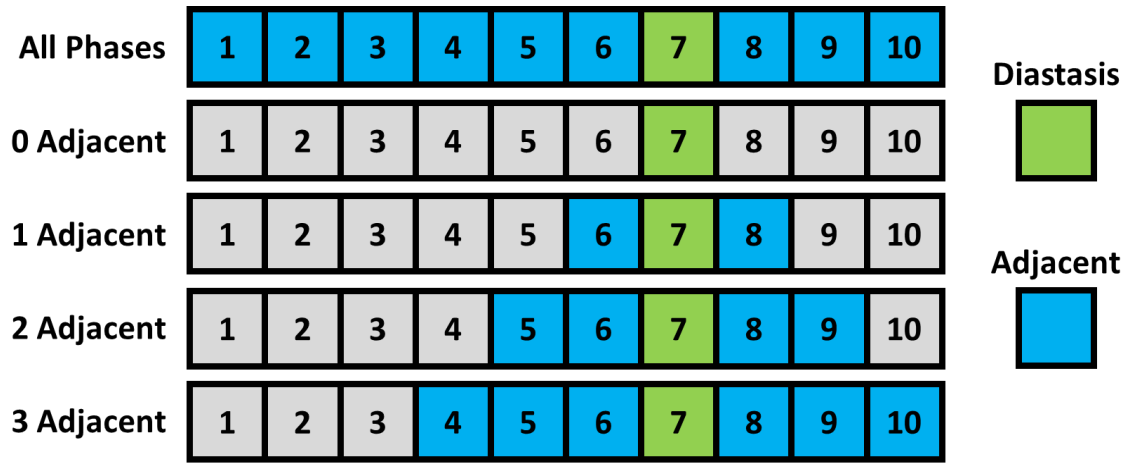

Figure 30: Visual representation of limited dimension reconstruction. If a data set was binned into 10 cardiac phases, then in the normal reconstruction all 10 phases would be used. In the limited dimension reconstruction, the diastasis phase—7 in this case—was identified, and a limited number of adjacent phases were used in the reconstruction.

dimension reconstruction was repeated with a variable number of adjacent phases ranging from zero to four. For each limited reconstruction, 1000 voxels were selected at random from the diastasis volume at end-inspiration and compared against the same voxels in the corresponding volume from the fully-reconstructed image set through calculation of Pearson's correlation coefficient and structural similarity (**SSIM**) index.

8.3 Results

8.3.1 Reconstruction

Reconstruction for each five-dimensional image required a significant amount of computational power. Memory usage varied for each data set, but it was observed to use approximately 100 to 200 GB at any given time. The time needed for each reconstruction also varied depending on the specific data asset and the combination of regularization parameters used but was observed to take from 12 to 30 hours.

8.3.2 Heuristic Evaluation

The images acquired from the three separate acquisition groups were evaluated heuristically by qualitatively assessing the quality of each epicardial vessel—LM, LAD, LCX, and RCA—on a scale of 0 to 4. The average score for each vessel was observed to be consistently higher with the gadolinium-enhanced, spoiled-GRE acquisitions (1.15 ± 1.04) than for the non-contrast–enhanced, bSSFP acquisition (0.78 ± 0.76), however differences were not found to be significant between groups when compared together or on a per-vessel basis (Figure 32). Significant differences were seen when comparing either the vessels individually or the acquisition group as a whole against the null hypothesis of $\mu_0 = 4$. Additionally, none of the 88 vessels from either group were evaluated to be of sufficient quality for use in computational fluid modeling. The ferumoxytol-enhanced, spoiled-GRE acquisition, however, was observed to perform substantially better than the other two groups (Figure 31) (Figure 33).

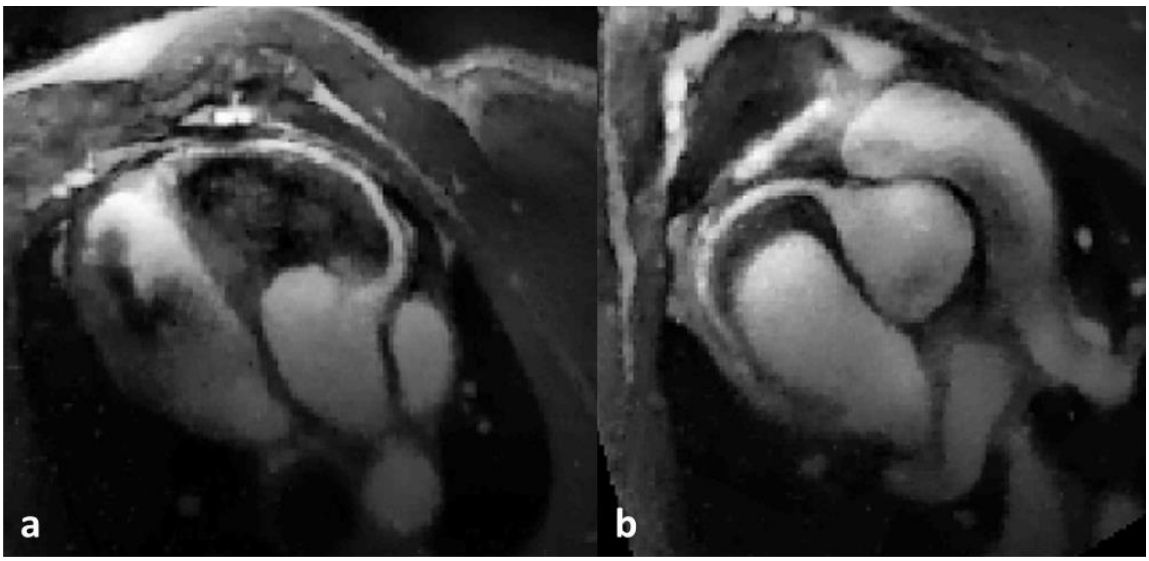

Figure 31: Typical results are shown. (a) Reformatted image volume showin the LM and LAD. (b) Reformatted images showing the RCA.

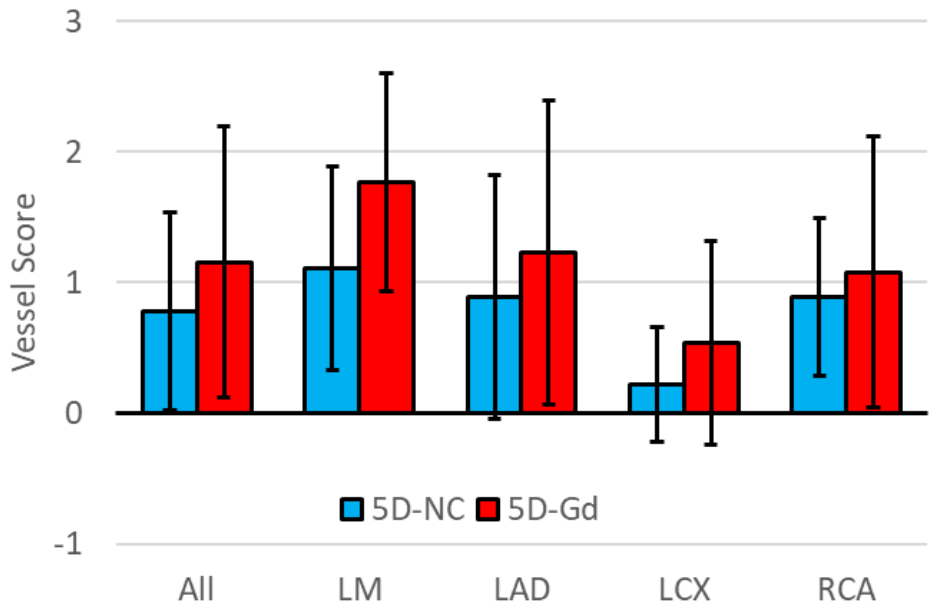

Figure 32: Vessel quality scores for patients imaged with the gadolinium-enhanced, spoiled-GRE acquisition (5D-Gd) (n = 52, N = 13) and patients imaged with the non-contrast–enhanced, bSSFP acquisition (5D-NC) (n = 9, N = 36). No significant differences were observed through unpaired *t*-test comparison of the vessel quality either invidually or combined ($\alpha = 0.05$). Significant differences were seen, however, for all groups when compared against the $\mu_0 = 4$ ($\alpha = 0.05$).

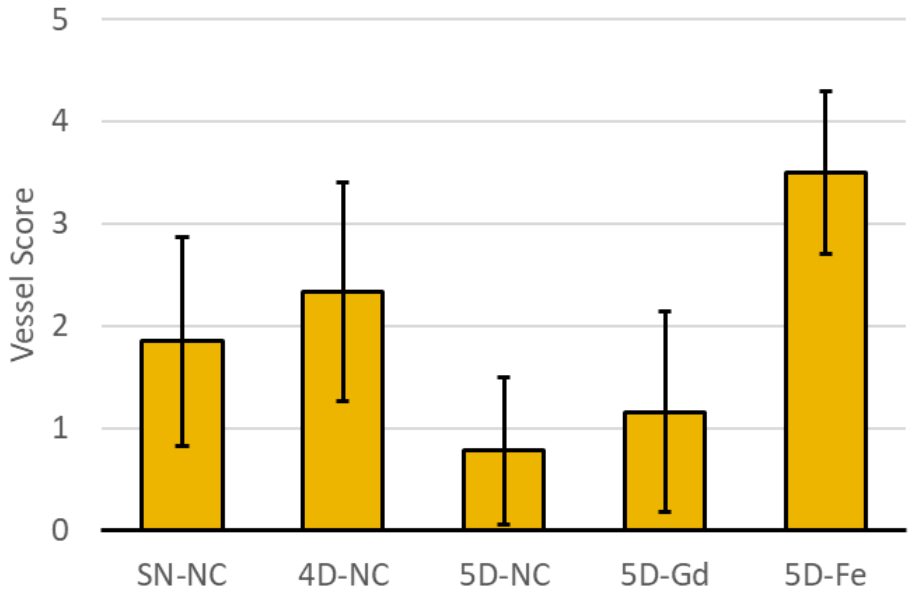

Figure 33: Comparison of vessel scores for all self-navigated methods tested including non-contrast, bSSFP self-navigation MRA (SN-NC), non-contrast, bSSFP 4D-GRASP MRA (4D-NC), non-contrast, bSSFP 5D-GRASP MRA (5D-NC), gadolinium-enhanced, spoiled-GRE 5D-GRASP MRA (5D-Gd), and ferumoxytol-enhanced, spoiled-GRE 5D-GRASP MRA (5D-Fe).

8.3.3 Ejection Fraction

The EF values computed with reformatted 5D-GRASP MRA images acquired with an SSFP acquisition were seen to correlate very strongly with the corresponding values

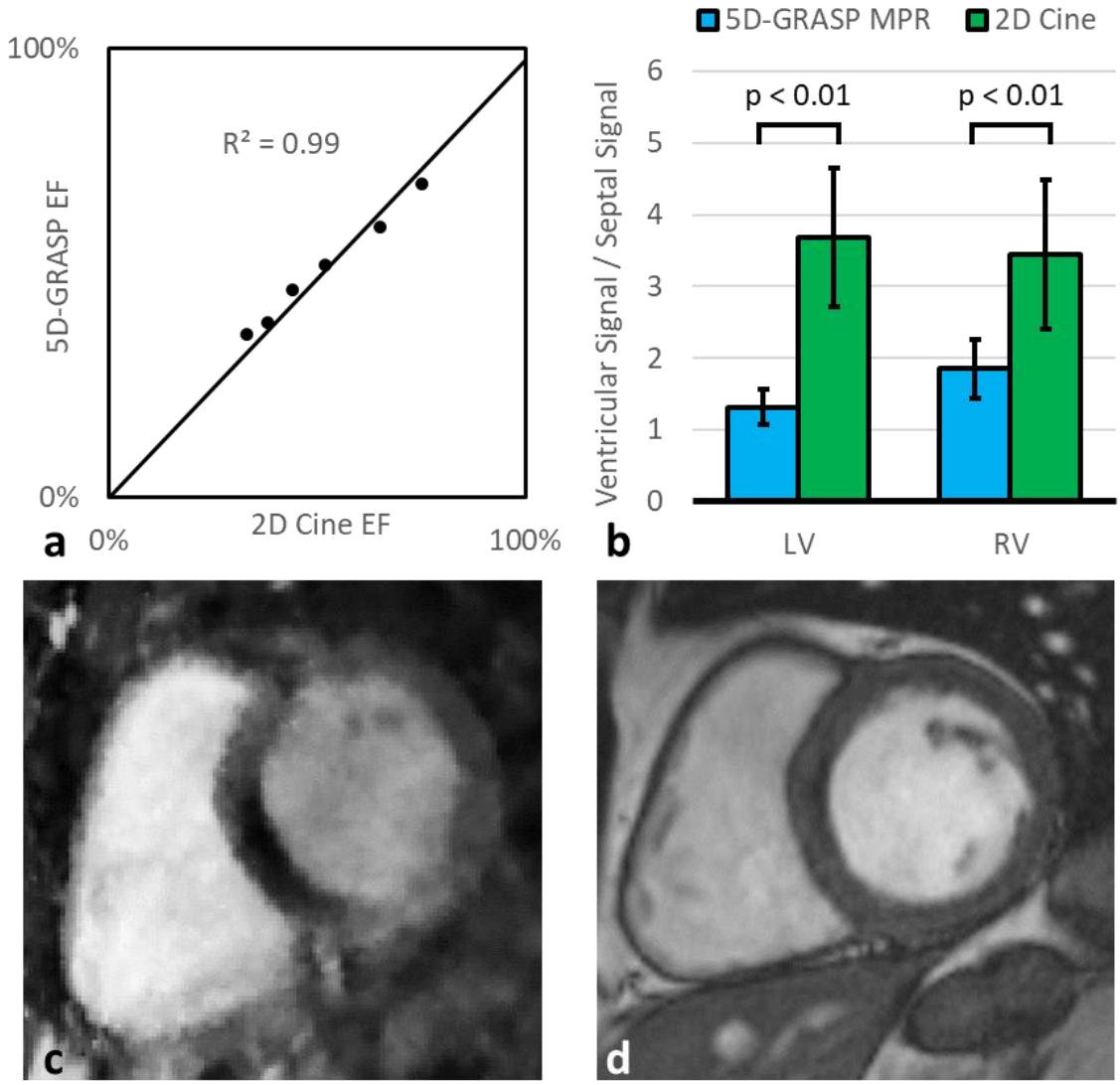

Figure 34: Comparison of EF calculated through MPR of 5D-GRASP coronary MRA and EF calculated through 2D cines (n = 6). (a) The EF values computed with both techniques were plotted against each other with correlation evaluated through Pearson's *r*. (b) Ventricular blood pool signal relative to myocardial septum in 2D cines and reformatted 5D images were seen to be significantly different for both the right and left ventricles. (c) Example of reformatted 5D image in ventricular short-axis view. (d) Example of ventricular short-axis 2D cine acquired during routine clinical scan.

found using the 2D cines acquired as part of the routine clinical scan (Figure 34a). Image quality was observed to be generally worse in the 5D MPR images (Figure 34c-d), however. Edges between the ventricular blood pools and the myocardium were seen to be softer in the 5D images, and the ventricular blood signal relative to the septal signal was lower in the 5D images as well (Figure 34b). This analysis was only done for six of the nine image sets in the bSSFP cohort as the other three image sets were of too poor quality for the endomyocardial wall to be identified.

8.3.4 Limited Dimension Reconstruction

Reconstruction time was substantially lower with fewer cardiac phases. For the first data set, reconstruction of the full five-dimensional image using all 10 bins required

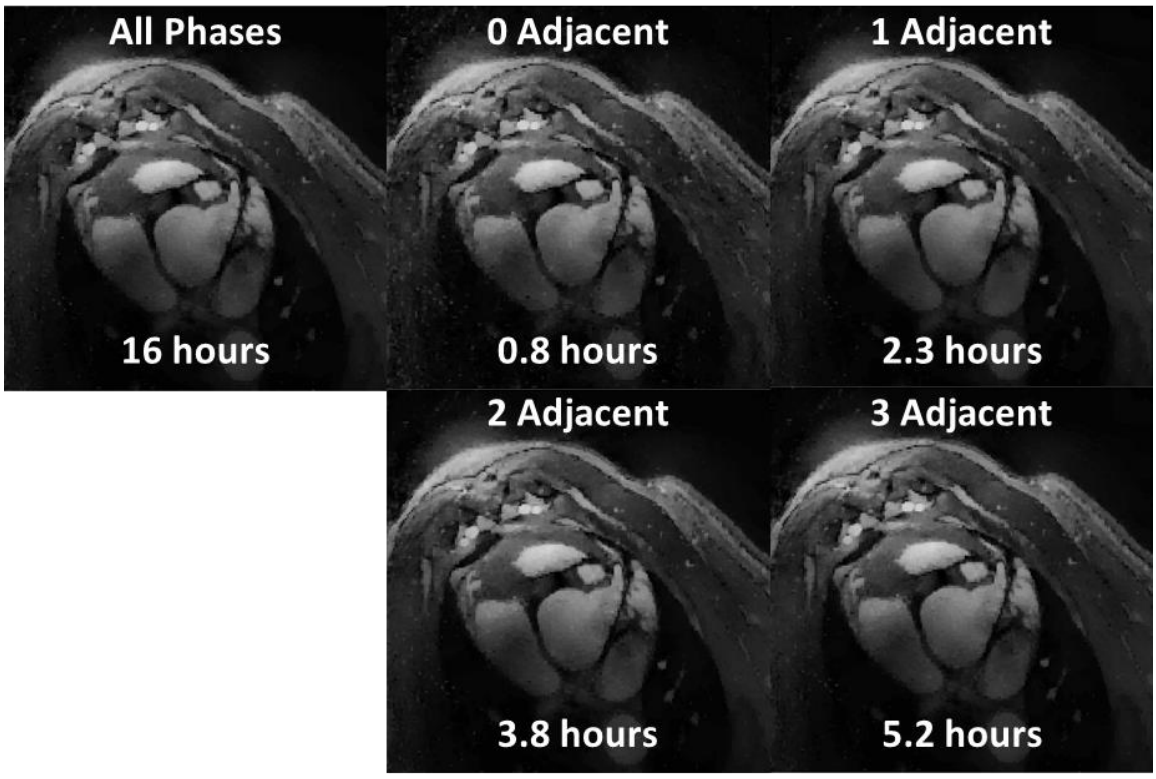

Figure 35: Visual comparison of images reconstructed with variable numbers of cardiac phases.

approximately 16 hours of reconstruction time. Conversely, using 0, 1, 2, or 3 adjacent cardiac phases for the limited reconstruction, only 0.8, 2.3, 3.8, and 5.2 hours were needed, respectively (Figure 35). For the second data set, 40.5 hours were needed to reconstruct all 24 phases, but the same times were needed in the limited reconstructions for this data set as in the first.

Visual inspection of the images reconstructed using fewer frames showed overall agreement with full reconstruction (Figure 35), though some minor differences could be seen particularly in the case where only the diastatic phase was used. The differences were not qualitatively determined to affect the potential diagnostic performance of the images. Quantitative comparison of the limited reconstructions against the full reconstruction reinforced these observations for both subjects tested (Figure 36). Generally strong correlation and structural similarity were seen for all cases with comparison with the

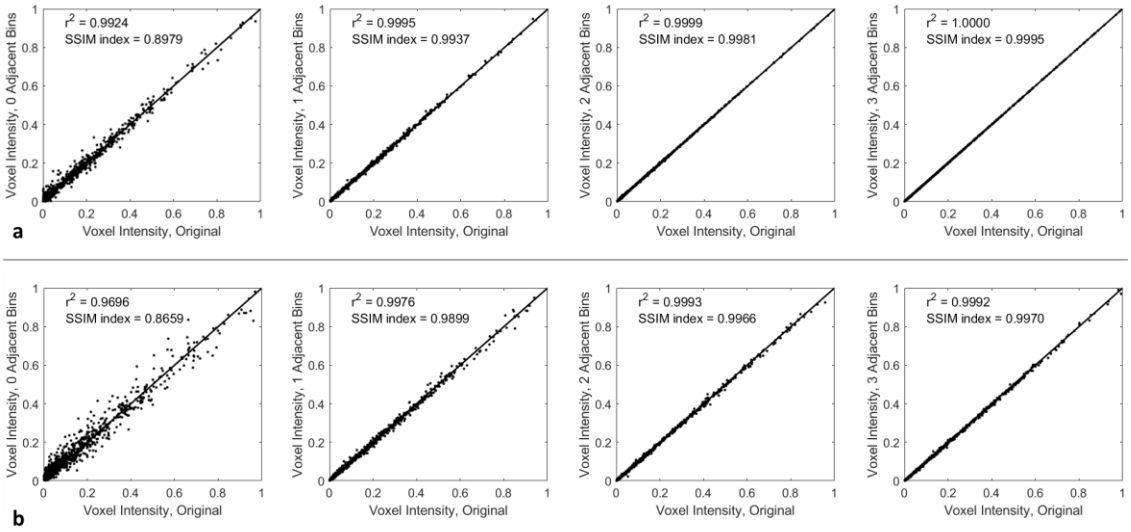

Figure 36: Similarity analysis of limited dimension reconstructions. Image sets reconstructed with limited cardiac dimension were compared against images reconstructed with all cardiac phases. For each volume, 1000 random voxels were selected and the intensity was plotted against the intensity of the corresponding voxel in the control volume, and Pearson's correlation coefficient was calculated. Additionally, the SSIM index was computed. Analysis was performed for two separate subjects (a) and (b).

original; however, this was particularly true for the cases in which one or more adjacent bins were used—i.e., the ones which actually utilized a five-dimensional reconstruction rather than simply a four-dimensional reconstruction with retrospective cardiac gating. Correlation and similarity were seen to increase with more adjacent phases, though both quantitative measures showed quick convergence towards 1.0.

8.4 Discussion

Of the three acquisitions tested, it was observed that the ferumoxytol-enhanced, spoiled-GRE sequence performed substantially better at characterizing the coronary three-dimensional geometry than either the non-contrast, bSSFP acquisition or the gadolinium-enhanced, spoiled-GRE acquisition. No significant difference was observed between the latter two groups in terms of imaging quality. The ability to correctly calculate the EF compared to clinical standard protocol did lend confidence in the bSSFP acquisition as far as its ability to correctly resolve the cardiac phases. However, in general, neither of the two acquisitions tested on human patients were determined to be of sufficient quality for three-dimensional segmentation of the coronary epicardial vasculature.

Though the theoretical disadvantages of the continuous bSSFP approach were discussed previously, this result is still somewhat unexpected. Without the T_2-prep pulse to amplify the myocardium-blood contrast, we would anticipate the image quality to be worse; without the saturation band on the anterior chest wall, we have fold-over artifacts manifesting as radial streaks which degrade the image. However, previously reported studies have shown relatively positive outcomes of this approach in comparison with 4D-GRASP MRA [26, 27]. Though the gadolinium-enhanced GRE approach has not previously been reported, the non-contrast bSSFP acquisition described here is very similar

to the methodology used by Feng et al. which yielded comparable quality to 4D-GRASP [26]. It is possible that this discrepancy is due to the populations investigated, as Di Sopra et al. only tested this acquisition on healthy volunteers. Patients with CHD may have anomalous cardiac rhythms which are not handled well by PCA. The exact causes of this disparity cannot be determined at this time and thus require further investigation. However, the results reported previously by Feng et al. only revealed an equal level of quality between 5D-GRASP MRA and 4D-GRASP MRA. According to the conclusions of Chapter 7, this level of quality still would not be sufficient for full three-dimensional characterization, so it is not suspected that resolving this discrepancy alone would be enough.

For the gadolinium-enhanced acquisition, the gadoteridol was administered as a bolus injection prior to the start of the scan, which resulted in the contrast between the blood pool and myocardium to lessen progressively as the contrast agent left the intravascular space. A potential correction for this would be a slow infusion of the gadolinium over the duration of the scan, to help maintain a constant level within the blood stream. Doing this was not possible in this study due to clinical limitations but may be an option in the future.

With both the bSSFP and gadolinium-enhanced GRE acquisitions, the manner in which the images appeared unsuitable was very similar for both. Using relatively low values for the regularization parameters (~0.01) produced images which were exceptionally noisy. To compensate for this noise, the values ultimately used were quite high so that information could be more easily shared across the cardiac and respiratory dimensions. Though this improved the noisiness of the images, it resulted in signal

averaging which removed finer details such as myocardial wall sharpness and vessel sharpness. To improve this, more initial information is needed to offload the reliance on the k-t SENSE algorithm; i.e., more samples are needed in each data set. Doing so in this clinical application was not possible, as only an eight minute window was allotted for the GRASP acquisition.

The image quality seen in the ferumoxytol-enhanced acquisition was substantially better than the other two 5D-GRASP MRA techniques and was also higher than what was seen previously in self-navigation MRA or 4D-GRASP MRA. The majority of the epicardial vessels imaged were fully three-dimensionally characterized. Further modifications of the protocol, however, could improve this success rate. The heart-rates seen in the pigs was much higher than what is typically observed in humans—around 100 to 140 bpm. Because of this, the number of cardiac phases that could be resolved was limited, meaning that more cardiac motion was captured within each phase. It is possible that imaging human patients with heart-rates closer to 40 to 70 bpm may automatically effect improvement due to the increased cardiac cycle resolution. Further improvement may come, again, from increasing the number of raw data points acquired, decreasing the number of segments acquired in each interleaf, and increasing the number of radial readouts per segment. Such changes would give an increased temporal and spatial resolution and reduce reliance on compressed sensing reconstruction to recover information from undersampled data. These changes would, of course, result in a longer scan time, however the spoiled-GRE acquisition employed with the ferumoxytol-enhanced acquisition was only 6 minutes and 29 seconds, so an increase in time should be allowable.

The computational cost of the reconstructions was high. Some reconstructions would perform in as few as 12 hours, but for many the time needed would exceed 24 or even 30 hours. One reconstruction required over 40 hours to complete. The time and computational hardware needed for these calculations will certainly be a hurdle for full clinical implementation of these protocols. Whole-heart MRA is very frequently used in patients with CHD to aid in positioning and planning other sequences.

The limited dimension reconstruction approach did show promising results. It was observed that reconstructing only the cardiac phase of interest with a limited number of adjacent phases—as few as three total phases—could produce images which were structurally identical to those acquired using the full data set. Due to the limited number of cardiac phases, reconstruction performed significantly faster, and could be completed in fewer than three hours. No differences were seen for the reconstruction times for the two subjects tested, which could suggest that the computational cost is constant for a set number of total bins. In practice, this timing should vary with acquisitions depending on regularization parameters and inherent continuity or discontinuity between physiologic states, however it does appear to be very largely dependent on the total dimensionality. It was not investigated here, but an obvious next step would be to investigate the same approach with a limited number of respiratory bins. Every reconstruction performed in this study used four reconstruction states, though it was generally observed that the best motion-compensation usually occurred at end-expiration. By using only this respiratory state and the one immediately adjacent, the total number of bins would be halved and could likely result in a significant reduction in reconstruction time as well.

The early success seen with this limited reconstruction approach shows promise for several applications of cardiac-resolved MRA. For coronary three-dimensional segmentation, only one motion state is needed and is almost always present at diastasis during end-expiration. In a subject with 10 cardiac and 4 respiratory states, 40 total bins are acquired from the data. However, by reconstructing only the bin at diastasis and end-inspiration and its immediate neighbors, the total number of bins can be reduced from 40 to 6. Similarly, for the use case of calculating the EF in the patient, only the volumes located at end-diastole and end-systole are needed. With only immediately adjacent physiologic states, this requires only 12 total bins.

It is important to note, however, that any dissimilarity observed between the limited dimension reconstructions and the full reconstructions does not necessarily imply that these shallow reconstructions are less accurate. The k-t SENSE algorithm utilizes a total variation–based compressed sensing reconstruction, which attempts to enforce continuity within dimensions. Ideally, this is used because all physiologic motions are continuous motions, however XD-GRASP is an inherently discrete approach to handling these motions. If a large amount of motion occurs between two adjacent physiologic bins, attempting to enforce continuity between them can result in images which are not necessarily representative of reality. It is, therefore, possible that the images reconstructed without any adjacent cardiac phases could be more accurate than those reconstructed using all cardiac phases. All that can be concluded here is the amount of similarity between these reconstructions, and further investigation of this would be useful in the future.

Though the ferumoxytol-enhanced group showed success, there is still limitations for its clinical implementation. In 2015, the U.S. Food and Drug Administration (**FDA**)

issued a boxed warning for ferumoxytol following a series of adverse events in patients after its use [63]. Bolus injection of ferumoxytol was identified as a risk factor for these events, and therefore the FDA currently advises that it be administered as an infusion over 15 minutes, which can add to the clinical overhead associated with the scan. However, because of its longevity in the patient, it is entirely possible to inject the agent into the patient well before they are actually on the scanner table. The potential for adverse events is still a cause for concern in its clinical use, and currently it is not FDA-approved for use in MRI except as an off-label drug. A recent multicenter study of off-label diagnostic use of ferumoxytol in MRI, however, concluded that diagnostic ferumoxytol use is well-tolerated and not associated with any serious adverse events [64]. Lastly, the cost of ferumoxytol is significantly higher than gadolinium-based contrast agents, which may also be a hurdle to its clinical implementation.

Another limitation to the techniques presented here is a lack of direct comparison of the anatomy measured here and a ground-truth measurement. For full validation of this approach, we would need to image the same subjects with CT or some invasive modality to determine if the MRI-derived anatomy is accurate. A phantom model could also be used to provide a known ground-truth for comparison, though such a model would necessarily be very complex. Such comparisons were determined to beyond the scope of the current study but would be necessary in the future.

8.5 Conclusion

The ability to retrospectively-gate cardiac temporal windows through 5D-GRASP MRA offers a substantial improvement for coronary MRA. Doing so, however, requires a continuous data acquisition, which imposes several requirements on the sequence. Under

these limitations, most magnetization preparatory pulses cannot be employed as this will preclude an adequate temporal resolution. It was observed that neither a non-contrast, bSSFP acquisition nor a gadolinium-enhanced, spoiled-GRE acquisition with continuous data sampling would be able to provide sufficient image quality for full coronary characterization in two cohorts of patients with CHD. A ferumoxytol-enhanced, spoiled-GRE acquisition, however, showed preliminary success in a cohort of pigs. The time required to reconstruct these five-dimensional images was seen to be very high, though it could be reduced through use of a limited number of cardiac phases. If the clinical hurdles for ferumoxytol can be overcome, it offers promise for significantly improved coronary MRA.

CHAPTER 9. CONCLUSIONS AND FUTURE WORK

9.1 Summary

The determination of which patients with CAD will benefit from intervention is critically important for providing proper treatment, but the gold standard for this determination—FFR—is underutilized due to its invasive nature. MRI is particularly well-suited for defining the boundary conditions needed for calculation of vFFR through CFD as it can measure both anatomy and flow velocity, directly. This thesis sought to further the development of MRI toward this overall objective. To do this, two aims were investigated:

1) Determine if PCMR can provide the inlet flow boundary conditions necessary for calculation of vFFR.
2) Determine if self-gated MRI can provide image quality sufficient for coronary geometry characterization.

In Aim 1, it was determined that *patient-specific* time-averaged hyperemic flow is needed to define the inlet flow boundary condition to calculate vFFR. This has two important implications. The first is that only the time-averaged flow is necessary, meaning that the patient-specific time-averaged basal flow rate can be measured through PCMR and then scaled by CFR to adequately define the boundary condition. The second implication is that patient-specific CFR is necessary for an accurate vFFR calculation. Because CT is incapable of measuring patient-specific CFR, this imposes limitations on the potential of CT-derived vFFR. Once it was determined what flow information was necessary, PCMR was tested for its ability to quantify time-averaged coronary arterial flow rate. It was shown

that coronary arterial flow measurements obtained through PCMR both exhibit repeatability and are consistent with coronary sinus flow measurements, which have been previously validated. In Aim 2, different implementations of self-gated MRI were investigated for their potential in coronary MRA. It was seen that self-navigation MRI could not provide sufficient quality, and this was suspected to be due to how it handles motion-compensation. These suspicions were confirmed through paired comparison with 4D-GRASP MRA, which showed significant improvement in image quality. 4D-GRASP MRA was still determined to not provide sufficient quality for calculation of vFFR due to its use of prospective cardiac-gating, and therefore 5D-GRASP MRA was investigated for its ability to retrospectively gate for both cardiac and respiratory motion. Three different implementations of 5D-GRASP MRA were considered, including a non-contrast bSSFP acquisition, a gadolinium-enhanced spoiled-GRE acquisition, and a ferumoxytol-enhanced spoiled-GRE acquisition. By far the best image quality of all self-gated MRI implementations tested was observed in the ferumoxytol-enhanced spoiled-GRE continuous acquisition with 5D-GRASP reconstruction, with full three-dimensional geometric characterization visible for most of the coronary vessels tested.

The results of these studies helped advance coronary MRA, both in quantifying flow and geometry. The potential for utilizing these techniques for calculating vFFR is clinically significant as it provides a non-invasive alternative with a fully patient-specific computational model. This can help increase the use of FFR in evaluating patients with CAD, thereby positively impacting patient care.

9.2 Future Work

Though the coronary arterial flow measurements obtained through PCMR were seen to be internally consistent, some limitations to these measurements were discovered. The flow rate measured through PCMR is the summation of the blood flow moving through the vessel and the motion of the vessel itself over the course of the cardiac cycle. For time-averaged flow rate, this vessel motion is not expected to significantly contribute to the net flow rate, so long as the ROI is maintained at a constant area. This can complicate flow rate measurements if adjacent tissues overlap with the ROI and its dimensions cannot be adjusted. Furthermore, this restricts PCMR from being used to quantify time-dependent coronary flow waveforms for use in simulations where time-dependent behavior is needed—such as in calculating wall shear stress or oscillatory shear index. Future work toward developing a more robust method for separating the flow velocity and vessel velocity would be useful both for simplifying the flow quantification process for vFFR and expanding the applications of PCMR elsewhere.

The ferumoxytol-enhanced 5D-GRASP technique was observed to provide the best image quality of all the techniques tested, but further development into this is necessary. The sample size tested was very limited due to the current safety concerns of off-label diagnostic use of ferumoxytol in humans, but further tests into its safety could reduce these restrictions and allow for more thorough testing. This technique was also observed to be limited by the spatial and temporal resolutions, though both of these limitations are hard-coded into the acquisition software and could not be changed. Further adjustment of these parameters and approval of the updated sequence would allow for testing of a more optimal acquisition technique which should likely show further improvement of the images.

Lastly, the combination of flow and anatomic measurements through MRI to develop a full non-invasive MRI-derived vFFR pipeline needs to be designed and tested against the invasive gold standard FFR to fully validate this methodology. This could be done through a complex phantom model designed to simulate the physiologic processes involved, an animal model, a patient model, or some combination thereof.

REFERENCES

1. Mozaffarian, D., et al., *Heart disease and stroke statistics--2015 update: a report from the American Heart Association.* Circulation, 2015. **131**(4): p. e29-322.

2. Harold, J.G., et al., *ACCF/AHA/SCAI 2013 update of the clinical competence statement on coronary artery interventional procedures: a report of the American College of Cardiology Foundation/American Heart Association/American College of Physicians Task Force on Clinical Competence and Training (Writing Committee to Revise the 2007 Clinical Competence Statement on Cardiac Interventional Procedures).* J Am Coll Cardiol, 2013. **62**(4): p. 357-96.

3. Chen, T.-C., C.D. Fryar, and X. Li, *Prevalence of uncontrolled risk factors for cardiovascular disease; United States, 1999-2010.* 2012.

4. Gould, K.L., K. Lipscomb, and G.W. Hamilton, *Physiologic basis for assessing critical coronary stenosis. Instantaneous flow response and regional distribution during coronary hyperemia as measures of coronary flow reserve.* Am J Cardiol, 1974. **33**(1): p. 87-94.

5. Shaw, L.J., et al., *Optimal medical therapy with or without percutaneous coronary intervention to reduce ischemic burden: results from the Clinical Outcomes Utilizing Revascularization and Aggressive Drug Evaluation (COURAGE) trial nuclear substudy.* Circulation, 2008. **117**(10): p. 1283-91.

6. Pijls, N.H., et al., *Fractional flow reserve a useful index to evaluate the influence of an epicardial coronary stenosis on myocardial blood flow.* Circulation, 1995. **92**(11): p. 3183-3193.

7. Pijls, N.H., et al., *Percutaneous coronary intervention of functionally nonsignificant stenosis: 5-year follow-up of the DEFER Study.* J Am Coll Cardiol, 2007. **49**(21): p. 2105-11.

8. Tonino, P.A., et al., *Fractional flow reserve versus angiography for guiding percutaneous coronary intervention.* New England Journal of Medicine, 2009. **360**(3): p. 213-224.

9. De Bruyne, B., et al., *Fractional flow reserve-guided PCI versus medical therapy in stable coronary disease.* N Engl J Med, 2012. **367**(11): p. 991-1001.

10. Dattilo, P.B., et al., *Contemporary patterns of fractional flow reserve and intravascular ultrasound use among patients undergoing percutaneous coronary intervention in the United States: Insights from the National Cardiovascular Data Registry.* J Am Coll Cardiol, 2012. **60**(22): p. 2337-9.

11. Taylor, C.A., T.A. Fonte, and J.K. Min, *Computational fluid dynamics applied to cardiac computed tomography for noninvasive quantification of fractional flow reserve: scientific basis.* J Am Coll Cardiol, 2013. **61**(22): p. 2233-41.

12. Choy, J.S. and G.S. Kassab, *Scaling of myocardial mass to flow and morphometry of coronary arteries.* J Appl Physiol (1985), 2008. **104**(5): p. 1281-6.

13. Murray, C.D., *The Physiological Principle of Minimum Work: I. The vascular System and the Cost of Blood Volume.* Proc. of the NAS of USA, 1926. **12**(3): p. 207-214.

14. Koo, B.K., et al., *Diagnosis of ischemia-causing coronary stenoses by noninvasive fractional flow reserve computed from coronary computed tomographic angiograms. Results from the prospective multicenter DISCOVER-FLOW (Diagnosis of Ischemia-Causing Stenoses Obtained Via Noninvasive Fractional Flow Reserve) study.* J Am Coll Cardiol, 2011. **58**(19): p. 1989-97.

15. Wilson, R.F., et al., *Effects of adenosine on human coronary arterial circulation.* Circulation, 1990. **82**: p. 1595-1606.

16. Ahn, S.G., et al., *Discordance Between Fractional Flow Reserve and Coronary Flow Reserve: Insights From Intracoronary Imaging and Physiological Assessment.* JACC Cardiovasc Interv, 2017. **10**(10): p. 999-1007.

17. Bryant, D., et al., *Measurement of flow with NMR imaging using a gradient pulse and phase difference technique.* J Comput Assist Tomogr, 1984. **8**(4): p. 588-593.

18. Firmin, D., et al., *In vivo validation of MR velocity imaging.* J Comput Assist Tomogr, 1987. **11**(5): p. 751-756.

19. Stehning, C., et al., *Free-breathing whole-heart coronary MRA with 3D radial SSFP and self-navigated image reconstruction.* Magn Reson Med, 2005. **54**(2): p. 476-80.

20. Piccini, D., et al., *Spiral phyllotaxis: the natural way to construct a 3D radial trajectory in MRI.* Magn Reson Med, 2011. **66**(4): p. 1049-56.

21. Piccini, D., et al., *Respiratory self-navigation for whole-heart bright-blood coronary MRI: methods for robust isolation and automatic segmentation of the blood pool.* Magn Reson Med, 2012. **68**(2): p. 571-9.

22. Piccini, D., et al., *Respiratory self-navigated postcontrast whole-heart coronary MR angiography: initial experience in patients.* Radiology, 2014. **270**(2): p. 378-86.

23. Coppo, S., et al., *Free-running 4D whole-heart self-navigated golden angle MRI: Initial results.* Magn Reson Med, 2015. **74**(5): p. 1306-16.

24. Piccini, D., et al., *Four-dimensional respiratory motion-resolved whole heart coronary MR angiography.* Magn Reson Med, 2016.

25. Feng, L., et al., *XD-GRASP: Golden-angle radial MRI with reconstruction of extra motion-state dimensions using compressed sensing.* Magn Reson Med, 2016. **75**(2): p. 775-88.

26. Feng, L., et al., *5D whole-heart sparse MRI.* Magn Reson Med, 2018. **79**(2): p. 826-838.

27. Di Sopra, L., et al., *An automated approach to fully self-gated free-running cardiac and respiratory motion-resolved 5D whole-heart MRI.* Magn Reson Med, 2019. **82**(6): p. 2118-2132.

28. Hair, J.B., L.H. Timmins, and J. Oshinski. *Magnetic Resonance Imaging - Derived Coronary Fractional Flow Reserve: Preliminary Results*. in *Society for Magnetic Resonance Angiography*. 2016. Chicago, IL.

29. Rosamond, W., et al., *Heart disease and stroke statistics--2007 update: a report from the American Heart Association Statistics Committee and Stroke Statistics Subcommittee.* Circulation, 2007. **115**(5): p. e69-171.

30. Cook, C.M., et al., *Diagnostic Accuracy of Computed Tomography-Derived Fractional Flow Reserve : A Systematic Review.* JAMA Cardiol, 2017. **2**(7): p. 803-810.

31. Hartlage, G.R., et al., *Prediction of response to cardiac resynchronization therapy using left ventricular pacing lead position and cardiovascular magnetic resonance derived wall motion patterns: a prospective cohort study*. J Cardiovasc Magn Reson, 2015. **17**: p. 57.

32. Yang, Q., et al., *Contrast-enhanced whole-heart coronary magnetic resonance angiography at 3.0-T: a comparative study with X-ray angiography in a single center*. J Am Coll Cardiol, 2009. **54**(1): p. 69-76.

33. Sethian, J.A., *A fast marching level set method for monotonically advancing fronts.* Proceedings of the National Academy of Sciences, 1996. **93**(4): p. 1591-1595.

34. Sethian, J.A., *Level set methods and fast marching methods: evolving interfaces in computational geometry, fluid mechanics, computer vision, and materials science*. Vol. 3. 1999: Cambridge university press.

35. Antiga, L., B. Ene-Iordache, and A. Remuzzi, *Computational geometry for patient-specific reconstruction and meshing of blood vessels from MR and CT angiography.* IEEE transactions on medical imaging, 2003. **22**(5): p. 674-684.

36. Samady, H., et al., *Coronary artery wall shear stress is associated with progression and transformation of atherosclerotic plaque and arterial remodeling in patients with coronary artery disease.* Circulation, 2011. **124**(7): p. 779-88.

37. Hung, O.Y., et al., *Comprehensive Assessment of Coronary Plaque Progression With Advanced Intravascular Imaging, Physiological Measures, and Wall Shear Stress: A Pilot Double-Blinded Randomized Controlled Clinical Trial of Nebivolol Versus Atenolol in Nonobstructive Coronary Artery Disease.* J Am Heart Assoc, 2016. **5**(1).

38. Bland, J.M. and D.G. Altman, *Statistical Methods for Assessing Agreement Between Two Methods of Clinical Measurement.* The Lancet, 1986. **327**(8476): p. 307-310.

39. Lin, L.I.K., *A Concordance Correlation Coefficient to Evaluate Reproducibility*. Biometrics, 1989. **45**(1): p. 255-268.

40. Davies, J., et al. *Evidence of a dominant backward-propagating*. 2006. BMJ PUBLISHING GROUP.

41. Morris, P.D., et al., *Fast Virtual Fractional Flow Reserve Based Upon Steady-State Computational Fluid Dynamics Analysis: Results From the VIRTU-Fast Study.* JACC Basic Transl Sci, 2017. **2**(4): p. 434-446.

42. Nakazato, R., et al., *CFR and FFR assessment with PET and CTA: strengths and limitations.* Curr Cardiol Rep, 2014. **16**(5): p. 484.

43. Levitt, M.H., *Spin dynamics: basics of nuclear magnetic resonance*. 2001: John Wiley & Sons.

44. Moran, P.R., R. Moran, and N. Karstaedt, *Verification and evaluation of internal flow and motion. True magnetic resonance imaging by the phase gradient modulation method.* Radiology, 1985. **154**(2): p. 433-441.

45. Stankovic, Z., et al., *4D flow imaging with MRI.* Cardiovasc Diagn Ther, 2014. **4**(2): p. 173-92.

46. Nayler, G., D. Firmin, and D. Longmore, *Blood flow imaging by cine magnetic resonance.* J Comput Assist Tomogr, 1986. **10**(5): p. 715-722.

47. Sakuma, H., et al., *MR measurement of coronary blood flow.* Journal of Magnetic Resonance Imaging: An Official Journal of the International Society for Magnetic Resonance in Medicine, 1999. **10**(5): p. 728-733.

48. Kawada, N., et al., *Hypertrophic cardiomyopathy: MR measurement of coronary blood flow and vasodilator flow reserve in patients and healthy subjects.* Radiology, 1999. **211**(1): p. 129-135.

49. Hundley, W.G., et al., *Assessment of coronary arterial restenosis with phase-contrast magnetic resonance imaging measurements of coronary flow reserve.* Circulation, 2000. **101**(20): p. 2375-2381.

50. Lam, A., et al., *Performance of 3D, navigator echo-gated, contrast-enhanced, magnetic resonance coronary vein imaging in patients undergoing CRT.* Journal of Interventional Cardiac Electrophysiology, 2014. **41**(2): p. 155-160.

51. Heiberg, E., et al., *Design and validation of Segment-freely available software for cardiovascular image analysis.* BMC medical imaging, 2010. **10**(1): p. 1.

52. Johnson, K., P. Sharma, and J. Oshinski, *Coronary artery flow measurement using navigator echo gated phase contrast magnetic resonance velocity mapping at 3.0 T.* J Biomech, 2008. **41**(3): p. 595-602.

53. Ganz, W., et al., *Measurement of coronary sinus blood flow by continuous thermodilution in man.* Circulation, 1971. **44**(2): p. 181-195.

54. Piccini, D., *Respiratory Self-Navigation for Free Breathing Whole-Heart Coronary MR Imaging with High Isotropic Spatial Resolution in Patients.* 2013.

55. Agarwal, A., et al., *Age- and Lesion-Related Comorbidity Burden Among US Adults With Congenital Heart Disease: A Population-Based Study.* J Am Heart Assoc, 2019. **8**(20): p. e013450.

56. Chandarana, H., et al., *Respiratory Motion-Resolved Compressed Sensing Reconstruction of Free-Breathing Radial Acquisition for Dynamic Liver Magnetic Resonance Imaging.* Invest Radiol, 2015. **50**(11): p. 749-56.

57. Chandarana, H., et al., *Free-breathing contrast-enhanced multiphase MRI of the liver using a combination of compressed sensing, parallel imaging, and golden-angle radial sampling.* Investigative radiology, 2013. **48**(1).

58. Feng, L., et al., *Golden-angle radial sparse parallel MRI: combination of compressed sensing, parallel imaging, and golden-angle radial sampling for fast and flexible dynamic volumetric MRI.* Magnetic resonance in medicine, 2014. **72**(3): p. 707-717.

59. Pang, J., et al., *ECG and navigator-free four-dimensional whole-heart coronary MRA for simultaneous visualization of cardiac anatomy and function.* Magn Reson Med, 2014. **72**(5): p. 1208-17.

60. Bieri, O. and K. Scheffler, *Fundamentals of balanced steady state free precession MRI.* J Magn Reson Imaging, 2013. **38**(1): p. 2-11.

61. Prince, M.R., et al., *A pilot investigation of new superparamagnetic iron oxide (ferumoxytol) as a contrast agent for cardiovascular MRI.* Journal of X-ray science and technology, 2003. **11**(4): p. 231-240.

62. Tweedle, M., et al., *Reaction of gadolinium chelates with endogenously available ions.* Magnetic resonance imaging, 1991. **9**(3): p. 409-415.

63. Administration., U.S.F.a.D. *FDA Drug Safety Communication: FDA strengthens warnings and changes prescribing instructions to decrease the risk of serious allergic reactions with anemia drug Feraheme (ferumoxytol)*. 2015 [cited 2020 March 7]; Available from: http://www.fda.gov/Drugs/DrugSafety/ucm440138.htm.

64. Nguyen, K.-L., et al., *Multicenter Safety and Practice for Off-Label Diagnostic Use of Ferumoxytol in MRI.* Radiology, 2019. **293**(3): p. 554-564.